UNIVERSITÀ DEGLI STUDI DI UDINE

Dipartimento di Ingegneria Elettrica, Gestionale e Meccanica

Corso di Dottorato in Ingegneria Industriale e dell'Informazione

Tesi di Dottorato

CYCLIC BLOCK FILTERED MULTITONE MODULATION: DESIGN AND PERFORMANCE ANALYSIS

Relatore:
Prof. ANDREA M. TONELLO

Dottorando:
MAURO GIROTTO

Marzo 2015

ANNO ACCADEMICO 2014-2015

Contents

List of Tables

List of Figures

List of Acronyms

ADSL Asymmetric Digital Subscriber Line

BB-PLC broadband PLC

CB-FMT Cylic Block Filtered Multitone Modulation

CCDF complementary cumulative distribution function

CENELEC European Committee for Electrotechnical Standardization

CM common mode

CP cyclic prefix

DWMT discrete wavelet multi-tone modulation

DFT Discrete Fourier Transform

EMC electromagnetic compatibility

FBM Filter Bank Modulation

FCC Federal Communications Commission

FD frequency domain

FFT Fast Fourier Transform

FMT Filtered Multitone

FSK frequency-shift keying

GFDM Generalized Frequency Division Multiplexing

HV high voltage

IBI inter-block interference

ICI inter-carrier interference

IDFT inverse DFT

IEC International Electrotechnical Commission

ISI inter-symbol interference

LTI linear time invariant

LTV linear time variant

LV low voltage

MCM multi-carrier modulation

MSE mean square error

MMSE minimum mean square error

MV medium voltage

NB-PLC narrowband PLC

O-LV outdoor low voltage

O-MV outdoor medium voltage

OFDM Orthogonal Frequency Division Multiplexing

PAPR Peak-to-Average Power Ratio

PLC Power Line Communication

PR perfect reconstruction

PS-OFDM pulse-shaped OFDM

PSD power spectral density

QAM quadrature amplitude modulation

RRC root raised cosine

SER symbol error rate

SNR signal-to-noise ratio

TCTL transverse conversion transfer loss

VDSL very-high-bit-rate digital subscriber line

WLAN wireless local area network

WMAN wireless metropolitan area network

WOFDM Windowed OFDM

ZF zero forcing

Abstract

Nowadays, high data rate communication demand is growing. Thus, several communication technologies, both wireless and wireline, have adopted Filter Bank Modulation (FBM) at the physical layer. In a general FBM scheme, the high data rate stream is converted into a series of several parallel low data rate streams. These streams are modulated with a series of carrier signals. In frequency domain, the available bandwidth is partitioned in disjointed sub-channels. If the sub-channel number is sufficiently high, the sub-channel frequency response is quasi-flat and the equalizer can be simplified. Furthermore, FBM schemes have low complexity digital implementation and bit loading could be used to minimize the transmission power.

In this thesis, a FBM transceiver is presented. The idea is to obtain good sub-channel frequency confinement as it is done by the family of exponentially modulated filter banks that is typically referred to as Filtered Multitone (FMT) modulation. However, differently from conventional FMT, the linear convolutions are replaced with circular convolutions. Since transmission occurs in blocks, the scheme is referred to as Cylic Block Filtered Multitone Modulation (CB-FMT). This thesis focuses on the principles, design, implementation and performances analysis of CB-FMT. In particular, it is shown that an efficient realization of both the transmitter and the receiver is possible in the frequency domain (FD), and it is based on the concatenation of an inner Discrete Fourier Transform (DFT) and a bank of outer DFTs. Such an implementation suggests a simple sub-channel FD equalizer. The overall required implementation complexity is lower than in FMT. Furthermore, the orthogonal filter bank design is simplified. The sub-channel frequency confinement in CB-FMT yields compact power spectrum and lower peak-to-average power ratio than in Orthogonal Frequency Division Multiplexing (OFDM).

Then, the orthogonal prototype pulse design problem is considered. The orthogonality conditions are derived in time domain and frequency domain. These conditions are translated in matrix form and pulse coefficients are parameterized with hyper-spherical coordinates, a non-linear combination of trigonometric functions. The mathematical analysis shows that exists an infinite number of solutions. Next, the orthogonality is discussed in presence of a transmission medium. In general, the channel could destroy the orthogonality. Finally, optimal orthogonal pulses are designed to maximize the in-band-to-out-band energy ratio and the achievable rate in time-variant channel scenario. These optimal pulses improve the performance of the baseline root-raised-cosine pulse.

Furthermore, the equalization task is discussed. Equalizers are necessary

to restore the orthogonality when an equivalent filter is inserted between the transmitter and the receiver. This filter could represent the transmission medium, a real interpolation filter or the hardware non-ideality. We discuss several equalizers, both for time-invariant and time-variant channels. A cyclic prefix (CP) can be added to the transmitted signal. We show that when the CP length is greater than the channel impulse response length, perfect reconstruction (PR) is possible. For time-invariant channels, a simple 1-tap equalizer is sufficient to restore the orthogonality. We show that in the time-variant scenario, the 1-tap equalizer is not sufficient to restore the orthogonality. Several equalizers are proposed for the time-variant case.

Finally, performances in real application scenarios are evaluated. We start from Power Line Communications. For in-home high data rate communications, broadband PLC (BB-PLC) is used. BB-PLC generally operates in the band 2-30 MHz. Transmission above 30 MHz is possible, but the electromagnetic compatibility (EMC) limits are more stringent than the limits in the band below 30 MHz. In the 2-30 MHz range there are several sub-bands dedicated to other communication systems, e.g. to amateur radio. A spectrum notching mask has to be fulfilled by the power spectral density (PSD) of the transmitted signal to grant coexistence. For command and control applications, narrowband PLC (NB-PLC) is used. NB-PLC operates in portions of the 3-500 kHz spectrum and it has to obey certain spectral masks for EMC and coexistence issues, similarly to BB-PLC. Although OFDM allows simple spectrum management by switching on-off the sub-channels, its poor sub-channel frequency selectivity translates into a poor spectrum usage. An agile use of the spectrum and higher spectral efficiency can be obtained with filter bank modulation. In particular, we investigate the use of CB-FMT modulation and compare it to pulse-shaped OFDM (PS-OFDM) deployed in the G3-PLC and IEEE P1901.2 standards for NB-PLC. For BB-PLC, we compare CB-FMT with the HomePlug standard. The comparison shows that higher spectral efficiency and improved spectrum management can be achieved with CB-FMT.

For the wireless scenario, the land mobile radio systems are considered. The transmitted signal propagates through a multipath channel. This propagation model is caused by several natural and man-made obstacles that introduce reflections, diffraction and scattering. Time-invariant and time-variant scenarios are considered. The FD equalization allows the exploitation of the transmission medium time and frequency diversity; thus, it potentially yields lower symbol error rate and higher achievable rate in time-variant frequency-selective fading.

Chapter 1

Introduction

This thesis deals with FBM. FBM systems, also referred to as multi-carrier modulation systems, have been successfully applied to a wide variety of digital communication applications over the past several years. The research of improved solutions is still large because the demand for broadband telecommunication services is growing, both over wireline and wireless channels.

Wide band channels are characterized by frequency selectivity which translates in time dispersive impulse responses that cause significant inter-symbol interference (ISI) in digital communication systems. FBM transceivers employ a transmission technique where a set of narrowband signals (low data rate sequences) are transmitted simultaneously over a broadband channel [1]. In particular, each low rate data sequence is transmitted through a sub-channel. If the sub-channels are sufficiently narrowband, they will experience an overall flat frequency response so that the medium frequency selectivity will not introduce significant ISI. Therefore, the channel equalization task can be simplified. More in general, FBM architectures aim to increase the system spectral efficiency, to enable the agile use of spectrum and the flexible adaptation of available resources.

Two baseline FBM solutions are OFDM [2] and FMT [3]. FMT consists of an exponentially modulated filter bank that privileges the sub-channel frequency confinement rather than the time confinement, as for example OFDM does. In FMT, with frequency confined pulses, the sub-channels are quasi-orthogonal to each other which prevents the system to suffer from ICI, while the ISI introduced by the frequency selective medium, can be mitigated with sub-channel equalization [3],[4] or with the use of outer OFDM modules, one per sub-channel, as described in the concatenated OFDM-FMT scheme in [5].

OFDM is the most famous and used FBM scheme. Indeed, this system has an efficient implementation that exploits the DFT. Furthermore,

a single tap zero forcing equalizer restores the orthogonality for transmissions over time-invariant frequency-selective channel. These two aspects have contributed to disseminate the OFDM scheme in various application scenarios. OFDM has been adopted in several important telecommunication standards. For wireless applications, OFDM is adopted for wireless local area network (WLAN) in IEEE 802.11 standards [6]. For the wireless metropolitan area network (WMAN), OFDM is employed in the WiMAX (IEEE 802.16) standard [7]. More recently, OFDM has been adopted for high data rate transmission in the fourth generation of mobile telecommunications technology. In the downlink of the new cellular standard LTE [8], OFDM is employed. Besides, OFDM is used for terrestrial broadcasting of digital audio (DAB) [9] and video (DVB) [10]. For wired applications, OFDM is adopted in Asymmetric Digital Subscriber Line (ADSL) to provide internet access [11]; OFDM is also used in Power Line Communication (PLC) in the HomePlug standard for broadband communications [12] and in the IEEE P1901 standard [13] for narrowband communications. OFDM is also used in the ITU.T NB and BB standards.

The research interest in OFDM and, in general, in FBM is still high because OFDM has several drawbacks. First, OFDM has poor frequency confinement characteristics. Thus, high out-of-band interference is present due to the high spectral sidelobes. To reduce this interference, PS-OFDM was introduced [14]. Out-of-band radiations are a serious problem in Cognitive Radio and its reduction is objective of study. Another drawback is the high Peak-to-Average Power Ratio (PAPR) that grows exponential with the number of sub-channels [15]. Furthermore, OFDM is sensitive to the time-variant channels, e.g. in the mobile communications.

For these reasons, several FBM schemes have been proposed in the literature. In addition to FMT and PS-OFDM, we can cite Windowed OFDM (WOFDM), discrete wavelet multi-tone modulation (DWMT) [16] and Offset-QAM [17].

In this thesis, a study on an alternative FBM scheme is presented. This scheme, known as CB-FMT, follows the idea behind FMT. The sub-channel filters are designed to have high frequency domain confinement. This allows to significantly reduce the out-of-sub-channel band energy. Thus, each sub-channel is independent from the others. Generally, in FMT, the frequency confinement increases the computational complexity. In CB-FMT the complexity is less than conventional FMT due to an efficient frequency domain implementation that exploits the Fast Fourier Transform (FFT) algorithm. In this work, the CB-FMT system is mathematically analyzed. Then, the orthogonal pulse prototype design is considered. Next, the equalization problem is

considered. Finally, the performances are evaluated over wireline (Power Line Communications) and wireless (mobile communications) channels.

In details, this thesis is organized as follows:

Chapter 2

In this chapter, we introduce the baseline idea behind the Filter Bank Modulations and the motivations that allow to improve the performances of the single-carrier systems. A general FBM architecture is reported and mathematically analyzed. This architecture is valid for both OFDM and FMT systems. To obtain one or the other system is sufficient to modify the parameters, i.e. the number of sub-channels, the interpolation factor and the prototype pulse impulse response. Then, we briefly recall the main concepts of OFDM and FMT and we report the mathematical representation of the transmitted and received signals.

Chapter 3

In this chapter, the CB-FMT filter bank modulation transceiver is presented. The idea is to obtain good sub-channel frequency confinement as it is done by the family of exponentially modulated filter banks that is typically referred to as FMT modulation. However, differently from conventional FMT, the linear convolutions are replaced with circular convolutions. Since transmission occurs in blocks, the scheme is referred to as Cyclic Block FMT.

This chapter focuses on the principles of CB-FMT, the design and the implementation. In particular it is shown that an efficient realization of both the transmitter and the receiver is possible in the FD and it is based on the concatenation of an inner DFT and a bank of outer DFTs. Such an implementation suggests a simple sub-channel FD equalizer. Then, the differences between CB-FMT and OFDM and between CB-FMT and FMT are shown to better understand the difference between these three FBM architectures. Next, the complexity is analyzed. The overall required implementation complexity is lower than in FMT.

The orthogonal filter bank design problem is introduced. This important topic is described in details in Chapter 4. In this chapter, we only show that the orthogonal filter bank design is simplified.

The PSD and PAPR of the transmitted signal are studied. The sub-channel frequency confinement in CB-FMT yields compact power spectrum and lower PAPR than in OFDM.

Several numerical results are provided is this chapter on:

- in-band-to-out-of-band energy ratio as a function of the system parameters, namely the prototype pulse length and sub-channel number;
- complexity comparison as a function of the prototype pulse length for FMT, CB-FMT and OFDM;
- PAPR comparison between the CB-FMT and the OFDM systems for different sub-channel numbers.

Chapter 4

In this chapter, we extensively discuss the prototype pulse design. The chapter is divided into two parts. The first part is essentially theoretical. Ideal conditions are assumed, i.e. the received signal is equal to the transmitted signal, without distortions. Under this assumption, the PR conditions are derived. If the PR conditions are satisfied, the information sequences at the receiver output are identical to the transmitted sequences. Then, the PR conditions are translated from time domain to frequency domain.

Next, the matched filter condition is added to obtain the orthogonality conditions. Orthogonal pulses are designed to maximize the signal-to-noise ratio (SNR) at the receiver output. These conditions are rewritten in a compact matrix form. To satisfy the orthogonality conditions, a non-linear system must be solved. This system can be partitioned in sub-systems to simplify the numerical solution. Finally, the prototype pulse is parametrized as a non-linear combination of trigonometric functions. This parametrization allows to simplify the numerical design.

In the second part, we consider the orthogonality problem under non-ideal conditions. An equivalent filter is added between the transmitter and the receiver. This filter can represent a real interpolation filter or a frequency selective channel. Orthogonality conditions are also analyzed in this case.

Finally, optimal orthogonal pulses are designed. The optimization is performed under an objective function maximization. Two metric functions are considered: the in-band-to-out-of-band energy ratio and the achievable rate over time-variant wireless channels.

As numerical results, in this chapter we design the optimal pulses for the two metrics for different parameters.

Chapter 5

This chapter is focused on the equalization task in CB-FMT. From the previous chapter, we demonstrate that, in general, orthogonality is lost when a non-ideal transmission medium is present between the transmitter and the receiver.

Orthogonality loss may introduce interference that lowers the performance. To avoid this, an equalizer is necessary.

First a matrix model of the channel is introduced. This allows to provide a compact representation of the transmission medium effects. The model is valid for both time-invariant and time-variant channels and it includes the CP effect. Then, we translate the model from time domain to frequency domain. The equalizers are designed in frequency domain under a long CP assumption, i.e. the cyclic prefix duration is greater than the channel impulse response.

Next, we show that a single-tap equalizer is sufficient to restore the orthogonality when the channel is time-invariant. For time-variant channels, we propose four equalizers: single-tap, band equalizer, block equalizer and optimal equalizer. These equalizers are sorted in terms of complexity. Only the optimal equalizer can restore the orthogonality in a time-variant scenario. The others equalizers are sub-optimal but can provide good performance with lower complexity.

Chapter 6

In this chapter, we perform a performance analysis of the CB-FMT scheme for two applications scenarios. Power Line Communications and the mobile wireless communications are considered.

For PLC, we summarize the main aspects. After a historical overview, we report the channel characteristic for indoor low-voltage, outdoor low-voltage and medium-voltage channels. Then, we introduce the noise models for the considered applications scenarios. In contrast to wireless, where the noise is white, in PLC the background noise is colored and has an exponential PSD profile. At the lower frequencies the noise is higher. Then, electromagnetic compatibility aspects are considered. Next, we describe the BB-PLC and the NB-PLC, and we show some numerical results in terms of achievable rate.

For wireless communication, we provide a historical overview and we report the relevant channel model for mobile communications. We provide some numerical results in terms of symbol error rate (SER) and achievable rate for time-invariant and time-variant channels.

Related Publications

The main results of this thesis have been the subject of the publications listed below.

Journal Papers

- M. Girotto and A. Tonello, "Design of Orthogonal Cyclic Block Filtered Multitone Modulation," to be submitted *to IEEE Transactions on Communications*.

- A. Tonello, A. Pittolo and M. Girotto, "Power Line Communications: Understanding the Channel for Physical Layer Evolution Based on Filter Bank Modulation," *IEICE Transactions on Communications*, vol. E97-B, no. 8, p. 1494–1503, 2014.

- A. Tonello and M. Girotto, "Cyclic Block Filtered Multitone Modulation," *EURASIP Journal on Advances in Signal Processing*, vol. 2014, no. 1, p. 109, 2014.

- A. Tonello, F. Versolatto and M. Girotto, "Multi-Technology (I-UWB and OFDM) Coexistent Communications on the Power Delivery Network," *IEEE Transactions on Power Delivery*, vol. 28, no. 4, p. 2039–2047, Oct. 2013.

Conference Papers

- M. Girotto and A. M. Tonello, "Improved Spectrum Agility in Narrow-Band PLC with Cyclic Block FMT Modulation," in *Globecom 2014 - Symposium on Selected Areas in Communications: Power Line Communications (GC14 SAC/PLC)*, Austin, USA, Dec. 2014.

- M. Girotto and A. M. Tonello, "Orthogonal Design of Cyclic Block Filtered Multitone Modulation," in *Proc. of European Wireless 2014*, Barcelona, Spain, May 14-16, 2014.

- A. M. Tonello and M. Girotto, "Cyclic Block FMT Modulation for Communications in Time-Variant Frequency Selective Fading Channels," in *Proc. of European Signal Processing Conference (EUSIPCO 2013)*, Marrakech, Morocco, September 2013.

- A. M. Tonello and M. Girotto, "Cyclic Block FMT Modulation for Broadband Power Line Communications," in *Proc. of IEEE ISPLC 2013*, Johannesburg, SA, March 24-27, 2013.

Chapter 2

Filter Bank Modulations

2.1 Introduction

In telecommunications, the term *modulation* refers to the process that converts the digital information, namely the bits of the information sequence, to electrical signals suitable to be transmitted on the transmission medium. In the ISO/OSI model, modulation is placed at the lowest layer, namely in the physical layer.

Early digital communications exploit single-carrier modulations. The information bits are gathered in symbols. Each symbol changes the electrical characteristic of a periodic signal. This signal is known as carrier and, usually, is a sinusoidal signal. For example, in an amplitude modulation, e.g. ASK, the symbols change the amplitude of the carrier. In a frequency modulation, e.g. frequency-shift keying (FSK), the symbols change the frequency of the sinusoidal signal. The electrical characteristics - amplitude, frequency and phase - can jointly change. For example, in quadrature amplitude modulation (QAM) the symbols change both the amplitude and the phase of the carrier.

Single-carrier modulations are suitable when the transmission medium exhibits flat frequency response, i.e. when the channel introduces a simple attenuation to the signal in the transmission bandwidth. In some scenarios, e.g. wireless communications and Power Line Communications, the channel is frequency selective. In time domain, this selectivity is translated into long channel impulse responses. The time dispersion introduces significant ISI that requires complex equalization techniques.

To simplify the equalization process, the multi-carrier modulation (MCM) has been introduced. The baseline idea is quite simple: transmit data by dividing the stream in a series of parallel streams. Each stream is associated

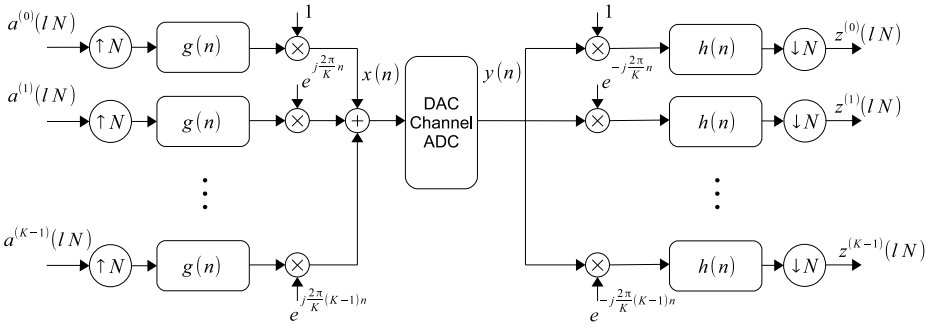

Figure 2.1: General Filter Bank Modulation scheme.

to a different carrier. This allows to divide the total signal bandwidth into a series of sub-channels. If the number of sub-channels is sufficiently high, each sub-channel has a quasi-flat frequency response and the equalizer complexity could be reduced. This idea was proposed in the mid-1950s by M.L. Doelz [1, 18]. The MCM is also known as FBM because the transceiver has a filter bank structure.

Early MCM applications were high-frequency military systems and voice bandwidth data communications in the Collins Kineplex system [19]. In the recent years the research on MCM is significantly grown in response to the increasing demand for broadband telecommunication services, both over wireline and wireless channels.

This Chapter is organized as follows. In Sec. 2.2, the general architecture of a filter bank transceiver is reported. Starting from the general scheme, we derive two particular modulation architectures. In Sec. 2.3, the OFDM is reported. This scheme is characterized by an efficient frequency domain implementation. In Sec. 2.4, the FMT scheme is reported. This scheme is characterized by a high frequency confinement of the sub-channels.

2.2 General Filter Bank Architecture

In this Section, we consider the baseline architecture of a FBM transceiver. The baseband scheme is shown in Fig. 2.1. The high data rate signal, denoted as $a(nT)$, is composed of a series of symbols belonging to a certain constellation, e.g. M-QAM. The signal $a(nT)$ is, then, serial-to-parallel converted to obtain K parallel branches. Thus, from the signal $a(nT)$ a series of K low data signals are obtained. We denote the n-th symbol of the k-th low rate signal as $a^{(k)}(nNT)$. To simplify the notation, the sampling rate, denoted as T, is

assumed to be unit, i.e. $T = 1$. Each sub-channel signal is interpolated by a factor N and, then, filtered with a prototype pulse $g(n)$. The outputs of these filters represent the baseband sub-channel signals. Now, the available bandwidth is partitioned in K disjointed sub-channels. Each baseband signal produced by the filter bank is translated, in frequency domain, into the suitable sub-channel. This frequency translation is performed by a complex exponential multiplication. Finally, the signals coming from the K branches are summed together to yield the transmitted signal $x(n)$. Mathematically, this signal can be written as

$$x(n) = \sum_{k=0}^{K-1} \sum_{\ell \in \mathbb{Z}} a^{(k)}(\ell N) g(n - \ell N) W_K^{-nk}, \quad n \in \mathbb{Z}, \tag{2.1}$$

where $W_K^{-nk} = e^{i2\pi nk/K}$ is the complex exponential function and i is the imaginary unit.

The transmitted signal in (2.1) is digital-to-analog converted and sent to the transmission medium. At the receiver, the signal is first analog-to-digital converted to obtain

$$y(n) = x * h_{ch}(n) + \eta(n), \quad n \in \mathbb{Z}, \tag{2.2}$$

where $*$, $h_{ch}(n)$ and $\eta(n)$ are the linear convolution operator, the discrete-time channel impulse response and the discrete-time background noise, respectively. In general, the channel impulse response can be written as

$$h_{ch}(n) = \sum_{p=0}^{P-1} \alpha_p(n) \delta(n - p), \tag{2.3}$$

where $\alpha_p(n)$ is the p-th channel coefficient.

The received signal in (2.2) is successively processed with an analysis filter bank. First, it is multiplied with a parallel bank of complex exponential functions. In this way, each sub-channel signal is translated into the baseband. Then, each branch is filtered with a prototype pulse $h(n)$. Finally, the filter outputs are sub-sampled by a factor N to obtain the demodulator output. To determine the transmitted symbol, a decision element could be applied to each sub-channel. Mathematically, we have

$$z^{(k)}(nN) = \sum_{m \in \mathbb{Z}} y(m) h(nN - m) W_K^{mk}, \quad n \in \mathbb{Z}. \tag{2.4}$$

In equations (2.1) and (2.4), the cascade between the prototype filter and the complex exponential function (and viceversa at the receiver) can be com-

bined as

$$g^{(k)}(n) = g(n)W_K^{-kn}, \tag{2.5}$$

$$h^{(k)}(n) = h(n)W_K^{kn}. \tag{2.6}$$

Equations (2.5) and (2.6) represent the frequency domain translation of the baseband prototype pulse. Replacing these equations in (2.1) and (2.4) allows to obtain

$$\begin{aligned}\tilde{z}^{(i)}(nN) &= \sum_{m\in\mathbb{Z}} y(m)h^{(i)}(nN-m) \\ &= \sum_{k=0}^{K-1}\sum_{\ell\in\mathbb{Z}} \tilde{a}^{(k)}(\ell N)\sum_{p\in\mathbb{Z}} g^{(k)}(p-\ell N) \\ &\times \sum_{m\in\mathbb{Z}} h_{ch}(m-p)h^{(i)}(nN-m) + \sum_{m\in\mathbb{Z}} \eta(m)h^{(i)}(nN-m),\end{aligned} \tag{2.7}$$

where

$$\tilde{z}^{(i)}(nN) = W_K^{nNi} z^{(i)}(nN), \quad \tilde{a}^{(k)}(\ell N) = W_K^{-\ell Nk} a^{(k)}(\ell N). \tag{2.8}$$

From (2.7), the received noise for the i-th sub-channel can be written as

$$\eta^{(i)}(nN) = \sum_{m\in\mathbb{Z}} \eta(m)h^{(i)}(nN-m). \tag{2.9}$$

Finally, we can define the equivalent filter between the k-th transmitted signal and the i-th received signal as

$$g_{eq}^{(k,i)}(nN) = g^{(k)} * h_{ch} * h^{(i)}(nN). \tag{2.10}$$

Replacing (2.10) in (2.7) allows to separate the useful term from the interference. In details, we have

$$\tilde{z}^{(i)}(nN) = \tilde{a}^{(k)}(nN)g_{eq}^{(i,i)}(0) + \mathrm{ISI}^{(i)}(nN) + \mathrm{ICI}^{(i)}(nN) + \eta^{(i)}(nN), \tag{2.11}$$

where

$$\mathrm{ISI}^{(i)}(nN) = \sum_{\substack{\ell\in\mathbb{Z}\\ \ell\neq n}} \tilde{a}^{(k)}(\ell N)g_{eq}^{(i,i)}(nN-\ell N) \tag{2.12}$$

$$\mathrm{ICI}^{(i)}(nN) = \sum_{\substack{k=0\\ k\neq i}}^{K-1}\sum_{\ell\in\mathbb{Z}} \tilde{a}^{(k)}(\ell N)g_{eq}^{(k,i)}(nN-\ell N). \tag{2.13}$$

From (2.11), we can note that the received symbol at time instant nN in the i-th sub-channel is equal to the transmitted symbol at the time instant nN in the same sub-channel multiplied by the constant $g_{eq}^{(i,i)}(0)$ plus an inter-symbol interference term $\mathrm{ISI}^{(i)}(nN)$ plus an inter-carrier interference term $\mathrm{ICI}^{(i)}(nN)$ plus the background noise filtered with the receiver prototype pulse $\eta^{(i)}(nN)$.

2.3 OFDM

OFDM is the most popular FBM scheme. The first OFDM scheme was conceived in 1966 by Robert W. Chang [20]. In his work, Chang proposed the idea of orthogonal multiplexing with band-limited signals. The efficient OFDM implementation, one of the OFDM strengths, was published in 1971 by Weinstein and Ebert [21]. OFDM is widely used in several standards, both for wireless and wired communications.

The OFDM scheme can be viewed as a particular case of a FBM architecture described in Sec. 2.2. In OFDM the interpolation factor and the sub-channels number are equal, i.e. $K = N$. In this case, the filter bank is known as critically sampled. The prototype pulses $g(n)$ and $h(n)$ are chosen as a rectangular window. In details, the pulses are defined as

$$\begin{cases} g(n) = \text{rect}(n/N) \\ h(n) = g(-n) \end{cases}, \tag{2.14}$$

where the rect function is defined as

$$\text{rect}(n/N) = \begin{cases} 1 & \text{for } n \in \{0, \ldots, N-1\} \\ 0 & \text{otherwise} \end{cases}. \tag{2.15}$$

As example, in Fig. 2.2 we show the frequency response of the prototype pulses for $K = 8$.

Replacing (2.14) in (2.1) allows to determine the efficient implementation. The symbols are processed in blocks of K elements. The transmitted signal related to the ℓ-th block read

$$\begin{gathered} x_\ell(n) = \sum_{k=0}^{K-1} a^{(k)}(\ell N) W_K^{-nk}, \\ \ell \in \mathbb{Z}, n \in \{0, \ldots, N-1\}, . \end{gathered} \tag{2.16}$$

In (2.16), it is immediate to identify the inverse DFT (IDFT) that can be efficiently implemented exploiting the Fast Fourier Transform (FFT) algorithm. Under assumption of ideal conditions, i.e. non-dispersive channel, the receiver is implemented with a DFT. The received symbols of the n-th block reads

$$\begin{gathered} z^{(i)}(nN) = \sum_{m=0}^{K-1} y_n(m) W_K^{mi}, \\ \ell \in \mathbb{Z}, n \in \{0, \ldots, N-1\}, . \end{gathered} \tag{2.17}$$

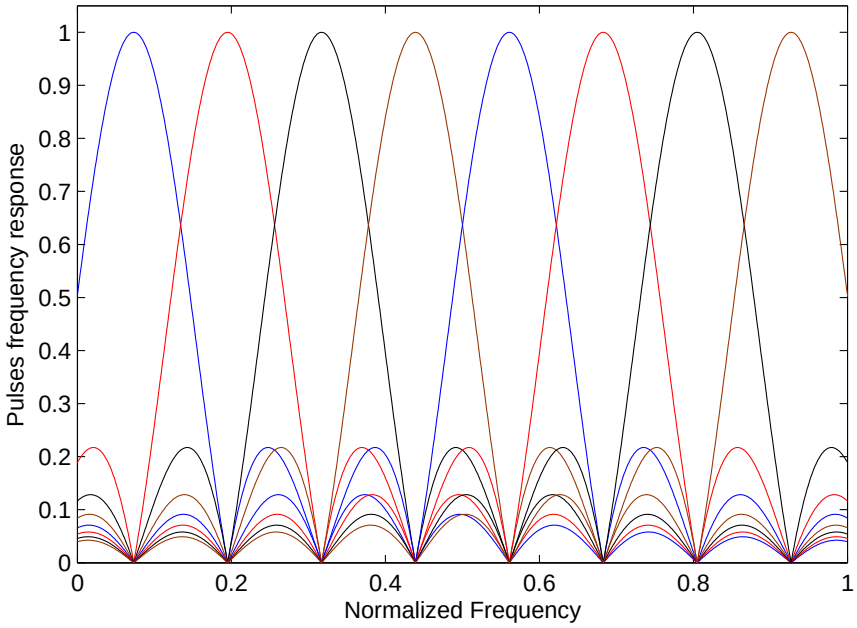

Figure 2.2: OFDM prototype pulses freq. response magnitude for $K = 8$.

where $y_n(m)$ is the n-th block of the received signal.

OFDM scheme is orthogonal only in ideal conditions. When the channel is frequency selective, the orthogonality is lost and ISI and inter-carrier interference (ICI) are present. To solve this problem, in 1980 Peled and Ruiz introduced a cyclic extension for every transmitted block. This idea is commonly known as CP [22]. Recalling the prototype pulses from (2.14), the CP introduction is equivalent to using the prototype pulses that follow:

$$\begin{cases} g(n) = \text{rect}\left(n/(N+\mu)\right) \\ h(n) = \text{rect}\left(-(n+\mu)/N\right) \end{cases}, \tag{2.18}$$

where μ is the cyclic prefix length, expressed in number of samples. If the CP in greater than the channel impulse response length, i.e. $\mu \geq P - 1$, the OFDM scheme is orthogonal and there are no ISI and ICI. The efficient OFDM implementation, including CP, is shown in Fig. 2.3.

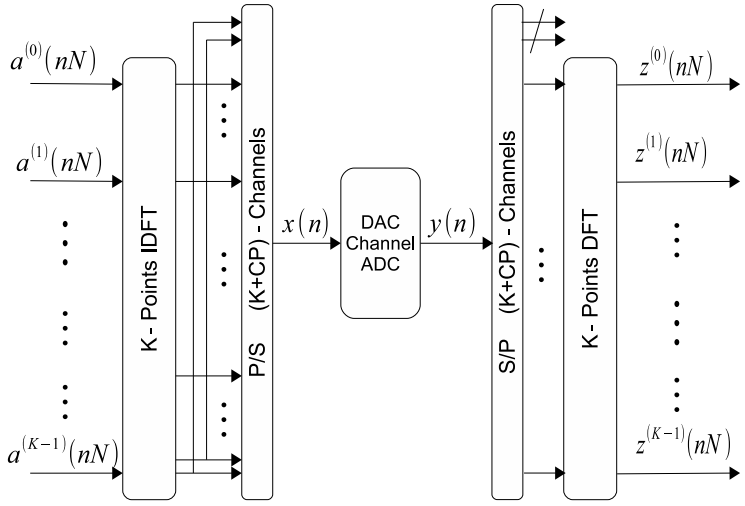

Figure 2.3: OFDM efficient implementation.

2.4 Filtered Multitone Modulation

FMT is another FBM. In FMT, the sub-carriers are uniformly spaced and the prototype pulses are identical among the sub-channels. FMT was initially proposed in 2002 for transmission over broadband wireline channels, i.e. for very-high-bit-rate digital subscriber line (VDSL) [3]. In the next years, FMT was studied for wireless [4, 5] and Power Line [23, 24] communications.

In contrast to OFDM, where the time domain confinement is preferred, FMT is characterized by high frequency confinement of the sub-channels. When the sub-channel frequency confinement is high, the ICI between different sub-channels is lower. In addition, the out-of-band interference is reduced. This aspect has an important implication in wireless and PLC. In fact, the standards could set several parts of the spectrum where the power of the transmitted signal must be reduced (or totally notched) to generate low emissions and to allow the coexistence with other systems. If the sub-channels have high frequency confinement, the number of sub-channels that need to be notched will be reduced w.r.t. OFDM. This implies that the data rate penalty is smaller.

A common choice is to use a root raised cosine (RRC) prototype pulse. Transmitter pulse $g(n)$ and receiver pulse $h(n)$ are matched, i.e. $h(n) = g^*(-n)$. Thus, both filters are RRC. The frequency response of the RRC

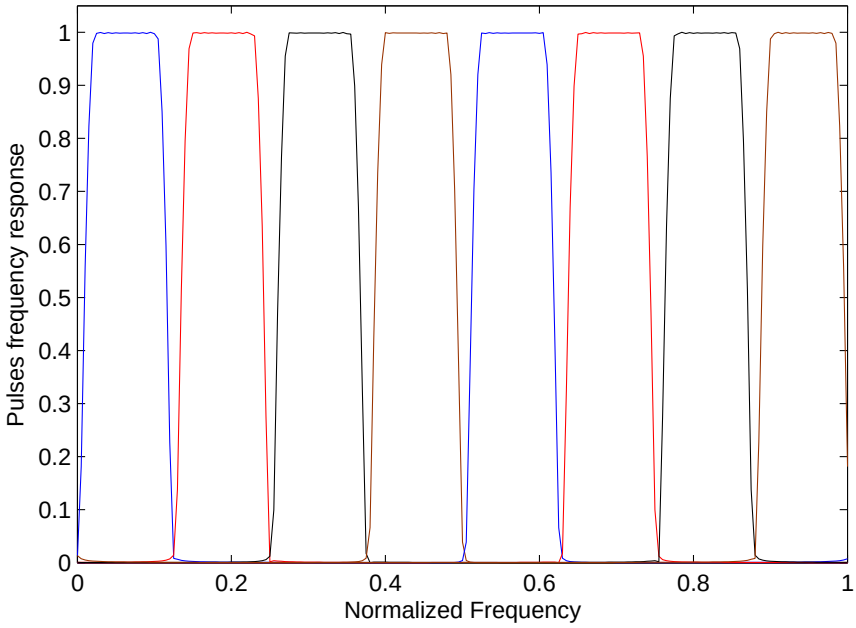

Figure 2.4: FMT prototype pulses frequency response (RRC) for $K = 8, N = 10, \beta = 0.20$ and filter length equal to $20N$.

pulse is defined as

$$\hat{G}(f) = \begin{cases} 1 & |f| \leq \frac{1-\beta}{2} \\ \sqrt{\frac{T}{2}\left[1 + \cos\left(\frac{\pi}{\beta}\left[|f| - \frac{1-\beta}{2}\right]\right)\right]} & \frac{1-\beta}{2} < |f| \leq \frac{1+\beta}{2}, \\ 0 & \text{otherwise} \end{cases} \quad f \in \mathbb{R}, \quad (2.19)$$

where $\beta \in [0, 1]$ is the roll-off factor. We note that when $\beta = 0$, we obtain a rectangular window in frequency domain. On the other hand, when $\beta = 1$, the frequency response has a sinusoidal shape. As example, in Fig. 2.4, we show the pulses frequency response for $K = 8, N = 10, \beta = 0.20$ and filter length equal to $20N$.

Clearly, to obtain high sub-channel frequency confinement, long prototype pulses are required. In such a case, the implementation complexity may increase significantly. Therefore, the efficient FMT implementation as well as the design of good pulses is an important problem [25, 26, 27, 28, 29].

Chapter 3

Cyclic Block FMT

3.1 Introduction

In this chapter, a novel filter bank modulation scheme is described. The ambitious goal is to merge the strengths of both OFDM and FMT, described in Ch. 2. We refer to it as cyclic block filtered multitone modulation (CB-FMT). Similarly to conventional FMT, CB-FMT aims at generating well frequency localized sub-channels. However, differently from it, CB-FMT transmits data symbols in blocks, and the filter bank does not use linear convolutions but cyclic convolutions. Similarly to OFDM, the block transmission can reduce latency, but the sub-channel frequency confinement is much higher, more similarly to FMT. This translates in higher spectral selectivity, more confined power spectral density, and lower PAPR than in OFDM given the same target spectral efficiency. Furthermore, the implementation complexity is lower than that in FMT with the same number of sub-channels and even with longer pulses. In fact, an efficient realization can be devised if both the synthesis and the analysis filter banks in CB-FMT are implemented in the frequency domain (FD) via a concatenation of an inner (with respect to (w.r.t.) the channel) DFT and a bank of outer DFTs. Such a FD architecture enables the use of a FD sub-channel equalizer designed according to the zero forcing (ZF) or the minimum mean square error (MMSE) criterion [30]. In particular, the ZF solution will restore perfect orthogonality if a cyclic prefix (similarly to OFDM) is appended to each block of signal coefficients that are transmitted over a dispersive (frequency selective) channel. In the presence of channel time variations (because of mobility), the ICI is small due to the sub-channel frequency confinement so that the sub-channel equalizer is sufficient to cope with the ISI experienced by the data symbols transmitted in a block. This

equalization scheme is capable of coherently collecting the sub-channel energies so that frequency and time diversity, offered by the fading channel, can be exploited. Consequently, this can provide better performance, i.e., lower symbol error rate and higher achievable rate, than OFDM.

The CB-FMT idea and principles were originally presented in [31].

Another FBM scheme referred to as Generalized Frequency Division Multiplexing (GFDM) has been independently presented in [32]. According to [32], GFDM is a FBM scheme that uses a non-orthogonal design where the sub-channel spacing is smaller than the sub-channel Nyquist band. It can be viewed as an FMT scheme operating beyond the critical sample rate. An extended CP is used to take into account the pulse tails and allow the implementation of a so-called tail biting convolution. The tail biting convolution in turn can be implemented with a circular convolution. Since the design is not orthogonal, ICI is present also in an ideal channel which requires some form of equalization to mitigate it. This may yield performance that is worse than OFDM. However, it is shown in [32] that other benefits are offered by GFDM as spectrum agility and lower PAPR. CB-FMT is a more general architecture than GFDM that shares the idea of using circular convolutions instead of linear convolutions. As FMT essentially represents a general exponentially modulated filter bank with linear convolutions, CB-FMT represents a general exponentially modulated filter bank with circular convolutions. An orthogonal CB-FMT system can be designed (as done in this chapter) without requiring the use of a CP unless more robustness is desirable in time dispersive channels. Orthogonal CB-FMT can offer lower SER and higher spectral efficiency compared to OFDM.

This chapter is organized as follows:

- The CB-FMT key elements are described in Section 3.2. These include the derivation of an efficient frequency domain implementation starting from the time domain signal representation (Section 3.2.1).
- Relations between CB-FMT and conventional FMT/OFDM are briefly described in Section 3.2.2 to better understand the differences.
- The complexity analysis is carried out in Section 3.2.3.
- The conditions under which the CB-FMT scheme is orthogonal are studied in Section 3.3. Herein, a simple orthogonal pulse design is also proposed. The orthogonality problem is extensively considered in Ch. 4.
- The analytic derivation of the CB-FMT PSD and the PAPR are discussed in Section 3.4.

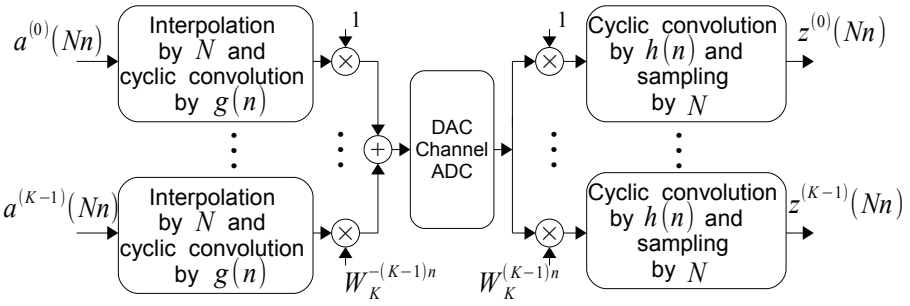

Figure 3.1: CB-FMT transceiver scheme.

- Several numerical examples, which include pulse shapes, complexity, PSD and PAPR are collected in Section 3.5.

3.2 Cyclic block FMT modulation

Cyclic block filtered multitone modulation is a multicarrier modulation scheme.

The principle of CB-FMT is depicted in Figure 3.1. In this scheme, the low data rate sequences are interpolated by a factor N and, then, filtered with a prototype pulse that is identical for all sub-channels. Differently from conventional FMT, the convolutions in the filter bank are circular. The filter outputs are multiplied by a complex exponential to obtain a spectrum translation. Finally, the K modulated signals are summed together yielding the transmitted discrete time signal.

The circular convolution involves periodic signals, and it can be efficiently realized in the frequency domain via the DFT. To use the circular convolution, a blockwise transmission is needed. Thus, we gather the low data rate sequences in blocks of L symbols $a^{(k)}(\ell N)$, $\ell \in \{0, \ldots, L-1\}$, for each sub-channel. Then, we consider the prototype pulse $g(n)$ to be a causal finite impulse response (FIR) filter, with a number of coefficients equal to $M = LN$. If the length is lower than M, we can extend the pulse length to M with zero-padding, without loss of generality. The CB-FMT transmitted signal can be

written as

$$\begin{aligned} x(n) &= \sum_{k=0}^{K-1} \left[a^{(k)} \otimes g\right](n) \\ &= \sum_{k=0}^{K-1} \sum_{\ell=0}^{L-1} a^{(k)}(\ell N) g((n-\ell N)_M) W_K^{-nk}, \\ & n \in \{0, \ldots, M-1\}, \end{aligned} \tag{3.1}$$

where $\otimes$ denotes the circular convolution operator and $g((n)_M)$ denotes the cyclic (periodic) repetition of the prototype pulse $g(n)$ with a period equal to M, i.e., $g((n)_M) = g(\mathrm{mod}(n, M))$ where $\mathrm{mod}(\cdot, \cdot)$ is the integer modulo operator.

The signal $x(n)$ is digital-to-analog converted and, then, transmitted over the transmission medium. At the receiver, after analog-to-digital conversion, the discrete time received signal, denoted with $y(\ell)$, is defined as in 2.2. In the following, we assume the channel response to be ideal. The more general case will be discussed in Chapter 5.

Similarly to the synthesis stage, we can apply the circular convolution to the analysis filter bank. The k-th sub-channel output is obtained as follows:

$$\begin{aligned} z^{(k)}(nN) &= \sum_{\ell=0}^{M-1} y(\ell) W_K^{\ell k} h((nN-\ell)_M), \\ & k \in \{0, \ldots, K-1\}, \quad n \in \{0, \ldots, L-1\}, \end{aligned} \tag{3.2}$$

where $h((n)_M)$ denotes the periodic repetition of the prototype analysis pulse $h(n)$ with period M.

Each sub-channel conveys a block of L data symbols over a time period equal to LNT. Therefore, the transmission rate equals $R = K/(NT)$ symbols/s. More generally, a cyclic prefix can be added (but it is not mandatory) to the transmitted signal, as explained in Chapter 5. In this case, the rate equals

$$R = \frac{KL}{(M+\mu)T} \quad \text{symbols/s}, \tag{3.3}$$

where μ is the cyclic prefix length in samples.

3.2.1 Frequency domain implementation

One of the goals in CB-FMT is the reduction of the computational complexity in the filtering operation w.r.t. the conventional FMT scheme. This can be

achieved by exploiting a frequency domain implementation of the system as described in the following.

Firstly, we define a constant integer Q subject to

$$M = LN = KQ. \tag{3.4}$$

Condition 3.4 imposes that $K/N = L/Q$. Thus, we can choose $L = \alpha K$ and $Q = \alpha N$, where α is an appropriate constant. If $\alpha \in \mathbb{Z}, \alpha > 0$, every α value gives a valid set of parameters.

Then, the M-point DFT of the transmitted signal in (3.1) is computed. We obtain

$$\begin{aligned} X(i) &= \sum_{n=0}^{M-1} x(n) W_M^{ni} \\ &= \sum_{n=0}^{M-1} \sum_{k=0}^{K-1} \sum_{\ell=0}^{L-1} a^{(k)}(\ell N) g((n-\ell N)_M)\, W_K^{-kn} W_M^{ni}, \\ i &\in \{0, \ldots, M-1\}. \end{aligned} \tag{3.5}$$

Under the assumption $M = KQ$, we can write

$$X(i) = \sum_{k=0}^{K-1} \sum_{\ell=0}^{L-1} a^{(k)}(\ell N) \sum_{n=0}^{M-1} g((n-\ell N)_M) W_M^{(i-kQ)n}. \tag{3.6}$$

We now multiply and divide (3.6) by $W_M^{(i-kQ)\ell N}$ to obtain

$$\begin{aligned} X(i) &= \sum_{k=0}^{K-1} \sum_{\ell=0}^{L-1} a^{(k)}(\ell N) \sum_{n=0}^{M-1} g((n-\ell N)_M)\, W_M^{(i-kQ)(n-\ell N)} W_M^{(i-kQ)\ell N} \\ &= \sum_{k=0}^{K-1} \sum_{\ell=0}^{L-1} a^{(k)}(\ell N) G(i-kQ) W_M^{(i-kQ)\ell N}, \end{aligned} \tag{3.7}$$

where in (3.7) we denoted by $G(i)$ the M-point DFT of the pulse $g(n)$.

Since $M = LN$, it should be noted that the summation with index ℓ in (3.7) is the L-point DFT of the data block $a^{(k)}(Nn)$ cyclically shifted by kQ, i.e.,

$$A^{(k)}(i-kQ) = \sum_{\ell=0}^{L-1} a^{(k)}(\ell N) W_L^{(i-kQ)\ell}. \tag{3.8}$$

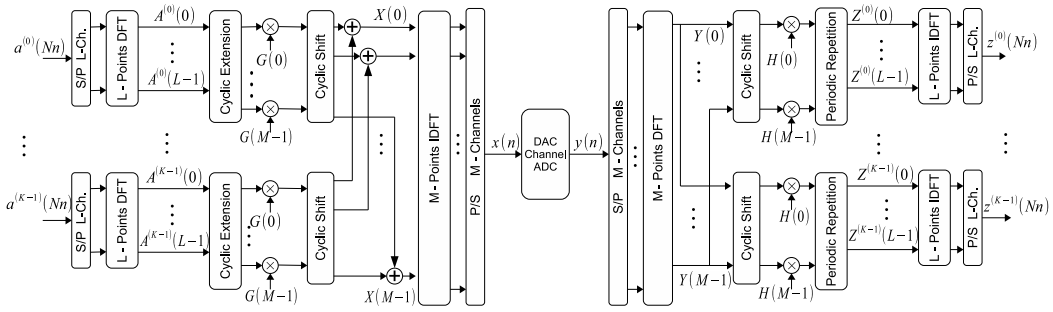

Figure 3.2: General frequency domain implementation of the CB-FMT transceiver.

Finally, substituting (3.8) in (3.7), we obtain

$$X(i) = \sum_{k=0}^{K-1} A^{(k)}(i - kQ)G(i - kQ), \quad i \in \{0, \ldots, M-1\}. \tag{3.9}$$

This suggests an implementation of the CB-FMT synthesis filter bank as shown in Figure 3.2. For each sub-channel block of data, we apply an L-point DFT (referred to as outer DFT). We extend cyclically the block of coefficients at the output of the outer DFT from L points to M points. Then, each sub-channel block of M coefficients is weighted with the M coefficients $G(i)$ of the prototype pulse DFT. Next, each sub-channel block is cyclically shifted by a factor $-kQ$, where k is the sub-channel index. Finally, the shifted blocks are summed together, and an M-point IDFT (referred to as inner IDFT) is applied to obtain the signal to be transmitted.

If we assume the M-point DFT of the prototype pulse to be confined in Q points, i.e., $G(i) \neq 0$ for $i \in \{0, \ldots, Q-1\}$ and $G(i) = 0$ for $i \in \{Q, \ldots, M-1\}$, we can simplify (3.9) into

$$\begin{aligned} X(i) &= A^{(k)}(i - kQ)G(i - kQ), \\ &\quad i \in \{kQ, \ldots, (k+1)Q - 1\}, \quad k \in \{0, \ldots, K-1\}. \end{aligned} \tag{3.10}$$

This suggests an efficient implementation of the CB-FMT synthesis filter bank as shown in Figure 3.3. For each sub-channel block of data, we apply an L-point DFT (referred to as outer DFT). We extend cyclically the block of coefficients at the output of the outer DFT from L points to Q points. Then, each sub-channel block of Q coefficients is weighted with the Q non-zero coefficients $G(i)$ of the prototype pulse DFT. Finally, we apply an M-point IDFT (referred to as inner IDFT) to obtain the signal to be transmitted.

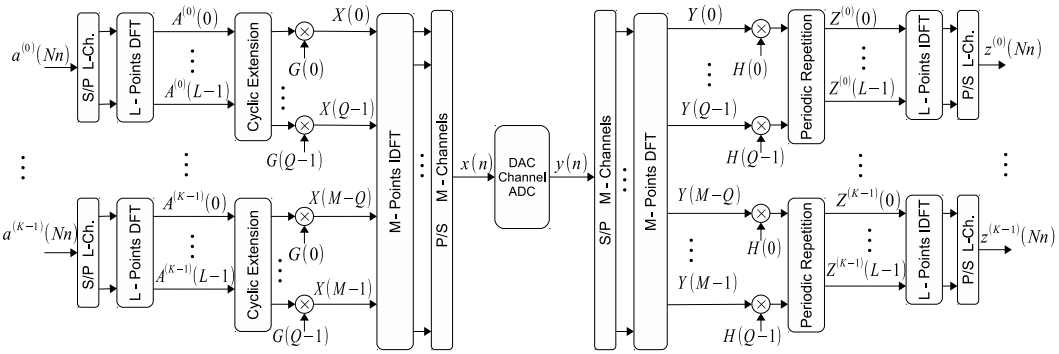

Figure 3.3: Efficient frequency domain implementation of the CB-FMT transceiver. This implementation is valid when the M-point DFT of the prototype pulse has only Q non-zero coefficients.

The analysis filter bank can also be implemented in the frequency domain. We start from (3.2) and we substitute the signal $y(\ell)$ with the IDFT of its frequency response as follows:

$$z^{(k)}(nN) = \sum_{\ell=0}^{M-1} \sum_{i=0}^{M-1} Y(i) W_M^{-\ell i} W_K^{\ell k} h((nN-\ell)_M), \tag{3.11}$$
$$k \in \{0, \ldots, K-1\},$$
$$n \in \{0, \ldots, L-1\}.$$

Assuming $M = KQ$, we can write

$$z^{(k)}(nN) = \sum_{i=0}^{M-1} Y(i) \sum_{\ell=0}^{M-1} h((nN-\ell)_M)\, W_M^{-(i-kQ)\ell}. \tag{3.12}$$

Now, we multiply and divide (3.12) by $W_M^{-(i-kQ)nN}$ to obtain

$$z^{(k)}(nN) = \sum_{i=0}^{M-1} Y(i) \sum_{\ell=0}^{M-1} h((nN-\ell)_M)\, W_M^{-(i-kQ)(\ell-nN)} W_M^{-(i-kQ)nN}, \tag{3.13}$$

where in (3.13) we can recognize the shifted version of the M-point DFT of $h(\ell)$ defined as

$$H(i-kQ) = \sum_{\ell=0}^{M-1} h((nN-\ell)_M)\, W_M^{-(i-kQ)(\ell-nN)}, \tag{3.14}$$
$$i \in \{0, \ldots, M-1\},$$
$$k \in \{0, \ldots, K-1\},$$

where the second equality holds since the signals are periodic of M. Considering that $M = LN$, we have that $W_M^{-(i-kQ)nN} = W_L^{-(i-kQ)n}$, and we can write

$$\begin{aligned} z^{(k)}(nN) &= \sum_{i=0}^{M-1} Y(i)H(i-kQ)W_L^{-(i-kQ)n} \\ &= \sum_{i=0}^{M-1} Y(i+kQ)H(i)W_L^{-in}, \qquad (3.15) \\ i &\in \{0,\ldots,M-1\}, \\ k &\in \{0,\ldots,K-1\}. \end{aligned}$$

The index i can be decomposed into two indexes p and q as $i = p + Lq$, with $p \in \{0,\ldots,L-1\}$ and $q \in \{0,\ldots,N-1\}$, to obtain

$$z^{(k)}(nN) = \sum_{p=0}^{L-1}\sum_{q=0}^{N-1} Y(p+qL+kQ)\ H(p+qL)W_L^{-pn}. \qquad (3.16)$$

In (3.16), we can recognize the L-point IDFT of the signal $Z^{(k)}(p)$ that is given by

$$\begin{aligned} Z^{(k)}(p) &= \sum_{q=0}^{N-1} Y(p+qL+kQ)H(p+qL), \qquad (3.17) \\ p &\in \{0,\ldots,L-1\}, \\ k &\in \{0,\ldots,K-1\}. \end{aligned}$$

This is the periodic repetition with period L of the signal $Y(i)H(i-kQ)$. Therefore, the receiver can be summarized as follows (Figure 3.2): Firstly, the received signal $y(n)$ is processed with an M-point DFT. Then, the output coefficients are weighted with the prototype pulse M-point DFT coefficients $H(i)$. Next, a periodic repetition with period L is performed for each sub-channel block of coefficients to obtain (3.17), where $Y(p)$ is the M-point DFT of the received signal.

Finally, to obtain the k-th sub-channel output, an L-point IDFT is applied to (3.17), i.e.,

$$\begin{aligned} z^{(k)}(nN) &= \sum_{p=0}^{L-1} Z^{(k)}(p)W_L^{-pn}, \qquad (3.18) \\ n &\in \{0,\ldots,L-1\}, \quad k \in \{0,\ldots,K-1\}. \end{aligned}$$

Assuming that the analysis pulse has only Q non-zero coefficients, i.e., $H(i) = 0$ for $i \in \{Q, \ldots, M-1\}$, as when the pulse is matched to the synthesis pulse and equal to $G^*(i)$, the pulse weighting and the periodic repetition take place on each sub-channel as graphically depicted in Figure 3.3. In particular, assuming $Q > L$, (3.17) corresponds to adding at the beginning of the block of coefficients $Y(i+kQ)H(i)$, $i \in \{0, \ldots, Q-1\}$ the last $Q-L$ coefficients of the same block.

With the orthogonal design that we describe in Section 3.3, i.e., when $H(i) = G^*(i)$ and assuming that orthogonality conditions are satisfied, we obtain

$$z^{(k)}(nN) = \sum_{q=0}^{Q-1} |G(q)|^2 a^{(k)}(nN) + N^{(k)}(nN), \tag{3.19}$$

which shows that the output sample is equal to the n-th data symbol of the k-th sub-channel weighted by the pulse energy, plus a noise contribution. More generally, when the transmission medium is not ideal, equalization can be performed (see Chapter 5) so that in (3.19) the coefficient that weights the data symbol is given by the sub-channel energy.

Also the FMT system can be implemented in the frequency domain. However, the presence of linear convolutions renders it more complex since an overlap-and-add operation has to be carried out as shown in [33].

As a final remark, the use of inner and outer DFTs appeared also in the concatenated OFDM-FMT architecture presented in [5].

3.2.2 Relation with FMT and OFDM

In the following, we briefly highlight the main differences between CB-FMT and FMT and OFDM:

Relation with FMT. Similarly to conventional FMT, CB-FMT targets the use of frequency confined sub-channels. However, while the filter banks in FMT deploy linear convolutions, in CB-FMT, the filter banks use cyclic convolutions. Therefore, the FMT transmitted signal does not read as in (3.1) but as follows:

$$x(n) = \sum_{k=0}^{K-1} \sum_{\ell \in \mathbb{Z}} a^{(k)}(\ell N) g(n - \ell N) W_K^{-nk}, \quad n \in \mathbb{Z}, \tag{3.20}$$

where $g(n)$ is the prototype pulse. Furthermore, while in FMT the transmission is typically continuous, in CB-FMT, data signals are transmitted in blocks, each of the K sub-channels transmits a block of L data symbols.

In FMT, the rate equals

$$R = \frac{K}{NT} \quad \text{symbols/s.} \tag{3.21}$$

The efficient implementation of FMT can exploit a polyphase DFT filter bank architecture [29]. Nevertheless, the FMT complexity is higher than the CB-FMT complexity, as shown in Section 3.2.3 assuming the same number of sub-channels and the same prototype pulse length.

In CB-FMT, very simple frequency domain design can be followed to obtain an orthogonal solution as shown in Section 3.3. In FMT, the orthogonal design is more complicated [28, 29]. Thus, non-orthogonal solutions are often adopted in FMT as for instance the use of a truncated root-raised-cosine prototype pulse [3] or *ad hoc* frequency localized pulses [26, 27].

When transmission is in time/frequency-selective fading channels, the good sub-channel frequency confinement in FMT provides robustness to ICI, while the residual ISI can be mitigated with sub-channel linear equalization [3] or maximum *a posteriori* sequence estimation [4, 34]. In CB-FMT, instead, simple frequency domain equalization can be adopted as described in Chapter 5.

Relation with OFDM. In OFDM, the filter bank privileges the sub-channel time domain localization, rather than the frequency domain localization. Furthermore, OFDM can be seen as a particular case of both FMT and CB-FMT. In fact it corresponds to an FMT system with $N = K$ and the prototype pulse being a rectangular window, i.e., $g(n)$ is equal to 1 for $n \in \{0, \ldots, N-1\}$ and 0 otherwise. It follows that the transmitted signal can be expressed as

$$x(n) = \sum_{k=0}^{K-1} a^{(k)}(\ell N) W_K^{-nk}, \quad n \in \{\ell N, \ldots, (\ell+1)N - 1\}\,. \tag{3.22}$$

Starting from CB-FMT, we obtain OFDM by setting $N = K$, $L = Q = 1$, and $G(0) = 1$, so that we also have $K = M$.

In OFDM, the rate equals

$$R = \frac{K}{(K+\mu)T} \quad \text{symbols/s,} \tag{3.23}$$

where μ is the cyclic prefix length in samples. It should be noted that cyclic prefix is not necessarily of equal length in CB-FMT and in OFDM. The same applies to the number of data sub-channels that can be different in the two systems.

Latency

In future communication systems, the latency requirement is of primal importance. CB-FMT and OFDM adopt a blockwise transmission. Thus, a latency is introduced. In OFDM, the latency is related to the sub-channels number and it reads

$$\tau_{\text{latency, OFDM}} = (K + \mu)T \quad \text{seconds.} \tag{3.24}$$

In CB-FMT, latency is related to the prototype pulse length and it reads

$$\tau_{\text{latency, CB-FMT}} = (M + \mu)T \quad \text{seconds.} \tag{3.25}$$

In OFDM, low-latency can be obtained with a low number of sub-channels. In CB-FMT, there are two different possibility to decrease the latency. Both modes decrease the filter length M.

- Similarly to OFDM, low-latency can be obtained with a low number of sub-channels. Sure enough, from (3.4), $M = KQ$. The number of frequency bins for each sub-channel remains constant.
- Another possibility to have low-latency is to decrease the value of L. Sure enough, in CB-FMT, the sub-channel symbols are gathered in blocks of L elements. Decreasing the block size decreases the latency too. In this case, K and N remain constant.

3.2.3 Computational complexity

In this section, we evaluate the computational complexity of CB-FMT in terms of the number of complex operations [cop] (additions and multiplications) per sample.

Let us assume that an M-point DFT (or IDFT) block has complexity equal to $\alpha M \log_2(M)$ [cop] where, for instance, $\alpha = 1.2$.

At the transmitter, K outer DFTs of L-points are used, together with one M-point inner IDFT. Furthermore, the inner IDFT input signals are weighted by the DFT components of the prototype pulse. Similarly, this applies at the receiver. The operations performed by the cyclic extension are negligible. Let us assume the number of non-zero DFT coeffients of the prototype pulse to be equal to $Q_2 = QC$, $C \in \{1, \ldots, K\}$. Since the transmitted block comprises LN coefficients, the number of complex operations per sample is equal to

$$C_{\text{CB-FMT}} = \frac{K\alpha L \log_2(L) + \alpha M \log_2(M) + S}{LN} \quad \left[\frac{\text{cop}}{\text{sample}}\right], \tag{3.26}$$

where $S = (2C-1)M$ for the transmitter. At the receiver, the periodic repetition increases the complexity by $S = 2MC - KL$ for $(Q-L)C < L$ and by $S = (M+KL)C$ otherwise. When the prototype pulse has only Q non-zero coefficients, i.e., $C = 1$, $S = M$ for the transmitter and $S = 2M - KL$ for the receiver.

As a comparison, we consider the complexity of FMT efficiently implemented with a polyphase DFT filter bank as described in [29]. This is equal to

$$C_{\text{FMT}} = \frac{K\alpha \log_2(K) + 2L_g}{N} \quad \left[\frac{\text{cop}}{\text{sample}}\right], \tag{3.27}$$

assuming K sub-channels, an interpolation factor N, and a prototype pulse with length L_g coefficients. This complexity does not take into account the operations required by the equalization stage.

If, for example, we assume $K = 64$ and $N = 80$ for both systems and furthermore FMT with a pulse length equal to $20N$ while CB-FMT with $L = K$, $Q = N$ resulting in a longer filter length equal to $M = 64N$ coefficients, the receiver complexity will be equal to $\{45.8, 21.7\}$ [cop] respectively for FMT and CB-FMT. This shows the gain in complexity of CB-FMT yet having a longer pulse. More results about the complexity are reported in Section 3.5.2.

3.3 Orthogonality conditions

The frequency domain implementation of CB-FMT allows us to deduce the system orthogonality conditions. A filter bank system is orthogonal when it has the perfect reconstruction property and the transmit-receive filters are matched, i.e., $g(n) = h^*(-n)$ and $H(i) = G^*(i)$, so that the system exhibits neither ISI nor ICI [35].

When the prototype pulse satisfies the following two conditions, the CB-FMT system will be orthogonal:

1. The M-point DFT of the prototype pulse has only Q non-zero coefficients, i.e., $G(i) = 0$ for $i \in \{Q, \ldots, M-1\}$ (sufficient condition).

2. The correlation between $g(n)$ and $g^*(-n)$, computed with the circular convolution and sampled by a factor N, is the Kronecker delta, i.e.,

$$\left[g \otimes g^*_-\right](nN) = \sum_{\ell=0}^{M-1} g((\ell)_M) g^*((nN+\ell)_M) = \delta(n), \tag{3.28}$$

where $\delta(n)$ is the Kronecker delta function, i.e., $\delta(n)$ is equal to 1 for $n = 0$ and 0 otherwise. The proof of these conditions is provided in Chapter 4.

3.3.1 Orthogonal prototype pulse design

The frequency domain implementation and the orthogonality conditions suggest to synthesize the pulse in the frequency domain with a finite number of frequency components.

In this chapter, the root-raised-cosine pulse is considered. We start by choosing a pulse that belongs to the Nyquist class with roll-off β, Nyquist frequency $1/(2NT)$, total bandwidth $1/(KT)$, and frequency response $\hat{G}(f)$, defined in 2.19. Then, we set M. The coefficients in the frequency domain of the CB-FMT prototype pulse are obtained by sampling the response $\sqrt{\hat{G}(f)}$, i.e., $G(i) = \sqrt{\hat{G}(i/(MT))}$ with $i \in \{0, \ldots, M-1\}$. To satisfy the orthogonality conditions, only Q out of M coefficients are non-zero, while $L < Q$ coefficients fall in the band $1/(NT)$. It should also be noted that there is a limiting condition on the choice of the roll-off β. In fact, the maximum roll-off to prevent the pulse tails from exceeding the bandwidth $1/(KT)$ of Q-points is $\beta_{\max} = (Q - L)/Q$. Therefore, we must choose $\beta \leq \beta_{\max}$.

We recall that the parameters of CB-FMT are related to each other through the relation $M = LN = KQ$, which can be rearranged as

$$\frac{N}{K} = \frac{Q}{L} = \frac{p}{q}, \tag{3.29}$$

where p and q are relative prime integers. Therefore, once we have chosen M, the number of sub-channels K, and the ratio N/K, we obtain the rest of the parameters N, Q, L.

Some examples of pulse responses are reported in Section 3.5.1. In particular, complex asymmetric pulses are also considered. It is also interesting to note that a trivial orthogonal solution is obtained by using a rectangular FD window of Q non-zero coefficients. In time domain, the FD rectangular pulse is given by

$$g(n) = e^{i\pi n(Q-1)/M} \frac{\sin(\pi n Q/M)}{\sin(\pi n/M)}. \tag{3.30}$$

In such a case, the CB-FMT scheme becomes the dual of the OFDM system that uses, instead, a rectangular window in the time domain.

3.4 PSD- and PAPR-related aspects

3.4.1 PSD-related aspects

In this section, we study the power spectral density (PSD) of the transmitted CB-FMT signal. The PSD is an important aspect to evaluate the confine-

ment of the transmitted spectrum. The objective is to limit the out-of-band emissions. More generally, the PSD must comply to regulatory aspects that typically set an upper limit, also known as spectrum mask, e.g., as in the IEEE 802.11 WLAN standard [36] or in the HomePlug PLC system.

To derive an analytic expression for the PSD of CB-FMT, we can start by expressing the (continuous) transmission of samples $x(n)$ as follows:

$$x(n) = \sum_{m\in\mathbb{Z}} \sum_{k=0}^{M-1} X^{(k)}(mM_1) g_P(n - mM_1) W_M^{nk}, \quad n \in \mathbb{Z}, \tag{3.31}$$

where the sub-channel symbol period $M_1 = M + \mu$ takes into account the fact that a CP of length μ samples can be used for the equalization, as it will be explained in Chapter 5. The CP is appended to the block of coefficients at the inner IDFT output. Furthermore, $X^{(k)}(mM_1)$ are the coefficients at the input of the inner IDFT in the transmitter at time instant mM_1, and $g_P(n)$ is the rectangular window that is equal to 1 for $n \in \{0, \ldots, M_1 - 1\}$ and zero otherwise. Essentially, $X^{(k)}(mM_1)$ represents the block of coefficients defined in (3.10) that is transmitted in the m-th CB-FMT block. The data symbols $a^{(k)}(\ell N)$ are assumed to be independent, identically distributed with zero mean and power equal to $M_a = E[|a^{(k)}(\ell N)|^2]$.

To convert the signal in (3.31) from discrete time to continuous time, an interpolation filter with response $g_I(t)$ is needed. The interpolated signal can be expressed as

$$x(t) = \sum_{n\in\mathbb{Z}} x(n) g_I(t - nT), \quad t \in \mathbb{R}. \tag{3.32}$$

To obtain the signal PSD, the correlation of $x(t)$, defined as

$$r_x(t, \tau) = E\left[x^*(t + \tau) x(t)\right], \tag{3.33}$$

needs to be computed. In (3.33), $E[\cdot]$ denotes the expectation operator. Since the interpolated signal is cyclo-stationary, the correlation is periodic [37], i.e., $r_x(t + T, \tau) = r_x(t, \tau)$. To remove the dependency on the variable t, the mean correlation $\overline{r_x(\tau)} = \frac{1}{T}\int_0^T r_x(t, \tau)\mathrm{d}t$ has to be computed, from which the mean PSD is obtained via a Fourier transform. The mathematical expressions involved in the PSD computation are convoluted. In the following, we report the main steps to obtain the PSD. The final result is given in (3.45) to (3.47).

The correlation can be written as

$$r_x(t, \tau) = \sum_{n,m\in\mathbb{Z}} E\left[x^*(n) x(m)\right] g_I^*(t + \tau - nT) g_I(t - mT), \tag{3.34}$$

where $E\left[x^*(n)x(m)\right]$ represents the correlation of the discrete time transmitted signal before the analog interpolation filter. To compute (3.34), we rewrite (3.31) as

$$x(n) = \sum_{k=0}^{M-1} \sum_{p\in\mathbb{Z}} X^{(k)}(pM_1) g_P^{(k)}(n - pM_1), \tag{3.35}$$

where $g_P^{(k)}(n) = g_P(n)e^{j2\pi nk/M}$. The correlation of (3.35) is given by

$$\begin{aligned} r(n,m) &= E[x^*(n+m)x(n)] \\ &= \sum_{\substack{k_1=0 \\ k_2=0}}^{M-1} \sum_{p_1,p_2\in\mathbb{Z}} E\left[\left(X^{(k_1)}(p_1M_1)\right)^* X^{(k_2)}(p_2M_1)\right] \\ &\qquad \times \left(g_P^{(k_1)}(n+m-p_1M_1)\right)^* g_P^{(k_2)}(n-p_2M_1), \end{aligned} \tag{3.36}$$

where the term $r_X(k_1,p_1,k_2,p_2) = E\left[\left(X^{(k_1)}(p_1M_1)\right)^* X^{(k_2)}(p_2M_1)\right]$ represents the correlation between the signal coefficients at the input of the inner IDFT of the transmitter. We obtain

$$r_X(k_1,p_1,k_2,p_2) = \begin{cases} M_a L \sum_{s=0}^{K-1} G(k_1 - sQ)G^*(k_2 - sQ), & \text{if } \overset{p_1=p_2}{k_1-k_2\in\{0,\pm L,\dots\}} \\ 0, & \text{otherwise} \end{cases}. \tag{3.37}$$

The correlation in (3.36) is periodic, i.e., $r(n,m) = r(n+M_1,m)$. Thus, we compute the mean correlation as

$$\begin{aligned} \overline{r(m)} &= \frac{1}{M_1} \sum_{n=0}^{M_1-1} r(n,m) \\ &= \frac{1}{M_1} \sum_{\substack{k_1=0 \\ k_2=0}}^{M-1} E\left[\left(X^{(k_1)}(p_1M_1)\right)^* X^{(k_2)}(p_2M_1)\right] \\ &\qquad \times \sum_{p\in\mathbb{Z}} \left(g_P^{(k_1)}(m+p)\right)^* g_P^{(k_2)}(p). \end{aligned} \tag{3.38}$$

Consequently, the mean PSD is

$$\overline{P_x(f)} = \frac{1}{T}\overline{R(f)}|G_I(f)|^2, \tag{3.39}$$

where $\overline{R(f)}$ is the discrete Fourier transform of (3.38).

Assuming that the prototype pulse DFT has only Q non-zero coefficients, (3.37) can be rewritten as

$$E\left[\left(X^{(a_1+b_1Q)}(\ell_1 M_1)\right)^* X^{(a_2+b_2Q)}(\ell_2 M_1)\right] = \begin{cases} M_a L G(a_1) G^*(a_2), & \text{if } \substack{\ell_1=\ell_2, b_1=b_2, \\ a_1-a_2\in\{-L,0,L\}} \\ 0, & \text{otherwise} \end{cases}. \quad (3.40)$$

Then, the PSD can be written as

$$\overline{P_x(f)} = |G_I(f)|^2 \frac{L}{M_1 T} \sum_{k=0}^{K-1} \sum_{(q_1,q_2)\in S} G(q_1) G^*(q_2) G_P^*(f - f_{k,q_1}) G_P(f - f_{k,q_2}), \quad (3.41)$$

where

$$f_{k,q} = (q + kQ)/(MT), \quad (3.42)$$

$$S = \{(x,y) | x,y \in \{0,\ldots,Q-1\}, x - y \in \{-L, 0, L\}\}, \quad (3.43)$$

and $G_P(f)$ is the periodic sinc function, defined as

$$\mathrm{sinc}_{M_1}(f) = e^{j\pi f(M_1-1)} \frac{\sin(\pi M_1 f)}{\sin(\pi f)}, \quad f \in \mathbb{R}. \quad (3.44)$$

In (3.41), we can split the summation with indexes (q_1, q_2) in the two sums and thus in two resulting terms:

$$\overline{P_x(f)} = P_1(f) + P_2(f). \quad (3.45)$$

For $q_1 = q_2$, we obtain the term

$$P_1(f) = G_I(f) \frac{M_a L}{M_1 T} \sum_{k=0}^{K-1} \sum_{q=0}^{Q-1} |G(q)|^2 |G_P(f - f_{k,q})|^2, \quad (3.46)$$

while for $q_1 \neq q_2$, we obtain the term

$$P_2(f) = G_I(f) \frac{2LM_a}{M_1 T} \sum_{k=0}^{K-1} \sum_{q=0}^{Q-L-1} \mathrm{Re}\left\{G(q) G^*(q+L) G_P(f - f_{k,q}) \times G_P^*(f - f_{k,q+L})\right\}, \quad (3.47)$$

where $G_I(f)$ is the Fourier transform of the analog interpolation filter. The first term, $P_1(f)$, is a sum of sinc functions, each centered in $f_{k,q}$ and weighted

by the prototype pulse DFT coefficients. The main lobe of the sinc function has a bandwidth equal to $1/\left((M+\mu)T\right)$. The second term, $P_2(f)$, is related to the correlation between the signal coefficients $X(i)$ at the input of the inner IDFT, defined in (3.10). In detail, we may reconsider (3.10). In fact, such coefficients can be written as

$$X(i) = A^{(k)}(i-kQ)G(i-kQ), \tag{3.48}$$

$$X(i+L) = A^{(k)}(i+L-kQ)G(i+L-kQ) = A^{(k)}(i-kQ)G(i+L-kQ), \tag{3.49}$$

$$i \in \{kQ, \ldots, (k+1)Q-1\}.$$

The correlation between (3.48) and (3.49) will not be null if $Q > L$. This is due to the fact that the block of coefficients $A^{(k)}(i)$, at the output of the outer DFT, is cyclically extended. Equation 3.47 takes this correlation into account.

3.4.2 PAPR-related aspects

The peak-to-average power ratio (PAPR) is a measure of the transmitted signal $x(t)$, defined as

$$\text{PAPR} = \frac{\max_{t\in\mathbb{R}}\left\{|x(t)|^2\right\}}{E\left[|x(t)|^2\right]}. \tag{3.50}$$

The PAPR indicates how much the signal peak power is higher than the mean power value. A signal with high PAPR exhibits high dynamic range. Consequently, this poses a challenge to the analog components of the front end which may introduce distortions. For example, if the signal exceeds the power amplifier dynamic range, the output signal will be clipped to the supply voltage level. In turn, unintentional out-band interference due to spurious emissions is generated as well as the signal distortion may cause a performance loss in the receiver stage. In OFDM, the high PAPR is a known drawback. It grows with the sub-channels number [15]. Generally, the PAPR cannot be expressed in closed-form.

In OFDM, $|x(t)|$ can be approximately modeled as a Rayleigh process as shown in [38] so that pseudo-closed expressions for the distribution of the PAPR can be derived. In CB-FMT, the problem is more complex, so that we have to resort to a numerical approach to evaluate the PAPR as it will be discussed in Section 3.5.3.

In the literature, several PAPR reduction techniques have been proposed for the OFDM system. These techniques are partitioned in two groups: the signal scrambling techniques and the signal distortion techniques [39]. In signal scrambling techniques, a coding is applied to the sub-carrier signals to reduce

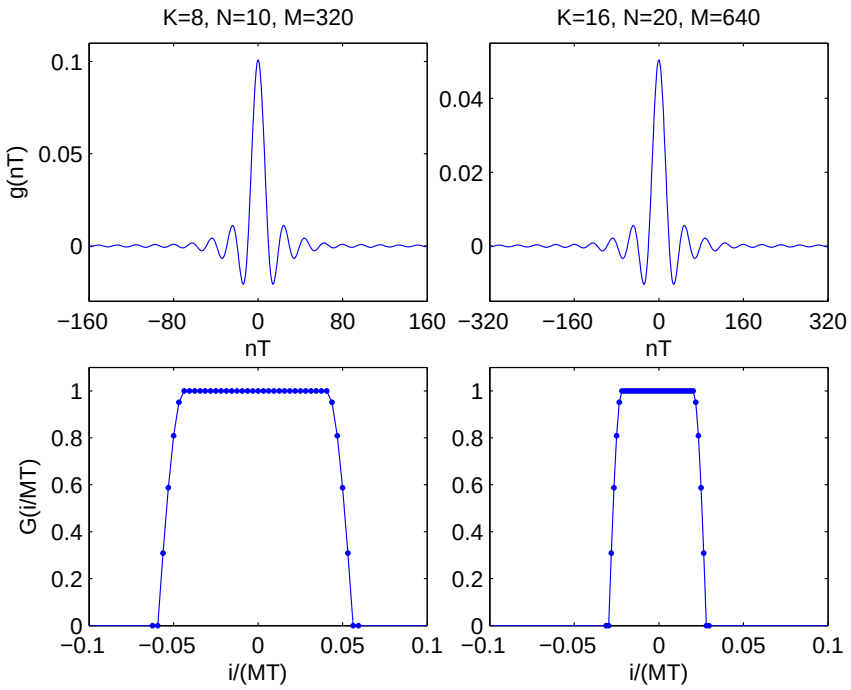

Figure 3.4: Prototype pulse examples for $M = 320$ and $M = 640$ with $T = 1$.

the PAPR. In this case, there is a loss of data rate due to the redundancy introduced by the code. In signal distortion techniques, the shape of the OFDM signal is distorted, i.e., the signal is clipped if it exceeds a threshold. In this case, in-band distortion and out-of-band radiations are introduced. In this work, the PAPR is shown without any reduction techniques to show the worst case. These techniques could be reasonably applied to CB-FMT too.

3.5 Numerical results

3.5.1 Pulse design examples

In Figure 3.4, we report two examples of pulses obtained with the method described in Section 3.3.1. Several combinations of parameters are considered. The pulses have been obtained starting from a root-raised-cosine spectrum with roll-off equal to 0.2. The pulses are designed for $M = 320$ and $M = 640$. Furthermore, $K = 8$ and $N = 10$ or $K = 16$ and $N = 20$ are considered, respectively.

Table 3.1: In-band/out-of-band power ratio for CB-FMT prototype pulse

	M			
	160	**320**	**640**	**1,280**
$K = 4$, $N = 5$	50.10	61.42	69.20	70.91
$K = 8$, $N = 10$	33.44	50.16	61.56	69.86
$K = 16$, $N = 20$	27.40	33.46	50.15	61.23
$K = 32$, $N = 40$	23.90	27.41	33.47	50.14

In Table 3.1, we report the ratio between the in-band and the out-of-band energy of the interpolated prototype pulse for several choices of the parameters. Despite the simple design method, the pulses exhibit good frequency confinement which increases for larger values of M.

In all numerical results that will follow, a common configuration is related to the case $M = 320$ and $K \in \{8, 16, 32, 64\}$.

3.5.2 Complexity comparisons

In Figure 3.5, we show the complexity of OFDM, FMT, and CB-FMT as a function of the prototype pulse length (in samples) and assuming it has Q non-zero DFT coefficients. In all FMT, OFDM, and CB-FMT, the pulse length L_g is set equal to M. It should be noted that OFDM uses a rectangular window of length M equal to the number of sub-channels. The complexity is presented in terms of cop/sample for different combinations of N, K. In CB-FMT, we show the complexity at the receiver side when a 1-tap equalizer is used.

The figure shows that in CB-FMT the complexity grows when the sub-channel number K decreases. This behavior is not intuitive and it requires an explanation. We start from (3.26) for a given M and K/N values. It is easy to show that the complexity is proportional to $(K/N)\log_2 L$. When K grows, N grows too to have constant K/N ratio. To keep $M = LN$ constant, L decreases and, subsequently, the complexity. The figure shows that CB-FMT has significant lower complexity than conventional FMT. Clearly, OFDM is the simplest solution. However, CB-FMT and OFDM have a more comparable complexity, i.e., CB-FMT is more complex than OFDM by a factor of about 1.5. As it will be shown in the next sections, this extra complexity pays back since CB-FMT can offer better PSD confinement, lower PAPR, and better performance in fading channels.

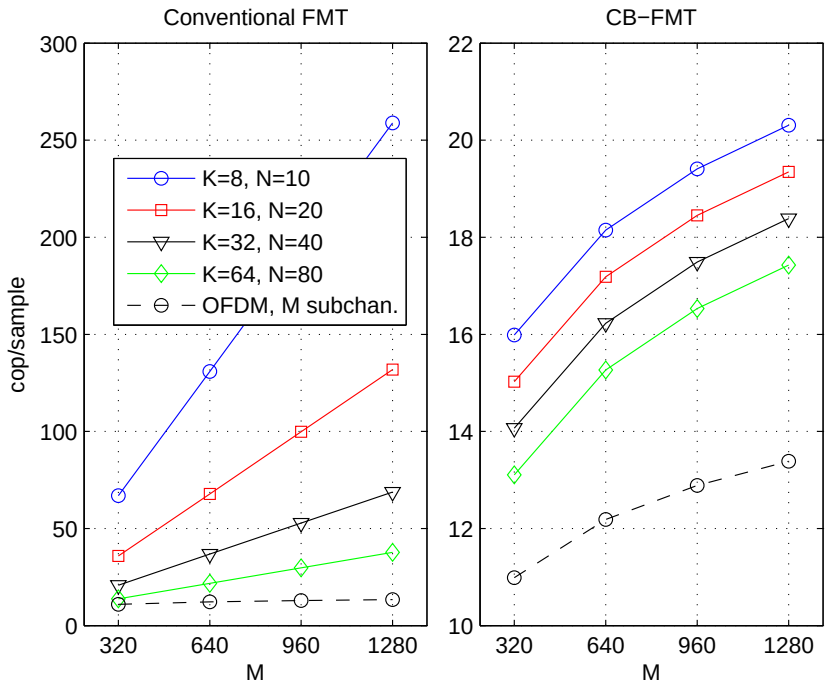

Figure 3.5: Complexity of CB-FMT, FMT, and OFDM in terms of cop/sample as a function of the parameters.

3.5.3 Power spectral density and PAPR

In this section, we consider the PSD and the PAPR of CB-FMT. For the OFDM system, the PSD derivation is reported in [40]. In Figure 3.6, we report an example of PSD of CB-FMT assuming the parameters equal to $K = 8, N = 10, Q = 40, L = 32$ (therefore $M = 320$), $\beta = 0.2$ and the cyclic prefix equal to $\mu = 8$ samples. The interpolation filter is a RRC pulse with roll-off equal to 0.1. If the interpolation pulse were ideal, i.e., the filter was a perfect low-pass filter, the out-band emissions would be null. However, a real interpolation filter introduces out-band emissions. For the parameters specified, the ratio between the useful signal power and out-band emissions power is equal to 25.48 dB. In OFDM, assuming the number of sub-channels equal to $K = 320$, this ratio is equal to 22.80 dB. CB-FMT has slightly better in-band/out-band power ratio due to a higher sub-channel frequency selectivity w.r.t OFDM, under comparable complexity assumption. If we set the number of sub-channels in OFDM equal to $K = 8$, then its in-band/out-of-band power ratio will decrease even further to 20.1 dB.

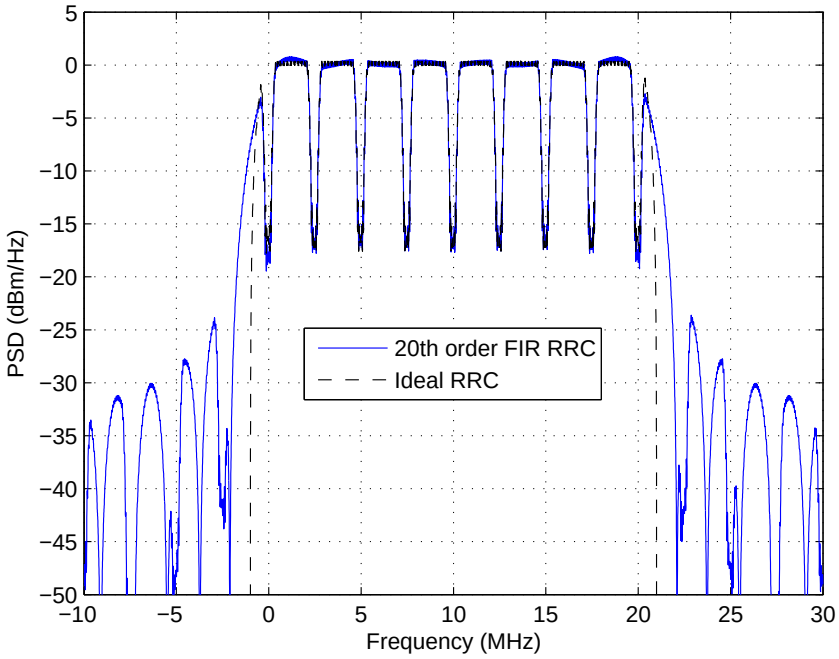

Figure 3.6: Mean power spectral density example of CB-FMT with an ideal and a real interpolation filter. The interpolator filter is a a 20th order root raised-cosine pulse.

We now consider the PAPR. The complementary cumulative distribution function (CCDF) of the PAPR for CB-FMT and OFDM is shown in Figure 3.7. The PAPR is influenced by the inner IDFT block size. In Figure 3.7a, we perform a comparison under similar complexities, i.e., the number of sub-channels in OFDM is set equal to $K = 320$, and in CB-FMT, we set $M = 320$ and $K \in \{4, 8, 16, 32\}$. In CB-FMT, the PAPR is significantly lower than in OFDM for low values of K, N. In Figure 3.7b, we perform a comparison under an equal number of sub-channels. In CB-FMT, we keep the IDFT block size equal to $M = 320$. In this case, OFDM outperforms CB-FMT due to the smaller inner IDFT size. In the simulations, a 4-PSK constellation is used for both systems. As it is shown in the next section, CB-FMT can offer higher spectral efficiency than OFDM with a smaller number of sub-channels. In turn, this allows to obtain a lower PAPR.

In Table 3.2, the mean PAPR for CB-FMT is shown when $M = 320$ and for several combinations of parameters. In OFDM, the mean PAPR is equal to

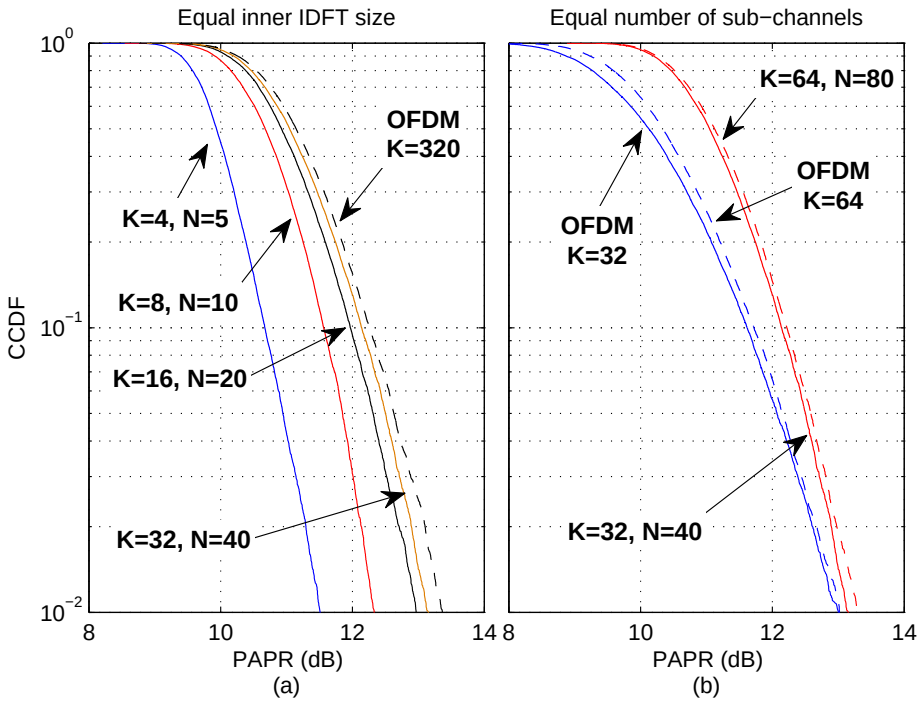

Figure 3.7: The PAPR complementary cumulative distribution function (CCDF) for CB-FMT and OFDM. The CB-FMT and OFDM transmitted signals are interpolated with a 20th order root raised-cosine filter.

11.28 dB, i.e., higher than in CB-FMT for all parameter combinations herein considered.

Table 3.2: Mean PAPR in CB-FMT for different values of K and N

K	N	Mean PAPR [dB]
4	5	10.03
8	10	10.76
16	20	11.06
32	40	11.19

Chapter 4

Orthogonal Design

4.1 Introduction

In this chapter, the orthogonal prototype pulse design problem is analyzed. In CB-FMT, the cyclic convolution allows to simplify the design process w.r.t. conventional FMT. Sure enough, cyclic convolution allows to translate the orthogonality problem in matrix form. A mathematical analysis is performed to determine the orthogonality criterion in time domain and in frequency domain. Starting from the frequency domain, the matrix model is built and the matrix structure is analyzed to have orthogonal pulses. In the first part of this work, the design is performed under ideal conditions, i.e. when the transmitted signal is equal to the received signal. Then, we consider the orthogonality problem when the transmitted signal is filtered with an equivalent filter. Next, we design two types of prototype pulses that maximize two cost functions. First, we design a pulse that maximize the in-band-to-out-band energy ratio. The goal is to obtain high confinement pulses. Second, we design a pulse that maximizes the achievable rate in time-varying scenarios. The goal is to obtain a pulse that improves the robustness to the time-variant channels, e.g. in the high mobility wireless applications. The optimal designed pulses are compared with baseline solutions, i.e. the root-raised-cosine pulse.

This chapter is organized as follows. In Section 4.2, we derive the conditions to have perfect reconstruction in time domain and frequency domain. Then, the orthogonality conditions in frequency domain are derived exploiting the matrix representation. In Section 4.3, we introduce a parametrization of the matrix elements in terms of non-linear combination of trigonometric functions. In Section 4.4, we build and study the non-linear system that solves the orthogonality problem. In Section 4.5, we consider the orthogonality problem

when an equivalent filter is present between the transmitter and the receiver. In Section 4.6, we introduce the two metrics to design the optimal orthogonal pulses under real conditions. In Section 4.7, some design examples are provided and the improvement w.r.t. the baseline solutions is shown.

4.2 Orthogonality Conditions

In CB-FMT, the prototype pulse is designed to have orthogonality between different sub-channels and between different symbols contained in the same sub-channel blocks. To have absence of ICI and ISI, the PR criterion must be found. First, the relation between the output and the input is deduced under ideal transmission medium and perfect synchronization assumptions, i.e. $y(n) = x(n)$. We replace (3.1) in (3.2). After some algebraic manipulation, we obtain

$$\tilde{z}^{(h)}(mN) = \sum_{k=0}^{K-1} \sum_{\ell=0}^{L-1} \tilde{a}^{(k)}(\ell N) g^{(k)} \otimes h^{(h)}(mN - \ell N), \tag{4.1}$$

where

$$\tilde{a}^{(k)}(\ell N) = a^{(k)}(\ell N) W_K^{-\ell N k}, \tag{4.2}$$

$$\tilde{z}^{(h)}(mN) = z^{(h)}(mN) W_K^{mNh}, \tag{4.3}$$

$$g^{(k)}(n) = g\left((n)_M\right) W_K^{-nk}, \tag{4.4}$$

$$h^{(h)}(n) = h\left((n)_M\right) W_K^{-nh}. \tag{4.5}$$

Equations (4.2)–(4.3) represent a rotation in the symbol constellation, equations (4.4)–(4.5) represents a translation of the prototype pulse in frequency domain. In (4.1), the cyclic convolution between $g^{(k)}(n)$ and $h^{(h)}(n)$ represents the cyclic cross-correlation between $g^{(k)}(n)$ and $\left(h^{(h)}(n)\right)^*$, sampled by a factor N. Relation (4.1) can be rewritten as

$$\tilde{z}^{(h)}(mN) = \sum_{k=0}^{K-1} \sum_{\ell=0}^{L-1} \tilde{a}^{(k)}(\ell N) r^{(k,h)}(mN - \ell N), \tag{4.6}$$

$$r^{(k,h)}(mN) = g^{(k)} \otimes h^{(h)}(mN). \tag{4.7}$$

Theorem 1 (Time domain PR conditions)**.** *CB-FMT has PR if and only if the following two conditions are satisfied:*

1. *for $k = h$, the auto-correlation function must be a Kronecker delta, i.e. $r^{(h,h)}(mN) = \delta_m$. Thus, for each sub-channel there is no interference between different symbols in the same block (no ISI condition);*

2. *for $k \neq h$, the cross-correlation must be always null. Thus, there is no interference between different sub-channels (no ICI condition).*

Proof. Equation (4.6) can be rearranged as

$$\begin{aligned}\tilde{z}^{(h)}(mN) =& \tilde{a}^{(k)}(0) r^{(h,h)}(0) \\ &+ \sum_{\substack{\ell=0 \\ \ell \neq m}}^{L-1} \tilde{a}^{(k)}(\ell N) r^{(h,h)}(mN - \ell N) \\ &+ \sum_{\substack{k=0 \\ k \neq h}}^{K-1} \sum_{\ell=0}^{L-1} \tilde{a}^{(k)}(\ell N) r^{(k,h)}(mN - \ell N). \end{aligned} \tag{4.8}$$

From (4.8), it is immediate to see that $r^{(k,h)}(m) = \delta_m \delta_{kh}$ is a valid solution.

This proves the sufficiency. To prove the necessity, we start again from (4.6). We isolate two symbols from the summation, the useful symbol $a^{(h)}(mN)$ and a generic symbol $a^{(k_1)}(\ell_1 N)$ for $k_1 \neq h \wedge \ell_1 \neq m$. Then, (4.6) can be rewritten as

$$\begin{aligned}\tilde{z}^{(h)}(mN) = & a^{(h)}(mN) r^{(h,h)}(0) \\ &+ a^{(k_1)}(\ell_1 N) A_1 + B_1, \end{aligned} \tag{4.9}$$

where $A_1 = r^{(k_1,h)}(mN - \ell_1 N)$ and B_1 is the (4.6) summation without the $k = h \wedge \ell = m$ and $k = k_1 \wedge \ell = \ell_1$ terms.

Now, we consider two symbols sequences, $a_1^{(k)}(\ell N)$ and $a_2^{(k)}(\ell N)$, that differ only in one symbol. We have

$$a_1^{(k)}(\ell N) - a_2^{(k)}(\ell N) = \begin{cases} C_1 & \text{for } k = k_1 \wedge \ell = \ell_1 \\ 0 & \text{otherwise} \end{cases}. \tag{4.10}$$

We consider (4.9). To have PR, we need to satisfy these two equations:

$$\begin{cases} a_1^{(k_1)}(\ell_1 N) A_1 + B_1 = 0 \\ a_2^{(k_1)}(\ell_1 N) A_1 + B_1 = 0 \end{cases}. \tag{4.11}$$

Combining these two equations, we obtain

$$\left(a_1^{(k_1)} - a_2^{(k_1)} \right) A_1 = 0 \tag{4.12}$$

In (4.12), $C_1 = \left(a_1^{(k_1)} - a_2^{(k_1)} \right) \neq 0$. Thus, the equation is satisfied only for $A_1 = 0$. The only possible solution is the Kronecker delta function. □

The above two conditions concern the prototype pulse impulse response. In the following, the prototype pulse is designed in the frequency domain. This allows to simplify the design procedure, as shown in the next sections. To obtain the PR conditions in the frequency domain, we compute the DFT of the cross-correlation. After some algebraic manipulation, we obtain

$$R^{(k,h)}(p) = \frac{1}{N}\sum_{s=0}^{N-1} G(p+sL+kQ)H(p+sL+hQ), \tag{4.13}$$

where $G(p)$ and $H(p)$ are the M-point DFT of the transmitter and receiver prototype pulses and $Q = M/K$ is a positive integer number, respectively.

Theorem 2 (Frequency domain PR conditions)**.** *PR conditions, in the frequency domain, can be written as*

1. *for $k = h$, the product between the prototypes pulse DFT must be a constant. Analytically, we have*

$$\frac{1}{N}\sum_{s=0}^{N-1} G(p+sL+kQ)H(p+sL+kQ) = 1, \tag{4.14}$$
$$\forall p \in \{0,\ldots,L-1\}, \quad \forall k \in \{0,\ldots,K-1\}.$$

2. *For $k \neq h$, the cross-correlation must be always null. Analytically, we have*

$$\frac{1}{N}\sum_{s=0}^{N-1} G(p+sL+kQ)H(p+sL+hQ) = 0, \tag{4.15}$$
$$\forall p \in \{0,\ldots,L-1\}, \quad \forall k \in \{0,\ldots,K-1\}.$$

Proof. The proof is immediate: the frequency domain PR conditions are obtained simply with a translation from the time domain to the frequency domain. □

In the presence of background noise, the SNR is maximized when transmitter and receiver filters are matched [37], i.e. $h(n) = g_{-}^{*}(n) = g^{*}(-n)$. The matched filter condition joined with the PR conditions in Thm. 1 and 2 give the orthogonality conditions.

Corollary 2.1 (Frequency domain orthogonal conditions)**.** *In the frequency domain, the orthogonality conditions are given by:*

1. *for $k = h$, the auto-correlation of the prototype pulse $g(n)$ has flat DFT spectrum. Analytically, we have*

$$\frac{1}{N}\sum_{s=0}^{N-1}|G(p+sL+kQ)|^2 = 1, \tag{4.16}$$
$$\forall p \in \{0,\ldots,L-1\}, \quad \forall k \in \{0,\ldots,K-1\}.$$

2. *For $k \neq h$, the auto-correlation must be always null. Analytically, we have*

$$\frac{1}{N}\sum_{s=0}^{N-1}G(p+sL+kQ)G^*(p+sL+hQ) = 0, \tag{4.17}$$
$$\forall p \in \{0,\ldots,L-1\}, \quad \forall k,h \in \{0,\ldots,K-1\}.$$

Corollary 2.2. *The condition* (4.17) *has the following property*

$$R^{(k,h)}(p) = R^{(0,h-k)}(p), \tag{4.18}$$

due to the periodic property of the DFT. Thus, equation (4.17) *can be rewritten as*

$$\frac{1}{N}\sum_{s=0}^{N-1}G(p+sL)G^*(p+sL+kQ) = 0, \tag{4.19}$$
$$\forall p \in \{0,\ldots,L-1\}, \quad \forall k \in \{0,\ldots,K-1\}.$$

4.2.1 Matrix Representation

The orthogonality conditions in (4.16) and (4.19) can be rewritten in matrix form.

In what follows, we denote the i-th element of a vector $\mathbf{v}$ as $\{\mathbf{v}\}_i$. Furthermore, given a matrix $\mathbf{A}$, we denote the element at the i-th row and j-th column as $\{\mathbf{A}\}_{i,j}$. Finally, to denote the j-th column vector of a matrix $\mathbf{A}$, we use the notation $\{\mathbf{A}\}_{*,j}$.

The M-points DFT coefficients of the prototype pulse can be partitioned in L vectors of size $N \times 1$. Each vector is defined as

$$\{\mathbf{v}_p\}_i = G(p+iL), \tag{4.20}$$
$$p \in \{0,\ldots,L-1\} \quad i \in \{0,\ldots,N-1\}.$$

We define the vector operator $\tau^a \{\mathbf{v}_p\}$ that performs a cyclic shift on the elements. Analytically, the operator can be written as

$$\{\tau^a \{\mathbf{v}_p\}\}_i = G(p + (i+a)_N L), \quad a \in \{0, \dots, N-1\}, \tag{4.21}$$

where the $(\cdot)_X$ operator denotes the modulo operations, i.e. $(c+dX)_X = (c)_X$.

The orthogonality condition in (4.19) can be viewed as an inner product between two vectors $\mathbf{a}$ and $\mathbf{b}$

$$\mathbf{a} \cdot \mathbf{b} = 0, \tag{4.22}$$

where the two vectors are defined as

$$\mathbf{a} = [G(p), G(p+L), \dots]^T, \tag{4.23}$$

$$\mathbf{b} = [G(p+kQ), G(p+L+kQ), \dots]^T. \tag{4.24}$$

Equation (4.22) imposes that the two vectors must be orthogonal. Vectors (4.23) and (4.24) can be rewritten with the notation in (4.20). For the vector in (4.23), it is immediate to see that $\mathbf{a} = \mathbf{v}_p$. For the vector (4.24), we need to find $c_{(p,k)}$ and $d_{(p,k)}$ s.t. $c_{(p,k)} + d_{(p,k)}L = p + kQ$. The solution is easily written as

$$c_{(p,k)} = (p + kQ)_L, \tag{4.25}$$

$$d_{(p,k)} = \frac{p + kQ - c_{(p,k)}}{L} = \frac{p + kQ - (p+kQ)_L}{L}. \tag{4.26}$$

Thus, the vector (4.24) is rewritten as $\mathbf{b} = \tau^{d_{(p,k)}} \left\{ \mathbf{v}_{c_{(p,k)}} \right\}$.

Finally, for a given p value, equation (4.19) involves K vectors:

$$\mathbf{v}_p,\ \tau^{d_{(p,1)}} \left\{ \mathbf{v}_{c_{(p,1)}} \right\},\ \dots,\ \tau^{d_{(p,K-1)}} \left\{ \mathbf{v}_{c_{(p,K-1)}} \right\}. \tag{4.27}$$

These vectors are gathered in a matrix defined as

$$\mathbf{H}_{ort,p} = \frac{1}{\sqrt{N}} \hat{\mathbf{H}}_p, \tag{4.28}$$

$$\left\{ \hat{\mathbf{H}}_p \right\}_{*,j}, = \tau^{d_{(p,j)}} \left\{ \mathbf{v}_{c_{(p,j)}} \right\}, \tag{4.29}$$

$$p \in \{0, \dots, L-1\}, \quad j \in \{0, \dots, K-1\}.$$

4.2.2 Matrix Conditions

Theorem 3. *The orthogonality in* (4.16) *and* (4.17) *is satisfied if and only if the matrices in* (4.28) *have orthogonal columns and with unit norm. If these conditions are satisfied for* $p \in \{0, \ldots, (Q)_L - 1\}$*, the condition is automatically satisfied for other matrices with* $p \in \{(Q)_L, \ldots, L-1\}$*.*

Proof. Given a generic (4.29) matrix for a given p value, if all the columns are orthonormal, the inner product (4.22) is zero for every k values. Thus, (4.17) is satisfied.

We focus on (4.16). This equation can be seen as the Euclidean norm square of the vector $\tau^{d_{(p,k)}} \left\{ \mathbf{v}_{c_{(p,k)}} \right\}$. If all the columns are orthonormal, the norms are equal to unity. Thus, the columns norm of the matrix (4.28) is equal to N, witch satisfies (4.16) condition.

Now, first, we observe that:

$$\begin{aligned} c_{(p+(k_2Q)_L,k)} &= (p + (k_2)_L(Q)_L + (k)_L(Q)_L)_L \\ &= (p + (k + k_2)_L(Q)_L)_L \\ &= c_{(p,k+k_2)}, \end{aligned} \tag{4.30}$$

$$\begin{aligned} d_{(p+(k_2Q)_L,k)} &= \frac{p + kQ + (k_2Q)_L - (p + (k + k_2)\, Q)_L}{L} \\ &= d_{(p,k+k_2)} + \frac{(k_2Q)_L}{L}. \end{aligned} \tag{4.31}$$

Next, we focus on the matrices $\mathbf{H}_{ort,p}$ and $\mathbf{H}_{ort,p+(k_2Q)_L}$. Applying (4.30) and (4.31), we can deduce:

- the two matrices are composed of the same column vectors. The k-th column vector in $\mathbf{H}_{ort,p}$ is translated in the k_2-th column in matrix $\mathbf{H}_{ort,p+(k_2Q)_L}$ (deduced from (4.30));
- all the column vectors of matrix $\mathbf{H}_{ort,p}$ are cyclically shifted by a factor $(k_2Q)_L$ in matrix $\mathbf{H}_{ort,p+(k_2Q)_L}$ (deduced from (4.31)).

Thus, the matrices $\mathbf{H}_{ort,p+(k_2Q)_L}, k_2 \neq 0$ are redundant because they are obtained by a swap on rows and columns of matrix $\mathbf{H}_{ort,p}$. The orthogonality conditions are set only for $p \in \{0, \ldots, (Q)_L - 1\}$. □

Corollary 3.1 (Critically sampled case)**.** *When the system is critically sampled, i.e.* $K = N$ *and* $Q = L$*, the matrices* $\mathbf{H}_{ort,p}$ *are circulant matrices. In this case, the matrices are orthogonal if the vectors* (4.20) *have unit modulus* N*-points DFT, i.e.* $\left|\{\mathbf{F}_N \mathbf{v}_p\}_i\right| = 1$*, where* $\mathbf{F}_N$ *is the* $N \times N$ *DFT matrix.*

Proof. When the system is critically sampled, $Q = L$. In this case, (4.25) and (4.26) can be rewritten as

$$c_{(p,k)} = (p + kL)_L = p, \tag{4.32}$$

$$d_{(p,k)} = \frac{p + kL - (p + kL)_L}{L} = k. \tag{4.33}$$

Equation (4.32) shows that all the columns of $\mathbf{H}_{ort,p}$ are composed of the $\mathbf{v}_p$ vector. Equation (4.33) shows that the k-th column is cyclically shifted by a factor k. Thus, the matrix is circulant.

A property of an orthogonal matrix is that all its eigenvalues, denoted as λ_n, are equal, in modulus, to 1 [41]. Furthermore, the n-th eigenvalue of a circulant matrix is obtained as [42]

$$\lambda_n = \sum_{k=0}^{N-1} \{\mathbf{v}_p\}_k \, e^{-i2\pi nk/N}. \tag{4.34}$$

Equation (4.34) can be identified as N-points DFT. Thus, the eigenvalue vector $\Lambda = [\lambda_0, \ldots, \lambda_{N-1}]$ is given by

$$\Lambda = \mathbf{F}_N \mathbf{v}_p. \tag{4.35}$$

□

4.3 Parametrization with Angles

To design the prototype pulse, the column vectors of $\hat{\mathbf{H}}_p$ must have unit Euclidean norm, i.e. $||\mathbf{v}_p|| = 1$. In other words, the sum of squares of the vector components must be constant and equal to one. This consideration suggests to express the vector components in terms of non-linear combination of trigonometric functions.

First, we focus on real valued solutions, i.e. $\mathbf{v}_p \in \mathbb{R}^N$. For $N = 2$, the norm square is simply given by $x^2 + y^2 = 1$. A solution is given by $x = \cos\alpha, y = \sin\alpha$. This representation exploits the polar coordinates with unit radius. For $N = 3$, the square norm $x^2 + y^2 + z^2 = 1$ represents a sphere in $\mathbb{R}^3$ with unit radius. Exploiting the spherical coordinates allows to write the solution as $x = \cos\alpha, y = \sin\alpha\cos\beta, z = \sin\alpha\cos\beta$. In general, for $\mathbb{R}^N, N > 3$, the

hyper-spherical coordinates [43] can be used. The vector $\mathbf{v}_p$ can be written as

$$\{\mathbf{v}_p\}_0 = \cos\left(\{\boldsymbol{\theta}_p\}_0\right), \tag{4.36}$$

$$\{\mathbf{v}_p\}_1 = \sin\left(\{\boldsymbol{\theta}_p\}_0\right)\cos\left(\{\boldsymbol{\theta}_p\}_1\right), \tag{4.37}$$

$$\vdots \quad = \quad \vdots$$

$$\underset{i\in\{2,\ldots,N-2\}}{\{\mathbf{v}_p\}_i} = \left[\prod_{s=0}^{i-1}\sin\left(\{\boldsymbol{\theta}_p\}_s\right)\right]\cos\left(\{\boldsymbol{\theta}_p\}_i\right), \tag{4.38}$$

$$\vdots \quad = \quad \vdots$$

$$\{\mathbf{v}_p\}_{N-1} = \left[\prod_{s=0}^{N-2}\sin\left(\{\boldsymbol{\theta}_p\}_s\right)\right], \tag{4.39}$$

where $\boldsymbol{\theta}_p$ is the angles vector that represent the vector $\mathbf{v}_p$. It should be noted that the $N \times 1$ vector $\mathbf{v}_p$ is obtained from a set of $N-1$ angles. Thus, the unknowns number going from LN to $L(N-1)$.

In general, the vectors $\mathbf{v}_p$ should be complex. Thus, the angles representation in equations (4.36) to (4.39) can be easily generalized to the complex space. In detail, a phase factor is included for every vector components. The complex angles representation is given by

$$\{\mathbf{v}_p\}_0 = \cos\left(\{\boldsymbol{\theta}_p\}_0\right)e^{i\{\boldsymbol{\Phi}_p\}_0}, \tag{4.40}$$

$$\{\mathbf{v}_p\}_1 = \sin\left(\{\boldsymbol{\theta}_p\}_0\right)\cos\left(\{\boldsymbol{\theta}_p\}_1\right)e^{i\{\boldsymbol{\Phi}_p\}_1}, \tag{4.41}$$

$$\vdots \quad = \quad \vdots$$

$$\underset{i\in\{2,\ldots,N-2\}}{\{\mathbf{v}_p\}_i} = \left[\prod_{s=0}^{i-1}\sin\left(\{\boldsymbol{\theta}_p\}_s\right)\right]\cos\left(\{\boldsymbol{\theta}_p\}_i\right)e^{i\{\boldsymbol{\Phi}_p\}_i}, \tag{4.42}$$

$$\vdots \quad = \quad \vdots$$

$$\{\mathbf{v}_p\}_{N-1} = \left[\prod_{s=0}^{N-2}\sin\left(\{\boldsymbol{\theta}_p\}_s\right)\right]e^{i\{\boldsymbol{\Phi}_p\}_{N-1}}, \tag{4.43}$$

where $\boldsymbol{\Phi}_p$ represents the phases vector. Thus, given $\mathbf{v}_p \in \mathbb{C}^N$, the vector components can be represented with two sets of angles. The first set, $\boldsymbol{\theta}_p$, represents the component modulus; the second set, $\boldsymbol{\Phi}_p$, represents the component phase. The total unknowns number is equal to $L(2N-1)$.

The unknowns number should be reduced if a band limited constraint is set, i.e. $G(i) = 0$ for $Q_2 < i \leq M$. In this case, some components of the vectors $\mathbf{v}_p$ is known and equal to zero. The angles representation is used only for the non-zeros components. To show that, we consider $\mathbf{v}_p$ with only $N_2 < N$

non-zero components. First, we swap the components s.t. the zeros are located at the end of the vector. To set only the last component equal to zero, it is necessary to set $\{\boldsymbol{\theta}_p\}_{N-1} = 0$. Thus, the $(N-2)$ component can be rewritten as

$$\{\mathbf{v}_p\}_{N-2} = \left[\prod_{s=0}^{N-3} \sin\left(\{\boldsymbol{\theta}_p\}_s\right)\right] e^{i\{\boldsymbol{\Phi}_p\}_{N-2}}. \tag{4.44}$$

We should note that (4.44) is similar to (4.43): the $N-1$ coefficients can be represented with $2N-3$ angles, $N-2$ for the modulus and $N-1$ for the phases. This procedure is repeated recursively for each null coefficient. As it finally results, we obtain a set of $2N_2-1$ angles, N_2-1 for the moduli and N_2 for the phases.

4.4 Pulse Design

Exploiting the angles representation described in Sec. 4.3, the condition (4.16) is automatically satisfied. To complete the orthogonal pulse design, we need to set the orthogonality for the matrices $\mathbf{H}_{ort,p}, p \in \{0,\dots,(Q)_L-1\}$, as shown in Thm. 3. To do that, we need to solve the non-linear system

$$\begin{cases} \{\mathbf{H}_{ort,p}\}^H_{*,0} \cdot \{\mathbf{H}_{ort,p}\}_{*,i} = 0 & i \in \{1,\dots,K-1\} \\ \{\mathbf{H}_{ort,p}\}^H_{*,1} \cdot \{\mathbf{H}_{ort,p}\}_{*,i} = 0 & i \in \{2,\dots,K-1\} \\ \quad\vdots & \quad\vdots \\ \{\mathbf{H}_{ort,p}\}^H_{*,K-3} \cdot \{\mathbf{H}_{ort,p}\}_{*,i} = 0 & i \in \{K-2,K-1\} \\ \{\mathbf{H}_{ort,p}\}^H_{*,K-2} \cdot \{\mathbf{H}_{ort,p}\}_{*,K-1} = 0 & \end{cases}. \tag{4.45}$$

From (4.45), we should note that the system is composed of $\sum_{k=0}^{K-1} k = K(K-1)/2$ equations of $(2N-1)/(Q)_L$ unknown angles for complex solutions and $(N-1)/(Q)_L$ for real solutions. The problem is composed of $(Q)_L$ independent systems, thus the total number of equations is equal to $(Q)_L K(K-1)/2$, split in $(Q)_L$ sub-systems.

Theorem 4. *Given a system with parameters K, N, M, there exists an infinite number of prototype pulses that satisfy the Thm. 3 orthogonality conditions.*

Proof. First, we consider the critically sampled case $K = N$. Corollary 3.1 shows that every vector $\mathbf{v}_p$ s.t.

$$\left|\{\mathbf{F}_N \mathbf{v}_p\}_i\right| = 1 \tag{4.46}$$

is a valid solution. Equation (4.46) could be rewritten as

$$\{\mathbf{F}_N \mathbf{v}_p\}_i = e^{j\phi_i}. \tag{4.47}$$

Thus, every set $\{\phi_0, \ldots, \phi_{N-1}\}$ gives a valid solution and, finally, the number of solutions is infinite.

Now, we focus on the general case $K < N$. The matrix columns of $\mathbf{H}_{ort,p}$ are composed of the $L/(Q_L)$ vectors and theirs cyclically shifted version of a factor $Q/(Q)_L$. Indeed, from (4.25) and (4.26), we can see

$$\begin{aligned} c_{(p,k+L/(Q)_L)} &= (p + kQ + LQ/(Q)_L)_L \\ &= (p + kQ + (L)_L(Q)_L/(Q)_L)_L \\ &= c_{(p,k)}, \end{aligned} \tag{4.48}$$

$$\begin{aligned} d_{(p,k+L/(Q)_L)} &= \frac{p + kQ + LQ/(Q)_L - c_{(p,k)}}{L} \\ &= d_{(p,k)} + \frac{Q}{(Q)_L}. \end{aligned} \tag{4.49}$$

Given a $N \times N$ circulant orthogonal matrix, obtained from (4.47), we can obtain a valid $\mathbf{H}_{ort,p}$ matrix simply by dropping $N - K$ columns. Given that there are infinite circulant orthogonal matrices, there are infinite solutions in the case $K < N$ too. □

Corollary 4.1 (Band limited pulses)**.** *If the prototype pulse is band limited, i.e. it has only Q non-zero coefficients ($G(i) = 0$ for $i \in \{Q, \ldots, M-1\}$), the non-linear system* (4.45) *is automatically satisfied. Thus, there are an infinite set of angles that satisfy the* (4.40)–(4.43) *equations. Two cases can be distinguished:*

1. ***Over-sampled case*** *($K < N$). In this case, the $\mathbf{v}_p$ vector has at most $\lceil Q/L \rceil$ non-zero components. Thus, the angles sets $\boldsymbol{\theta}_p$ and $\boldsymbol{\Phi}_p$ have at most $2\lceil Q/L \rceil - 1$ angles.*

2. ***Critically-sampled case*** *($K = N$). In this particular case $Q = L$ and the $\mathbf{v}_p$ vectors has only one non-zero coefficient. Thus, the only valid solutions is written as*

$$\begin{cases} G(p) = e^{i\{\boldsymbol{\Phi}_p\}_0} & \text{for } p \in \{0, \ldots, L-1\} \\ 0 & \text{otherwise} \end{cases}. \tag{4.50}$$

Condition (4.50) *shows that the only possible solution has a rectangular modulus.*

4.5 Practical Aspects and Orthogonality

The orthogonality analysis performed up to now is valid under ideal conditions, i.e. the equivalent filter between the transmitter and the receiver is a Kronecker delta. More generally, the transmitted signal is filtered with an equivalent filter as

$$y(n) = x * g_{\text{eq}}(n), \tag{4.51}$$

where $*$ is the linear convolution operator. The equivalent filter $g_{\text{eq}}(n)$ takes into account some practical aspects, e.g. real interpolation filter or frequency selective channel. In general, the equivalent filter causes an orthogonality loss.

Theorem 5 (Orthogonality with equiv. filter)**.** *In the presence of an equivalent filter between the transmitter and the receiver, orthogonality holds if and only if the filter $g_{eq}(n)$ meets the conditions of Thm. 1 and the receiver pulse in* (4.5) *is equal to* $h^{(h)}(n) = \left(g_{eq,\text{-}} * g_{-}^{(h)}(n)\right)^{*}$.

Proof. Exploiting equation (4.4) allows to rewrite the transmitted signal in (3.1) as

$$x(n) = \sum_{k=0}^{K-1} \sum_{\ell=0}^{L-1} a^{(k)}(\ell N) g^{(k)}(n - \ell N). \tag{4.52}$$

The signal at the receiver input in (4.51) is given by

$$\begin{aligned} y(n) &= \sum_{s=0}^{P-1} g_{\text{eq}}(s) x(n-s) \\ &= \sum_{s=0}^{P-1} g_{\text{eq}}(s) \sum_{k=0}^{K-1} \sum_{\ell=0}^{L-1} a^{(k)}(\ell N) g^{(k)}(n - s - \ell N) \\ &= \sum_{k=0}^{K-1} \sum_{\ell=0}^{L-1} a^{(k)}(\ell N) g_1^{(k)}(n - \ell N), \end{aligned} \tag{4.53}$$

where $g_1^{(k)}(n) = g^{(k)} * g_{\text{eq}}(n)$. Thus, the matched receiver filter for the h-th sub-channel is given by $h^{(h)}(n) = \left(g_{\text{eq,-}} * g_{-}^{(h)}(n)\right)^{*}$.

Condition (4.7) becomes

$$r_{\text{eq}}^{(k,h)}(mN) = r^{(k,h)} * g_{\text{eq}} * g_{\text{eq,-}}^{*}(mN). \tag{4.54}$$

The prototype pulse $g(n)$ is designed to be orthogonal and $r^{(k,h)}(nN)$ is equal to the Kronecker delta. Thus, condition (4.54) simply becomes

$$r_{\text{eq}}^{(k,h)}(mN) = g_{\text{eq}} * g_{\text{eq,-}}^{*}(mN). \tag{4.55}$$

Finally, from (4.55), if the equivalent pulse satisfies Thm. 1, then orthogonality is not lost. □

Generally, the equivalent filter does not satisfy the Nyquist conditions. In this case, an equalizer is required to restore the orthogonality. Two cases can be distinguished, as a function of the equivalent filter type:

1. **Linear Time Invariant filter.** When the equivalent filter is linear time invariant (LTI), a CP allows to simplify the equalizer. In particular, if the CP length, in samples, is greater than or equal to the equivalent filter length (in samples) minus one, the PR is possible with a simple equalizer.

2. **Linear Time Variant filter.** When the equivalent filer in linear time variant (LTV), i.e. for a wireless channel, the equalization process is more complicated, as shown in Chapter 5. Simple solutions have been analyzed in Section 5.5.1. These sub-optimal equalizers do not restore the orthogonality and some interference may be present.

4.6 Practical Pulse Design

As shown in Thm. 4, there are an infinite number of solutions to the orthogonal pulse design problem. To complete the design procedure, we consider the pulse design under an objective function maximization. Two metric functions have been identified:

1. the in-band-to-out-of-band pulse energy;

2. the maximum achievable rate over time-variant wireless channels.

4.6.1 In-band-to-out-of-band metric

To compute the in-band-to-out-of-band ratio, we consider the frequency response of the prototype pulse. The objective function is defined as

$$\begin{aligned} f_1(\boldsymbol{\theta}, \boldsymbol{\Phi}) &= \frac{\int_0^B |S(f, \boldsymbol{\theta}, \boldsymbol{\Phi})|^2 \, \mathrm{d}f}{\int_{-\infty}^{+\infty} |S(f, \boldsymbol{\theta}, \boldsymbol{\Phi})|^2 \, \mathrm{d}f - \int_0^B |S(f, \boldsymbol{\theta}, \boldsymbol{\Phi})|^2 \, \mathrm{d}f}, \\ \boldsymbol{\theta} &= [\boldsymbol{\theta}_0, \ldots, \boldsymbol{\theta}_{L-1}], \\ \boldsymbol{\Phi} &= [\boldsymbol{\Phi}_0, \ldots, \boldsymbol{\Phi}_{L-1}], \end{aligned} \tag{4.56}$$

where $S(f, \boldsymbol{\theta}, \boldsymbol{\Phi})$ is the frequency response of the prototype pulse, $B = 1/KT$ is the sub-channel bandwidth and $\boldsymbol{\theta}$, $\boldsymbol{\Phi}$ are two $(2N-1) \times L$ matrices that contain all the angle parameters of equations (4.40) to (4.43).

4.6.2 Maximum achievable rate metric

To optimize the mean achievable rate, we follow this procedure:

1. we build a series of N_{ch} channel realizations;

2. for each channel realization, we search the prototype pulse that maximizes the metric

$$f_2(\boldsymbol{\theta}, \boldsymbol{\Phi}) = \\ = \frac{1}{(M+\mu)T} \sum_{k=0}^{K-1} \sum_{\ell=0}^{L-1} \log_2 \left((1 + \mathrm{SINR}^{(k)}(\ell, \boldsymbol{\theta}, \boldsymbol{\Phi}) \right), \tag{4.57}$$

   where $\mathrm{SINR}^{(k)}(\ell, \boldsymbol{\theta}, \boldsymbol{\Phi})$ is the signal-to-noise-plus-interference computed for the ℓ-th element of the block transmitted in the k-th channels. The matrices $\boldsymbol{\theta}$ and $\boldsymbol{\Phi}$ are defined as in equation (4.56). Equation (4.57) is the maximum achievable rate computed exploiting the Shannon capacity.

   In this step, we obtain a set of N_{ch} prototype pulses;

3. for each prototype pulse designed in previous step, we compute (4.57) for every N_{ch} channel realizations. In this way, we build a $N_{ch} \times N_{ch}$ matrix: each n-th column is the vector of the N_{ch} achievable rate computed with the n-th prototype pulse;

4. we computed the mean achievable rate for every column and we select the prototype pulse that maximizes the mean achievable rate.

4.7 Numerical Results

To search the optimal pulses that maximize the objective functions (4.56) and (4.57), a numerical approach has been adopted. The optimization problem is a function maximization problem under non-linear constraints. In this case, the constraints are given by the orthogonality conditions (4.16) and (4.17). The design is performed in the frequency domain. The angles representation, described in Sec. 4.3, is adopted. The optimization process is performed exploiting the interior point method [44, 45, 46]. In general, in optimization algorithms, the starting point influences the solution: different starting points could give different solutions due to the local maximum problem. To avoid this, we repeat the optimization several times for randomly and different starting points. Finally, we select the pulse that maximizes the metric.

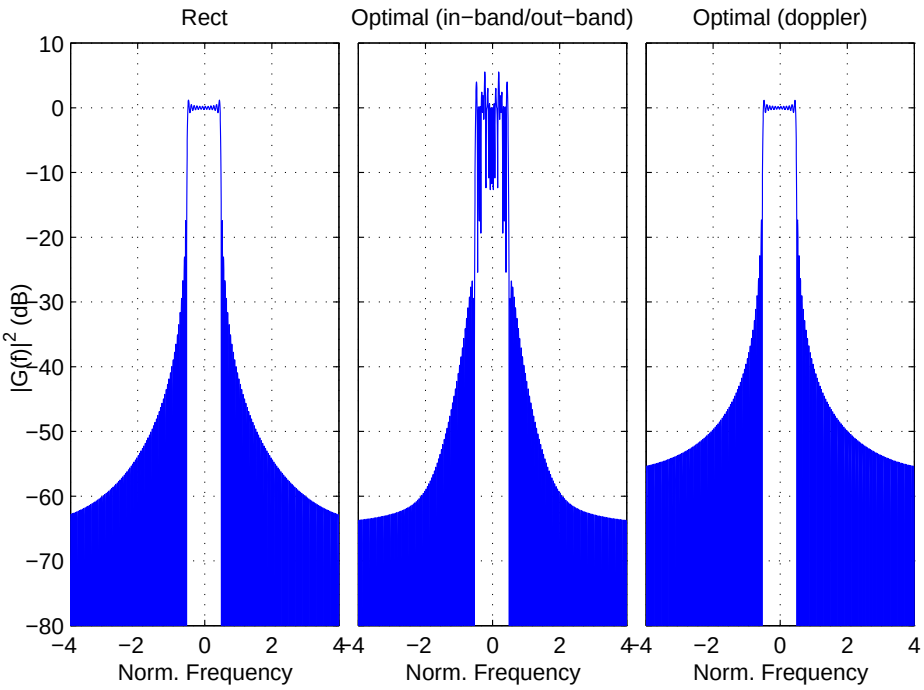

Figure 4.1: Frequency response of the prototype pulse for the critically sampled case ($K = 10, N = 10$). Plot in left shows the frequency response of baseline. Plot in the middle shows the in-band/out-band optimal pulses. Finally, plot right shows the maximum achievable optimal pulses. In these plots, the frequency is normalized to the sub-channel spacing, i.e. $1/KT = 1$.

The design is performed for a given filter length, set to $M = 240$, and different K, N values. In details, we choose $K \in \{8, 10, 12\}$ and appropriate N values s.t. $K/N \in [0.5, 1]$. When $K = N$, the system is critically sampled and exhibits the maximum rate equal to $M/(M + \mu)T$ symbols/s.

For the in-band-to-out-of-band metric, we design two prototype pulses: the symmetric and the asymmetric pulses. The first pulse has Hermitian symmetric DFT coefficients - and, consequentially, real impulse response - and it is obtained with the angles representation in (4.40)-(4.43). The second pulse has no symmetry in frequency domain and impulse response could be complex.

For the achievable rate metric, we design the following two prototype pulses: the real and complex symmetric pulses. The first pulse has real DFT coefficients - and, consequently, Hermitian symmetric impulse response - and it is obtained with the angles representation in (4.36)-(4.39). The second pulse has

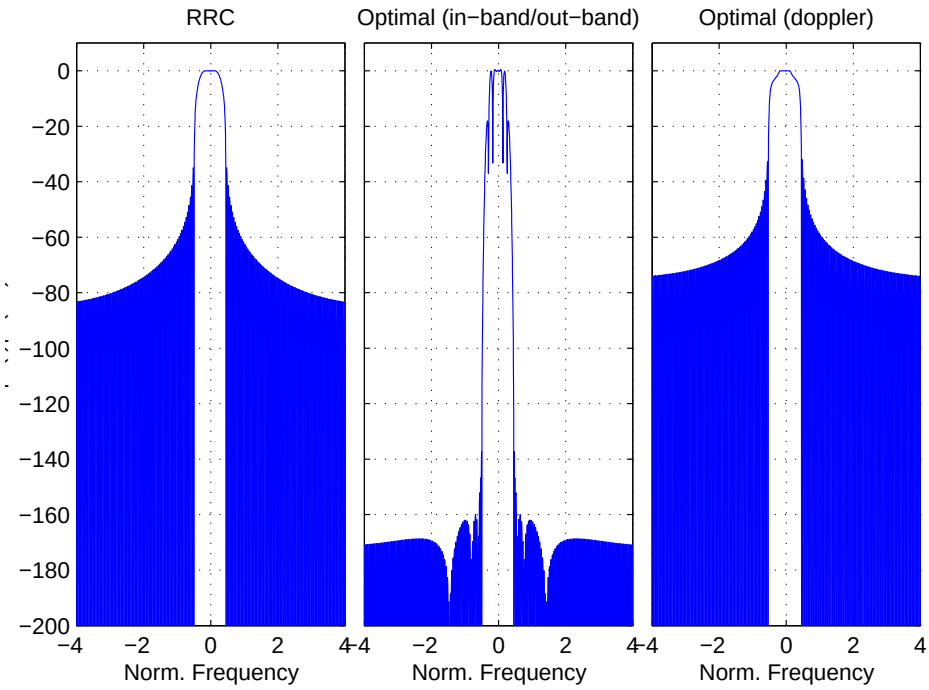

Figure 4.2: Frequency response of the prototype pulse for the critically sampled case ($K = 10, N = 10$). Plot in left shows the frequency response of baseline. Plot in the middle shows the in-band/out-band optimal pulses. Finally, plot right shows the maximum achievable optimal pulses. In these plots, the frequency is normalized to the sub-channel spacing, i.e. $1/KT = 1$.

complex DFT coefficients - and, in general, has no symmetry in time domain - and exploits the angles representation in (4.40)-(4.43). In this metric, we do not distinguish between symmetric and asymmetric pulses because the algorithm converges always to a symmetric solution. Thus, we distinguish between real and complex pulses.

We compare the optimal pulse performance with the RRC baseline pulse. The DFT coefficients are obtained sampling the frequency response in (2.19): $G(i) = \hat{G}(i/MT)$. The roll-off is chosen s.t. there is not interference between adjacent sub-channels. In details, we have $\beta_{max} = (Q - L)/L$ [47]. In the critically sampled case, $\beta_{max} = 0$. Thus, the RRC pulse coincides with the rectangular window in frequency domain.

Table 4.1: In-band to out-band ratios for baseline and optimal pulses.

System Params.			Metric value (dB)				
			RRC	In-band/Out-band		Achievable rate	
K	N	Rate		Symm.	Asym.	Real.	Complex
8	8	1.00	19.71	19.71	23.02	–	19.69
	10	0.80	44.72	146.38	119.61	31.65	30.72
	12	0.67	49.04	154.60	132.79	33.43	31.28
	16	0.50	51.63	148.56	123.80	33.61	34.08
10	10	1.00	17.42	19.36	19.57	–	17.39
	12	0.83	39.64	122.33	89.20	28.72	28.60
	16	0.63	46.90	151.51	123.29	29.60	27.92
	20	0.50	48.72	150.03	125.68	32.74	32.32
12	12	1.00	16.64	18.51	18.71	–	16.59
	16	0.75	40.93	123.51	98.88	26.85	24.83
	20	0.60	44.93	161.58	119.55	30.06	28.34
	24	0.50	46.33	144.96	130.01	31.00	30.20

4.7.1 In-band to out-band ratio

In Fig. 4.1, the critically sampled case ($K = N$) is analyzed. The plot in the middle shows the prototype pulse frequency response when the objective function is the in-band to out-band ratio. The optimal pulse has complex and symmetric DFT coefficients. The plot on the right shows the prototype pulse frequency response when the objective function is achievable rate in wireless time-variant channels, designed as explained in Sec. 4.7.2. In this case, the frequency response exhibits very similar spectrum for both pulses.

In Fig. 4.2, the over-sampled case ($K < N$) is analyzed. The plot in the middle shows the prototype pulse frequency response when the objective function is the in-band to out-band ratio. The interference in the adjacent sub-channel is less than RRC pulse. The plot on the right shows the optimal pulse for achievable rate metric. In this case, the optimal pulses have worst frequency confinement w.r.t. RRC pulse.

In CB-FMT, each sub-channel maps L symbols in Q frequency bins. In over-sampled case ($K < N$), $Q > L$, i.e., a redundancy is introduced. This allows to add some degrees of freedom in the prototype pulse design. Thus, the metric can significantly improved.

Tab. 4.1 shows the in-band to out-band ratio for all the simulated parameters.

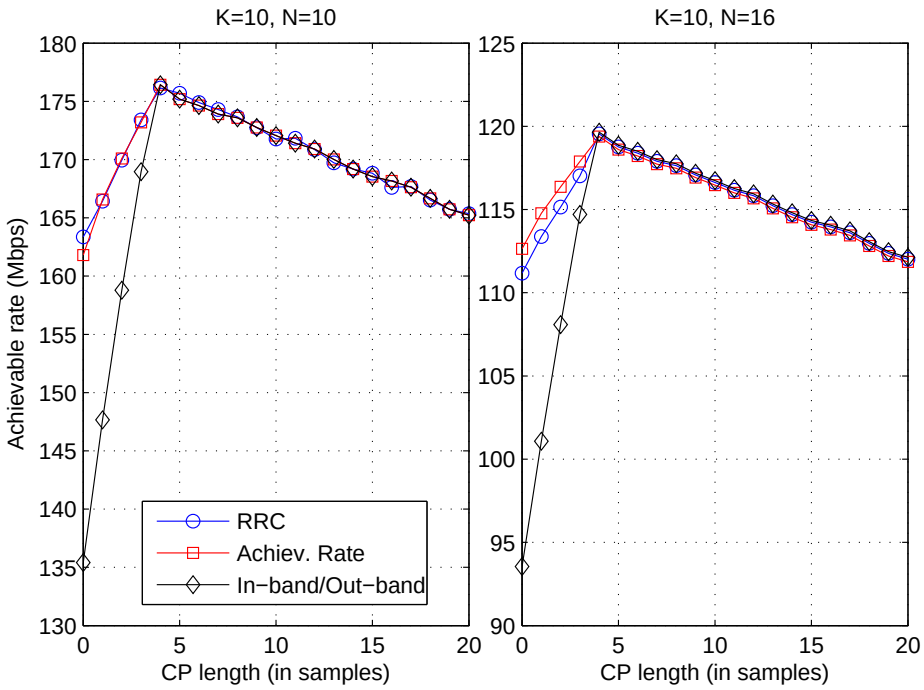

Figure 4.3: Maximum achievable rate as a function of cyclic prefix length prototype pulses. On the left, the critically sampled case in reported for $K = 10, N = 10$. On the right, the over-sampled case is reported for $K = 10, N = 16$.

4.7.2 Maximum achievable rate

To design the prototype pulse that maximizes the achievable rate, we follow the steps reported in Sec. 4.6.2. The wireless channel is modeled with the Clarke's isotropic scattering [48]. The channel is assumed frequency selective with normalized delay spread equal to $\gamma = 2$. To design the prototype pulse, the normalized doppler frequency is set to 5×10^{-5}. To perform a performance analysis, we have studied both the static and time-variant scenarios. In all cases, the SNR is set equal to 30 dB.

For static channels case, we have computed the achievable rate as a function of the CP, as shown in Fig. 4.3. When the CP length is greater than the channel duration, all the considered pulses have the same performance. Achievable rate decreases when the CP length grows due to overhead increase. When the CP is shorter than the channel duration, the inter-block interference (IBI) may be present. In this numerical analysis a single-tap equalizer is used,

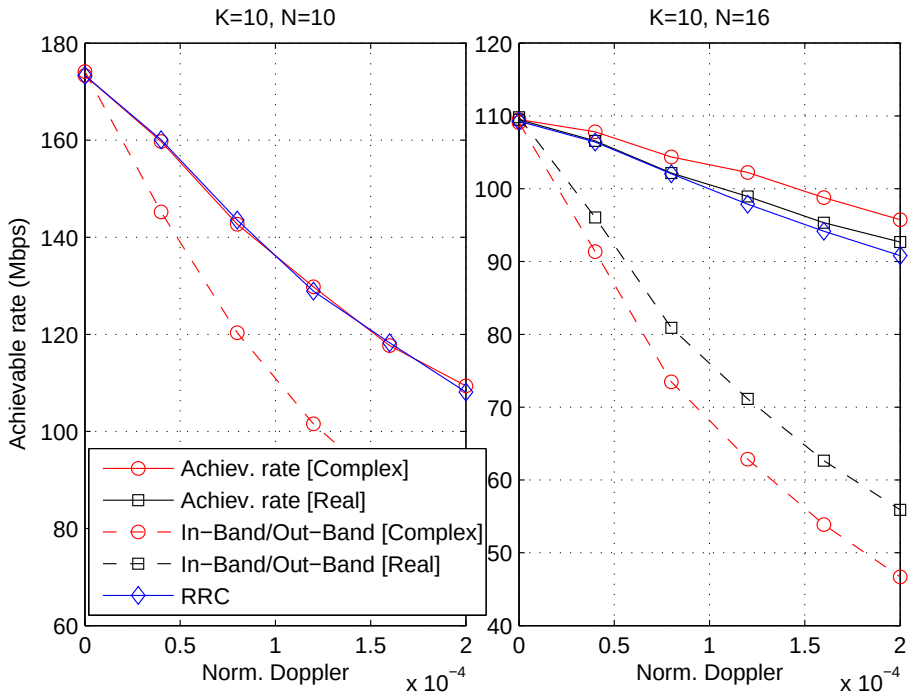

Figure 4.4: Maximum achievable rate as a function of the normalized doppler frequency for different prototype pulses. On the left, the critically sampled case in reported for $K = 10, N = 10$. On the right, the over-sampled case is reported for $K = 10, N = 16$.

as described in Section 5.5.1. The equalizer takes into account the power of the interference signal. Thus, IBI introduces a performance degradation. For the critically sampled case, RRC and optimal achievable rate pulses exhibit equal performance. For over-sampled case, the optimal achievable rate pulse has the better performance w.r.t. the RRC pulse. In both cases, the in-band/out-band optimal pulse introduces an achievable rate drop.

For time-variant channels, the achievable rate is computed as a function of the Doppler frequency, as shown in Fig. 4.4. For the critically sampled case, the achievable rate optimal pulse offers the same performance as the rectangular pulse. For the over-sampled case, the achievable rate complex symmetric optimal pulse has better performance. The real symmetric optimal pulse has similar performance to RRC for low Doppler; for high Doppler the performances are better than RRC. In both cases, critically sampled and over-sampled, the in-band/out-band optimal pulse introduces an important drop of

achievable rate.

In both cases (static with short CP and time-variant), there is an orthogonality loss. The optimization of the maximum achievable rate metric increases the robustness to interference when the orthogonality is lost. Thus, the performances are improved in the static case too. The optimization of the in-band to out-band ratio metric is performed at the transmitter and it does not take into the account the transmission medium. This has two consequences. On the one hand, the in-band to out-band ratio is improved w.r.t. the simple RRC pulse. On the other hand, the pulse robustness to interference is less than the RRC pulse.

Chapter 5

Equalization

5.1 Introduction

In the previous chapters, the CB-FMT system is considered on ideal condition, i.e. when the transmission medium is ideal (or flat frequency response) and there is no noise. Under these assumptions, the system is orthogonal if the orthogonality conditions, described in Ch. 4, are satisfied.

In a real application scenario, the channel frequency response could be frequency selective and/or time variant. Generally, in this case, the orthogonality is lost and some interference could be present. We distinguish three types of interference. The ISI is generated from the other symbols belonging to the sub-channel block: as shown, in CB-FMT each sub-channel processes L symbols at the same time. At the receiver, the n-th symbol in the block is given by the n-th transmitted signal plus a combination of the other $L-1$ symbols (ISI).

ICI is generated from the other sub-channels: at the received symbol is added a combination of the $(K-1)L$ symbols transmitted in the other sub-channels.

Finally, inter-block interference (IBI) is generated only when the channel impulse response has more than one coefficient (time dispersive). As shown, CB-FMT translates KL symbols in a signal of M coefficients that can be viewed as a block. When the transmission is continuous, these M coefficients blocks are adjacent. If the channel is time-dispersive, the blocks interfere with each other.

If the channel is time-invariant and frequency selective, orthogonality between different sub-channels is kept. For every sub-channel, interference between the symbols is introduced. This interference can be split into two com-

ponents: ISI (for symbols belonging to the useful sub-channel block) and IBI (for symbols belonging to the adjacent sub-channel blocks). If the channel is flat and time-variant, orthogonality is lost and ISI and ICI are introduced. Finally, if the channel is time-variant and frequency selective, ISI, ICI and IBI are introduced.

To avoid performance drops due to the interference, the orthogonality should be restored with an equalizer. Exploiting the frequency domain implementation, we design the equalizer in the frequency domain. This allows to simplify the design process w.r.t. the time domain. We propose several equalizers for time-invariant and time-variant channels and we analyze the IBI problem.

This chapter is organized as follows:

- In Sec. 5.2, a matrix channel model is introduced. This model describes the convolution between the transmitted signal and the channel impulse response in matrix form. The transmitted signal is modeled as a vector of M elements. The model takes into account the cyclic prefix and shows the analytic expression of the interference when the CP is shorter than the channel memory.

- In Sec. 5.3, the matrix model is translated in frequency domain to produce a relation between the M-points DFT of the transmitted and received signals. Thus, the MMSE frequency domain equalizer is introduced.

- In Sec. 5.4, we design the equalizer for time-invariant channels. In this case, the channel impulse response is time dispersive and constant. In this case, a 1-tap equalizer is sufficient to restore the orthogonality.

- In Sec. 5.5, we design the equalizer for time-variant channels. In this case, a 1-tap equalizer can not restore the orthogonality and more involved techniques are required. We introduce several equalizers with growing complexity.

5.2 Channel Matrix Model

From the frequency domain implementation of CB-FMT (Figure 3.3), we note that the chain comprising the M-point inner IDFT at the transmitter, the transmission medium, and the M-point inner DFT at the receiver is similar to the OFDM system. This suggests to append a CP of μ samples to the transmitted block of samples, as shown in Figure 5.1.

To proceed, we recall the time-variant channel impulse response, defined in (2.3)

$$h_{\text{ch}}(n) = \sum_{s=0}^{P-1} \alpha_s(n)\delta(n-s), \tag{5.1}$$

where P is the channel impulse response length in samples, and $\alpha_s(n)$ is the s-th channel tap at time instant n. Then, the received signal can be written as

$$y(n) = \sum_{s=0}^{P-1} \alpha_s(n)x(n-s). \tag{5.2}$$

We distinguish between two cases as a function of the CP length. When $\mu \geq P-1$, there is no IBI and the channel matrix assumes a circulant form, as shown in the next Sec. 5.2.1. When $\mu < P-1$ there is interference between the current and the previous transmitted blocks. This case is studied in Sec. 5.2.2.

5.2.1 Long Cyclic Prefix

After CP removal, under the assumption that the channel memory (in samples) is shorter than the CP, (5.2) becomes a circular convolution between the transmitted signal and the channel impulse response. In matrix form, we can write

$$\mathbf{y} = \mathbf{H}_{\text{CH}}\mathbf{x} \tag{5.3}$$

where $\mathbf{y} = [y(\mu)\ y(\mu+1)\ \ldots\ y(M+\mu-1)]^T$, $\mathbf{x} = [x(0)\ x(1)\ \ldots\ x(M-1)]^T$ and $\mathbf{H}_{\text{CH}}$ is the circulant channel matrix of size $M \times M$. The i-th element of the j-th channel matrix column is defined as

$$\{\mathbf{H}_{\text{CH}}\}_{ij} = \begin{cases} \alpha_m(i), & \text{for } m = \text{mod}(i-j, M) \in \{0, \ldots, P-1\}, \\ 0, & \text{otherwise.} \end{cases} \tag{5.4}$$

5.2.2 Short Cyclic Prefix

If the channel memory (in samples) is greater than the CP, or the CP is not present, (5.2) remains a linear convolution between the transmitted signal and the channel impulse response. Thus, there is IBI. In matrix form, we can write

$$\mathbf{y} = \mathbf{H}_{\text{CH}}\mathbf{x} + \mathbf{H}_{\text{I}}\mathbf{x}_{\text{I}}, \tag{5.5}$$

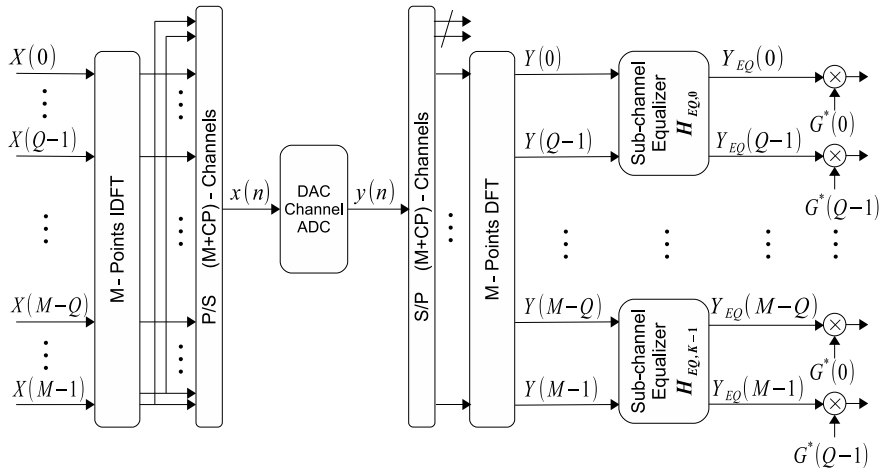

Figure 5.1: Cyclic prefix and frequency domain equalization in CB-FMT.

where $\mathbf{x}_{\mathrm{I}} = [x_I(0)\ x_I(1)\ \ldots\ x_I(M-1)]^T$ is the previous transmitted block. The i-th element of the j-th channel matrix column is defined as

$$\{\mathbf{H}_{\mathrm{CH}}\}_{ij} = \begin{cases} \alpha_m(i), & \text{for } m = \mathrm{mod}(i-j, M) \in \{0, \ldots, P-1\}, \\ & i + \mu - m \geq 0, \\ 0, & \text{otherwise.} \end{cases} \tag{5.6}$$

The interference matrix $\mathbf{H}_{\mathrm{I}}$ is defined as

$$\{\mathbf{H}_{\mathrm{I}}\}_{ij} = \begin{cases} \alpha_m(i), & \text{for } m = \mu + \mathrm{mod}(i-j, M) \in \{\mu+1, \ldots, P-1\}, \\ 0, & \text{otherwise.} \end{cases} \tag{5.7}$$

From (5.5), we note that the interference can be seen as an additive noise. Thus, if the previous block is unknown, the interference introduced by the short CP could be minimized with a MMSE equalizer.

5.3 Frequency Domain Equalization

When the CP is long, the elements of the matrix $\mathbf{H}_{\mathrm{CH}}$ can be easily written in closed form. We work in frequency domain. If we apply an M-point DFT to (5.3), which is what the receiver does through the inner DFT, we will obtain

$$\mathbf{Y} = \mathbf{F}_M \mathbf{H}_{\mathrm{CH}} \mathbf{x} = \mathbf{F}_M \mathbf{H}_{\mathrm{CH}} \mathbf{F}_M^H \mathbf{X} = \hat{\mathbf{H}}_{\mathrm{CH}} \mathbf{X}, \tag{5.8}$$

where $\mathbf{F}_M$ is the M-point DFT matrix, defined as $\{\mathbf{F}_M\}_{ij} = W_M^{ij}/\sqrt{M}$, $i, j \in \{0, \ldots, M-1\}$, and $\mathbf{X}$ is the vector of coefficients at the input of the inner IDFT at the transmitter side. Essentially, (5.8) describes the relation that exists between the coefficients at the input of the inner IDFT at the transmitter side and the coefficients at the output of the inner DFT at the receiver side. Such a relation suggests the use of a frequency domain equalizer applied at the output of the receiver inner DFT as shown in Figure 5.1. To proceed, we need to derive an expression for the elements of the matrix $\hat{\mathbf{H}}_{\text{CH}}$.

We start from (5.2). Without loss of generality, we can extend the sum from P to M by zero-padding the channel impulse response. The block of received samples can be written as

$$\begin{aligned} y(n) &= x * h_{\text{ch}} \\ &= \sum_{s=0}^{M-1} \alpha_s(n) x(n-s) \\ &= \sum_{s=0}^{M-1} \alpha_s(n) \sum_{p=0}^{M-1} X(p) W_M^{-p(n-s)} \\ &= \sum_{p=0}^{M-1} X(p) H_1(p,n) W_M^{-pn}, \qquad (5.9) \\ n &\in \{\mu, \ldots, M+\mu-1\}, \end{aligned}$$

where $H_1(p,n)$ is the M-point DFT of the channel impulse response at time instant n, i.e., computed along the ℓ variable. By computing the M-point DFT of (5.9), we obtain the elements of the vector (5.8):

$$\begin{aligned} Y(q) &= \sum_{n=0}^{M-1} \sum_{p=0}^{M-1} X(p) H_1(p,n) W_M^{-pn} W_M^{qn} \\ &= \sum_{p=0}^{M-1} X(p) H_2(p, q-p), \qquad (5.10) \\ q &\in \{0, \ldots, M-1\}, \end{aligned}$$

where $H_2(p,q)$ is the two-dimensional M-point DFT of $h_{\text{CH}}(\ell, n)$, defined as

$$H_2(p,q) = \sum_{s=0}^{M-1} \sum_{n=0}^{M-1} \alpha_s(n) W_M^{sp+nq}. \qquad (5.11)$$

Finally, it follows that the elements of $\hat{\mathbf{H}}_{\text{CH}}$ are defined as

$$\left\{\hat{\mathbf{H}}_{\text{CH}}\right\}_{ij} = H_2\left(j, \text{mod}(i-j, M)\right). \qquad (5.12)$$

In frequency domain, the equalizer is represented as a matrix $\mathbf{H}_{\mathrm{EQ}}$. The equalized received signal is defined as

$$\mathbf{Y}_{\mathrm{EQ}} = \mathbf{H}_{\mathrm{EQ}}\mathbf{Y}, \tag{5.13}$$

$$\mathbf{Y} = \hat{\mathbf{H}}_{\mathrm{CH}}\mathbf{X} + \mathbf{N}, \tag{5.14}$$

where $\mathbf{N}$ is the M-points DFT of the background noise at the receiver input. The equalizer is designed to minimize the mean square error (MSE) between the transmitted signal and the equalized signal. This equalizer is known as MMSE equalizer [49] and is expressed as

$$\mathbf{H}_{\mathrm{EQ}} = \mathbf{R}_{\mathbf{YY}}{}^{-1}\mathbf{R}_{\mathbf{YX}}, \tag{5.15}$$

$$\mathbf{R}_{\mathbf{YY}} = E\left[\mathbf{Y}\mathbf{Y}^{H}\right], \tag{5.16}$$

$$\mathbf{R}_{\mathbf{YX}} = E\left[\mathbf{Y}\mathbf{X}^{H}\right], \tag{5.17}$$

where $(\cdot)^H$ and $E[\cdot]$ are the Hermitian operator and the expectation operator, respectively. $\mathbf{R}_{\mathbf{YY}}$ and $\mathbf{R}_{\mathbf{YX}}$ are the autocorrelation matrices of the received signal and the cross-correlation between transmitted and received signal, respectively.

To derive the FD equalizer, we distinguish between the case of having a time-invariant channel and the case of having a time-variant channel.

5.4 Time-invariant channel

When the channel is time-invariant, $h_{\mathrm{CH}}(\ell, n)$ does not depend on the time instant n. Thus, $H_2(p, q)$ is non-zero only for $q = 0$. Consequently, the channel matrix $\hat{\mathbf{H}}_{\mathrm{CH}}$ is a diagonal matrix. The M-point DFT output, at the receiver stage, can be simply written as follows:

$$\begin{gathered} Y(p + kQ) = X(p + kQ)H_2(p + kQ, 0) + N(p + kQ), \\ p \in \{0, \ldots, Q-1\}, \quad k \in \{0, \ldots, K-1\}, \end{gathered} \tag{5.18}$$

where $N(i)$, $i \in \{0, \ldots, M-1\}$, are the M-point DFT coefficients of the background noise samples. This shows that there is absence of ICI, i.e., interference among the sub-channels. Therefore, the application of a simple 1-tap frequency domain equalizer is enabled [30]. In particular, with zero forcing, the equalizer output is given by

$$Y_{\mathrm{EQ}}(p + kQ) = Y(p + kQ)H_{\mathrm{EQ,ZF}}(p + kQ), \tag{5.19}$$

$$H_{\mathrm{EQ,ZF}}(p + kQ) = \frac{1}{H_2(p + kQ, 0)},$$

where $H_{\mathrm{EQ,ZF}}(i)$ is the i-th coefficient of the FD zero forcing equalizer. In Figure 5.1, the matrix $\mathbf{H}_{\mathrm{EQ},k}$, associated to the k-th sub-channel equalizer, is diagonal. Its p-th main diagonal element is equal to $H_{\mathrm{EQ,ZF}}(p+kQ)$. In such a case, perfect orthogonality is achieved in the system. That is, after zero forcing equalization, the sub-channel signal is multiplied with the conjugate of the pulse frequency response $G^*(p)$, and it is finally processed by the other stages depicted in Figure 3.3. Then, the output reads as in (3.19).

Alternatively, the equalizer coefficients can be designed according to the MMSE principle and they read

$$H_{\mathrm{EQ,MMSE}}(p+kQ) = \frac{H_2^*(p+kQ)}{|H_2(p+kQ,0)|^2 + \sigma^2/|G(p)|^2}, \tag{5.20}$$

where σ^2 is the noise variance. This solution provides better performance at low signal-to-noise ratios than the zero forcing solution.

Finally, the equalization matrix in (5.13) is a diagonal matrix. The elements are defined as

$$\{\mathbf{H}_{\mathrm{EQ}}\}_{ii} = \frac{H_2^*(i)}{|H_2(i,0)|^2 + \sigma^2/|G\left(\mathrm{mod}\left(i,Q\right)\right)|^2}. \tag{5.21}$$

The 1-tap equalizer is generally used in OFDM for time-invariant channels [50].

5.5 Time-variant channel

When the channel is time variant, the channel matrix $\hat{\mathbf{H}}_{\mathrm{CH}}$ has non-zero elements outside the main diagonal. The number of non-zero elements off the diagonal grows with the channel Doppler spread [51]. The q-th inner DFT output coefficient at the receiver can be written as

$$Y(q) = X(q)H_2(q,0) + \sum_{\substack{p=0 \\ p\neq q}}^{M-1} X(p)H_2(p,q-p) + N(q). \tag{5.22}$$

Relation (5.22) shows that a simple 1-tap equalizer cannot fully remove the interference introduced by the time-variant channel and represented by the second additive term in (5.22). Thus, we propose several equalizers with growing complexity.

5.5.1 1-tap Equalizer

The 1-tap equalizer applies the MMSE criterion independently for each DFT coefficient of the received signal. The MMSE criterion is applied between $Y(q)$ and $X(q)$, i.e., the q-th diagonal element of the $\mathbf{H}_{EQ}$ matrix is equal to

$$\{\mathbf{H}_{\mathrm{EQ}}\}_{ii} = \frac{R_{XY}(i)}{R_{YY}(i)}, \tag{5.23}$$

where $R_{XY}(q)$ and $R_{YY}(q)$ are the scalar version of eq. (5.16) and (5.17), respectively. After some algebraic manipulations, we obtain

$$R_{YY}(q) = R_{YY}^{(1)}(q) + R_{YY}^{(2)}(q), \tag{5.24}$$

$$R_{YY}^{(1)}(q) = L \sum_{p=0}^{M-1} |G_1(p)|^2 |H_2(p, q-p)|^2 + \sigma^2, \tag{5.25}$$

$$R_{YY}^{(2)}(q) = 2L \,\mathrm{Re}\left\{ \sum_{s=0}^{K-1} \sum_{u=0}^{Q-L-1} G(u) G^*(u+L) \times \right.$$
$$\left. \times\, H_2^{(s)}(u, q-u) \left(H_2^{(s)}(u+L, q-u-L) \right)^* \right\}, \tag{5.26}$$

$$R_{YX}(q) = R_{YX}^{(1)}(q) + R_{YX}^{(2)}(q), \tag{5.27}$$

$$R_{YX}^{(1)}(q) = L |G_1(q)|^2 H_2(q, 0), \tag{5.28}$$

$$R_{YX}^{(2)}(q) = \begin{cases} LG(q_1 + L)G^*(q_1)H_2(q, L) & 0 \le q_1 < Q - L \\ LG(q_1 - L)G^*(q_1)H_2(q, -L) & L \le q_1 < Q - 1 \\ 0 & \text{otherwise} \\ & (q_1 = q \bmod Q) \end{cases}, \tag{5.29}$$

where $G_1(q) = G\left(\mathrm{mod}(q, Q)\right)$ and $H_2^{(s)}(u, q-u) = H_2(u + sQ, q - u - sQ)$.

When the channel is time-invariant, the terms (5.26) and (5.29) are always null. Thus, the equalizer simply becomes

$$\{\mathbf{H}_{\mathrm{EQ}}\}_{ii} = \frac{|G_1(i)|^2 H_2^*(i)}{|G_1(i)|^2 |H_2(i, 0)|^2 + \sigma^2}. \tag{5.30}$$

It is immediate to see that equation (5.30) is equal to (5.21).

5.5.2 Band Equalizer

The simple 1-tap equalizer, described in Sec. 5.5.1, consists in a diagonal $\mathbf{H}_{\mathrm{EQ}}$ matrix. An idea to improve the performance is to increase the number of non-zero diagonals in the equalization matrix. In other words, the matrix has the

main diagonal and N_D upper (and lower) diagonals different from zeros. All the other diagonals are null. In matrix theory, this sparse matrix is known as banded matrix. The band equalizer is not a new idea and it is already used in OFDM [52].

To deduce the band equalizer, we assume channel matrix $\hat{\mathbf{H}}_{\text{CH}}$ has only non-zero elements in N_D diagonals on either side. If the channel matrix is not banded, we force to zero the elements outside the band, i.e., $\left\{\hat{\mathbf{H}}_{\text{CH,band}}\right\}_{ij} = \left\{\hat{\mathbf{H}}_{\text{CH}}\right\}_{ij}$ for $i \in \{0, \ldots, M-1\}, j \in \{i - N_D, \ldots, i + N_D\}$ and zero otherwise. The equalizer is given by

$$\mathbf{H}_{\text{EQ,band}} = \mathbf{R}_{XY}\mathbf{R}_{YY}^{-1}, \tag{5.31}$$

$$\mathbf{R}_{XY} = \mathbf{R}_{XX}\hat{\mathbf{H}}_{\text{CH,band}}^{H}, \tag{5.32}$$

$$\mathbf{R}_{YY} = \hat{\mathbf{H}}_{\text{CH,band}}\mathbf{R}_{XX}\hat{\mathbf{H}}_{\text{CH,band}}^{H} + \sigma^2\mathbf{I}, \tag{5.33}$$

where $\mathbf{R}_{XX} = E[XX^H]$, $\mathbf{I}$ and σ^2 is the transmitted signal autocorrelation, the identity matrix and the background noise statistical power, respectively. The matrix equalizer computation in (5.31) involves a $M \times M$ matrix inversion. Under band assumption, if $N_D \ll M$ the inversion complexity is in the order of $O(M)$ [41]. Thus, this approximation reduces the computational complexity w.r.t. a full matrix inversion, where the complexity is in the order of $O(M^3)$.

5.5.3 Block Equalizer

Another approach consists to equalize each sub-channel independently from the others. This sub-channel equalizer is represented in Fig. 5.1. In this case, the equalization matrix $\mathbf{H}_{\text{EQ}}$ has a block structure. In details, the k-th block, defined as $\mathbf{H}_{\text{EQ},k}$ ($Q \times Q$ matrix), is located in $\mathbf{H}_{\text{EQ}}$ matrix at the rows (columns) indices $i, j \in \{kQ, \ldots, (k+1)Q - 1\}$. The elements outside the blocks are null.

The proposed block equalizer mitigates the interference between the L symbols transmitted in each of the K sub-channels considering the fact that the ICI between distinct sub-channels is small due to their good frequency response confinement.

The block equalizer always removes the ISI term. In the band equalizer, ISI is removed only if N_D is greater than the number of non-zero diagonals in the channel matrix.

We start by splitting the matrix $\hat{\mathbf{H}}_{\text{CH}}$ in blocks of $Q \times Q$ elements, so that

(5.8) can be written as

$$\begin{bmatrix} \mathbf{Y}_0 \\ \mathbf{Y}_1 \\ \vdots \\ \mathbf{Y}_{K-1} \end{bmatrix} = \begin{bmatrix} \mathbf{B}_{0,0} & \mathbf{B}_{0,1} & \cdots & \mathbf{B}_{0,K-1} \\ \mathbf{B}_{1,0} & \mathbf{B}_{1,1} & \cdots & \mathbf{B}_{1,K-1} \\ \vdots & \vdots & \ddots & \vdots \\ \mathbf{B}_{K-1,0} & \mathbf{B}_{K-1,1} & \cdots & \mathbf{B}_{K-1,K-1} \end{bmatrix} \begin{bmatrix} \mathbf{X}_0 \\ \mathbf{X}_1 \\ \vdots \\ \mathbf{X}_{K-1} \end{bmatrix} + \mathbf{N}, \quad (5.34)$$

where $\mathbf{X}_k$ and $\mathbf{Y}_k$ are $Q \times 1$ vectors whose elements are the Q coefficients associated to the k-th sub-channel and $\mathbf{N}$ is the background noise vector. $\mathbf{B}_{i,j}$ is a $Q \times Q$ matrix defined as

$$\{\mathbf{B}_{i,j}\}_{r,c} = \left\{\hat{\mathbf{H}}_{\mathrm{CH}}\right\}_{r+iQ,c+jQ}, \; r, c \in \{0, \ldots, Q-1\}. \quad (5.35)$$

The k-th sub-vector in (5.34) can be written in order to separate the term of interest from the interference as follows

$$\mathbf{Y}_k = \mathbf{B}_{k,k}\mathbf{X}_k + \sum_{\substack{i=0 \\ i \neq k}}^{K-1} \mathbf{B}_{k,i}\mathbf{X}_i + \mathbf{N}_k. \quad (5.36)$$

Now, the k-th sub-channel block equalizer output vector is given by

$$\mathbf{Y}_{\mathrm{EQ},k} = \mathbf{H}_{\mathrm{EQ},k}\mathbf{Y}_k, \quad (5.37)$$

where the sub-channel equalizer matrix is computed according to the MMSE criterion. Such a matrix is obtained as

$$\mathbf{H}_{\mathrm{EQ},k} = \mathbf{R}_{X_kY_k}\mathbf{R}^{-1}_{Y_kY_k}, \quad (5.38)$$

$$\mathbf{R}_{X_kY_k} = \mathbf{R}_{X_kX_k}\mathbf{B}^H_{k,k}, \quad (5.39)$$

$$\mathbf{R}_{Y_kY_k} = \mathbf{B}_{k,k}\mathbf{R}_{X_kX_k}\mathbf{B}^H_{k,k} + \sum_{\substack{i=0 \\ i \neq k}}^{K-1} \mathbf{B}_{k,i}\mathbf{R}_{X_iX_i}\mathbf{B}^H_{k,i} + \sigma^2\mathbf{I}_Q, \quad (5.40)$$

where $\mathbf{I}_Q$ is the $Q \times Q$ identity matrix, $\mathbf{R}_{X_kY_k} = E\left[\mathbf{X}_k\mathbf{Y}^H_k\right]$ is the $Q \times Q$ correlation matrix between the vector $\mathbf{X}_k$ and the vector $\mathbf{Y}_k$, and $\mathbf{R}_{Y_kY_k} = E\left[\mathbf{Y}_k\mathbf{Y}^H_k\right]$ is the $Q \times Q$ auto-correlation matrix of the vector $\mathbf{Y}_k$. It should be noted that the signals $\mathbf{X}_i$, $i \neq k$, are treated as noise by the k-th sub-channel block equalizer since the interference that they generate is small due to the sub-channel spectral confinement.

After the sub-channel equalization, the output coefficients are weighted with the prototype pulse FD coefficients $G^*(i)$ and, finally, processed by the others stages, as shown in Figures 3.3 and 5.1.

The computation of the k-th sub-channel equalizer in (5.38) involves a $Q \times Q$ matrix inversion. Each inversion has a complexity in the order of $O(Q^3)$. The equalizer performs K matrix inversions, one for every sub-channel. Thus, the total complexity is in the order of $O(KQ^3)$.

5.5.4 Optimal Equalizer

All the previous equalizers are sub-optimal because they introduce an approximation that simplifies the channel matrix $\hat{\mathbf{H}}_{\mathrm{CH}}$ to reduce the computation complexity involved in the matrix inversion operation.

To obtain the optimal equalizer, we apply the MMSE criterion to the full matrix $\hat{\mathbf{H}}_{CH}$. The equalizer matrix is given by

$$\mathbf{H}_{\mathrm{EQ,opt}} = \mathbf{R_{XY}}{\mathbf{R_{YY}}}^{-1}, \tag{5.41}$$

$$\mathbf{R_{XY}} = \mathbf{R}_{XX}\hat{\mathbf{H}}_{\mathrm{CH}}^{H}, \tag{5.42}$$

$$\mathbf{R_{YY}} = \hat{\mathbf{H}}_{\mathrm{CH}}\mathbf{R}_{XX}\hat{\mathbf{H}}_{\mathrm{CH}}^{H} + \sigma^2\mathbf{I}, \tag{5.43}$$

If no noise is present, the optimal equalizer simply becomes $\mathbf{H}_{EQ,opt} = \hat{\mathbf{H}}_{CH}^{-1}$ (zero forcing equalizer). Thus, the system is fully orthogonal. The main disadvantage is the computation complexity. Indeed, the computing involves an inversion of a $M \times M$ matrix. The complexity is in the order of $O(M^3)$.

In Tab. 5.1 we summarize the complexity of the proposed equalizers.

Table 5.1: Complexity of the proposed equalizers.

Equalizer	Complexity
Baseline	$O(M)$
Band	$O(M)$
Block	$O(KQ^3)$
Optimal	$O(M^3)$

5.5.5 Equalizers comparison

In Fig. 5.2, a comparison between 1-tap, band and block equalizers is performed. Results show the SER in wireless time-variant scenario as a function of Doppler frequency. For CB-FMT, a frequency domain rectangular pulse is chosen, with $K = 8$, $N = 8$, $M = 240$. In OFDM, the number of sub-channel is set equal to $K = 240$. Thus, CB-FMT and OFDM have equal transmission rate. The constellation used is 4-PSK and SNR is set to 40 dB. For low Doppler frequencies, CB-FMT outperforms OFDM: CB-FMT exploits the frequency diversity introduced by the channel. For high Doppler frequencies, the

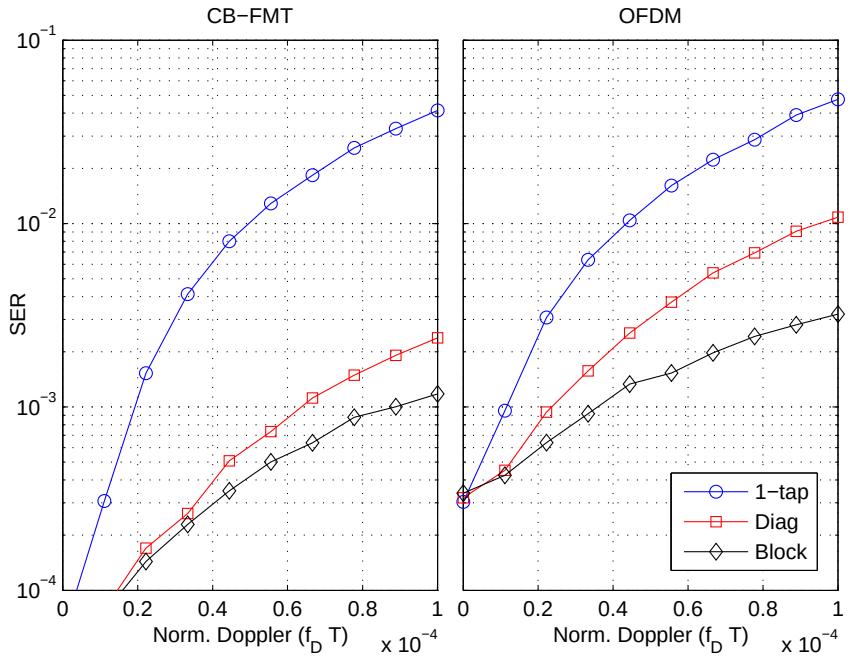

Figure 5.2: Equalizers comparison in time-variant wireless scenario.

1-tap equalizer offers equal performance for CB-FMT and OFDM. This simple equalizer has better performances for low Doppler. Band and block equalizers improve the performance of the 1-tap equalizer. For high Doppler, CB-FMT outperforms OFDM.

Chapter 6

Applications and Results

6.1 Introduction

In this chapter, we analyze the performance of the CB-FMT scheme applied to two different applications scenarios. First, we focus on PLC. The desire to deliver new communication services without requiring significant investments in the expansion of the telecommunication infrastructure has pushed the development of no-new-wire technologies. Besides wireless and twisted pair copper systems, power line communication enables the delivery of a broad range of services by the exploitation of power delivery grids. Since power lines are pervasively deployed, the use of PLC is potentially ubiquitous. In this scenario, both single-carrier and multi-carrier modulations are used. We propose the use of CB-FMT for high-data rate and low-data rate communications and we perform a comparison with the existent multi-carrier solutions, generally based on OFDM.

Another considered application scenario is the wireless. In details, we consider a transmission over frequency selective time-variant fading channels. The aim is to provide higher spectral efficiency and robustness than OFDM, especially in channels with high frequency selectivity, high time selectivity (due to mobility, Doppler effects, carrier frequency offsets and phase noise) and with asynchronous multiple users [53].

This chapter is organized as follows. In Sec. 6.2 we briefly introduce the PLC: some historical notes are provided in Sec. 6.2.1. The physical layer is described in the following three sections: channel characterization in Sec. 6.2.2, background noise in Sec. 6.2.3 and EMC aspects in Sec. 6.2.4. In Sec. 6.2.5 we disclose the results for high-data rate communications, namely the BB-PLC. This type of communications is suitable for home networking and

multimedia applications. Then, in 6.2.5, we discuss the results for low data rate communications, namely the NB-PLC. This type of communications is suitable for command and control applications or in Smart Grids.

In Sec. 6.3.3, the wireless channel is considered. In Sec. 6.3.1, we provide a summarized historical overview of the wireless communications. Then, in Sec. 6.3.2, the mobile communications scenario is introduced and the time-variant model is reported. Finally, in Sec. 6.3.3 several numerical results are provided.

6.2 Power Line Communication

6.2.1 History, Applications and Standards

PLC is not a recent idea: it was used by power utilities since about 1920, initially for communications over high voltage lines between remote stations. Since then, the application areas have significantly expanded [54]. Broad band internet access offered by PLC, over the distribution network that feeds houses and buildings, was considered of great interest especially in the first decade of the new millennium. Advanced technology was deployed and it proved to be a technically valuable solution. However, the market was already highly penetrated by DSL technology which relegated PLC in few areas, although still some hope exists about its wide use in countries under development.

In parallel, it was recognized that high speed data coming from last mile communication systems, e.g., DSL and optical fiber, might have found a bottleneck at the house door. Therefore, high speed in-home connectivity was also desirable allowing the home gateway to provide uninterrupted flow of heterogeneous traffic between the outdoor and the indoor network, the service provider and the end user. WiFi has fostered such a paradigm and it has been largely researched, developed and marketed (see the evolution of the IEEE 802.11 standard). However, wireless technology may also experience complications mostly due to unfavorable propagation conditions and limited radiated power for safety reasons that do not allow to grant full coverage at the promised speeds, e.g., in multiple floor dwellings with the presence of reinforced concrete floors. Consequently, complementary technologies were also researched, and PLC found a fertile market where to prove its own validity. Initially, a number of proprietary solutions were developed, but the key for wide deployment was standardization.

A first relevant industry standard was promoted by the HomePlug (HP) Alliance that developed a broadband solution operating in the 2-28 MHz band based on orthogonal frequency division multiplexing (OFDM). The first version HP 1.0 was capable to deliver up to 14 Mbps, the second version HPAV reached

a peak rate of 200 Mbps, and the latest version HPAV2 [55], completed in 2012, promises 2 Gbps of peak rate thanks to the extended bandwidth up to 86 MHz, multiple wire transmission (MIMO), precoding and adaptation together with a number of advanced techniques at the MAC layer. However, the first world wide broad band standard was IEEE P1901 which was ratified in 2010 [56], followed by ITU G.9960 (known as G.hn) [57].

More recently, the high momentum gained by the Smart Grid concept has reinvigorated research in PLC and in particular of so called NB-PLC technology operating in the CENELEC bands (3–148.5 kHz), in the ARIB bands (10–450 kHz) and in the FCC bands (9–490 kHz). Although the first solutions used to deploy single carrier modulation, e.g., frequency shift keying (FSK) in the IEC 61334 [58] standard, OFDM was chosen to provide higher speeds up to about 1 Mbps in the PRIME and G3 specifications [59], [60]. PRIME and G3 were the basis for the definition of the ITU G.9902 (known as G.hnem) [61]) and the IEEE P1901.2 [13] standards for the use of frequency bands below 500 kHz (ratified at the end of 2012 and 2013, respectively).

PLC can be applied to provide two-way communication in all three smart grid domains, namely transmission, distribution and user domains, exploiting high voltage (HV), medium voltage (MV) and low voltage (LV) lines [62]. It can be used to deliver several applications, for instance, remote fault detection, remote station surveillance, or state estimation. It can provide communication capabilities between sensors located in substations so that status can be monitored, and faults detected and isolated. PLC can also be exploited for the detection of islanding events. The main application in the LV part of the network is automatic/smart metering. For this application, PLC has already enjoyed a great deployment success, with about 90 million meters installed in Europe, and many more installed worldwide. Sensing, command, and control applications are also of great interest for applications inside a home or building. The in-home PLC network can be exploited for energy management purposes, together with a wide set of home automation applications for increasing security, comfort and quality of life. Two further PLC application areas lie in the management and control of micro grids, for example local generation grids using renewable energy sources such as solar cells and wind turbines, and in the connection between electrical vehicles and the grid, which can offer a wide set of applications.

There are a number of other applications of PLC among which a promising, but not yet significantly exploited, is in-vehicle (car, ship, plane, train) communications.

6.2.2 Channel Characterization

The characterization of the PLC channel is very important since it allows the development of models and the design of appropriate physical layer transmission technology. The specific characteristics depend on the application scenario and on the used transmission bandwidth. In general, the channel exhibits multipath propagation due to line discontinuities and unmatched loads which translates in severe frequency selectivity. Differently from wireless, there is no mobility so that the channel is mostly static. However, changes in the wiring topology and the connected loads induce a change in the channel response. Furthermore, cyclic time variations with periodicity equal or double the mains frequency can be present [63]. This is due to the periodic change of the loads impedance with the mains frequency, in particular of those that have rectifying units and AC/DC converters that exhibit a bi-static impedance behavior. Such cyclic time variations are mostly visible at frequencies below 2 MHz. This is because most of active loads deploy EMI filters that at high frequencies provide a (low) and stable value of impedance [64].

We distinguish three different PLC application scenarios: Indoor, outdoor low voltage (O-LV) and outdoor medium voltage (O-MV). The channels used in numerical results are described in the following.

Indoor

In-home LV grids are characterized by a layered tree structure with wires that depart from the main panel, reach derivation boxes and then the final outlets [65]. The presence of many branches gives rise to severe frequency selective fading. The results are computed exploiting a set of channel responses acquired in Italian home networks.

Outdoor LV and MV Channels

Differently from the indoor scenario, a less comprehensive analysis of the outdoor PLC channel is available in the literature for what concerns both the LV and MV part of the distribution grid. A measurement campaign of the LV outdoor channel was performed by the open PLC European research alliance (OPERA) project [66]. From the measurements, a deterministic model was proposed so that 8 reference channel responses have been tabulated.

Fig. 6.1a shows the frequency response of three different OPERA reference channels, corresponding to high (350 m), medium (250 m) and low (150 m) attenuation and decreasing path length. The average path loss profile $\overline{PL} = 10 \log_{10} E[|H|^2]$, where the average is along the measures, obtained from the full set of 8 responses is also reported. For comparison a typical in-home

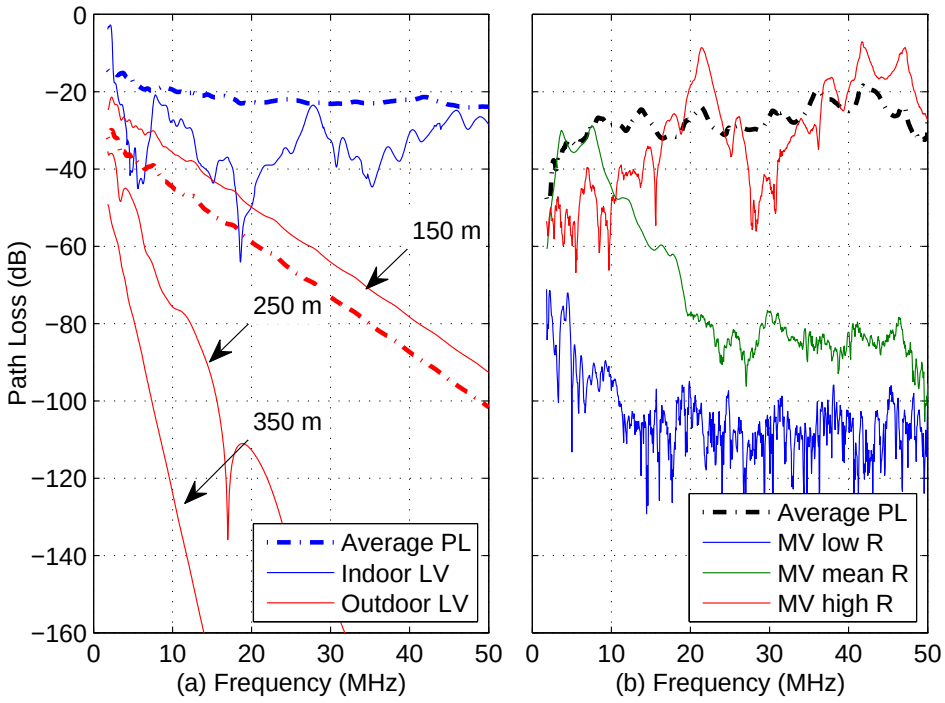

Figure 6.1: Path loss along frequencies for the outdoor (OPERA) and the indoor low voltage (a), and medium voltage (b) channels. The average path loss for each scenario is also shown.

channel response is also shown. It can be noted as the in-home channel exhibits high frequency selectivity but lower attenuation, due to a very high number of branches, discontinuities and unmatched loads, as well as the deployment of short cables. On the contrary, the outdoor LV channels introduce high attenuation but negligible fading effects which shows that what dominates is the cable attenuation rather than multipath fading.

We now consider the MV channel analyzing data obtained in a measurement campaign performed in northern Italy in 2013 and consisting of 122 responses. In Fig. 6.1b, the path loss for a good, a medium and a bad outdoor MV channel realization (ranked according to the capacity they offer), as well as the average path loss, are depicted. It should be noted that such channels are less attenuated than the LV outdoor channels. Furthermore, the average path loss profile is only slightly worse than the indoor LV case. Some further analysis of the outdoor MV channel in a grid feeding an industrial scenario, is presented in [67].

6.2.3 PLC Noise

The noise in PLC is a combination of several contributions: the background stationary noise, the impulsive noise with both periodic and aperiodic components which is introduced by noisy loads, switching devices and plug-in/plug-out procedures [54]. Often, the overall noise contribution is estimated by measuring the power spectral density (PSD) of the noise averaged over a long period of time. Typical noise PSD profiles are reported in Fig. 6.2 for the indoor and outdoor scenarios. The figure shows an exponentially decreasing profile which can be modeled for the in-home scenario as [68]

$$PSD_W^{IH}(f) = a + b|f|^c \quad [\text{dBm/Hz}], \tag{6.1}$$

while for the outdoor LV and MV scenarios as [69]

$$PSD_W^{LV,MV}(f) = a + be^{fc} \quad [\text{dBm/Hz}]. \tag{6.2}$$

Interestingly, even the best indoor case (lowest noise possible) [68] exhibits a noisier environment compared to the outdoor LV case. The average SNR at the receiver, taking into account the effect of the channel can be computed according to the equation

$$\overline{SNR} = E\left[\frac{\int_{F_1}^{F_2} P_S(f)|H(f)|^2 df}{\int_{F_1}^{F_2} P_W(f) df}\right] \quad [\text{dB}]. \tag{6.3}$$

where $E[\cdot]$ denoted the expectation, while $P_S(f)$ and $P_W(f)$ denote the transmitted signal and the noise PSD, respectively. For instance, in the MV scenario, assuming a transmission at a constant PSD level of -50 dBm/Hz the average SNR for the CENELEC 3–148.5 kHz band, the FCC 9–490 kHz (FCC) and the 1.8–30 MHz broad band , is equal to 34.86 dB, 37.34 dB, and 39.65, respectively. This shows that potentially higher SNRs are experienced with the use of BB-PLC than with NB-PLC in the smart grid context. In turn, BB PLC has the potential to offer higher noise margins and not only higher achievable rates. This has also been shown with a comparison between the use of NB OFDM and impulsive ultra wide band (UWB) modulation in [70]. However, BB-PLC may undergo more severe limitations to grant EMC and coexistence capabilities according to current norms.

6.2.4 Electromagnetic Compatibility Aspects

The transmitted PLC signal propagates according to two different modes, namely, the differential (symmetric) and the common (asymmetric) mode.

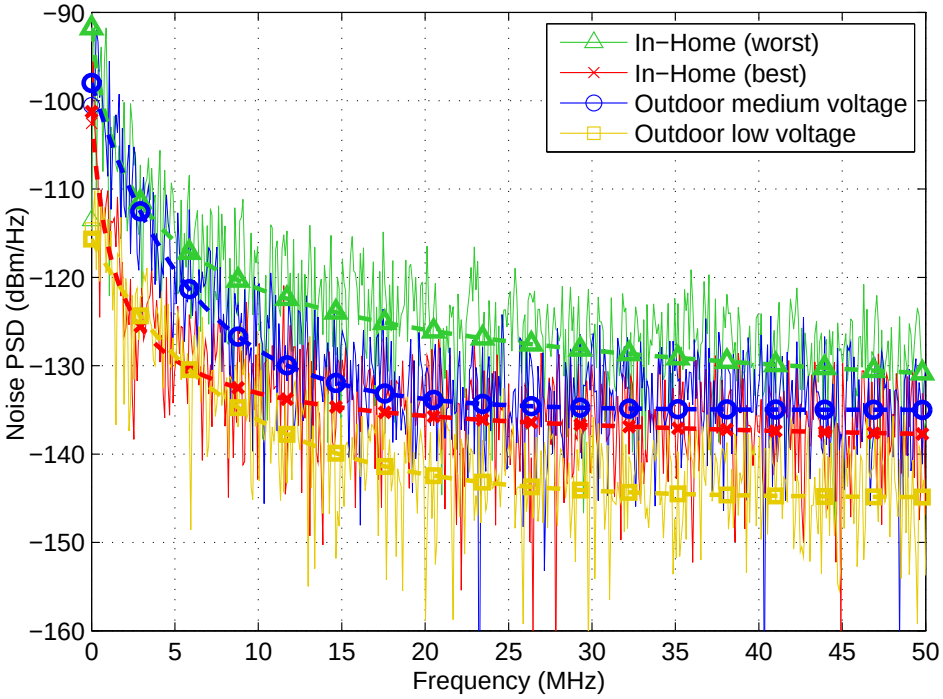

Figure 6.2: Power spectral density for indoor (worst and best case) and outdoor (low voltage and medium voltage) background noise. The noise model is also shown.

Symmetric currents flow with the same intensity, but with opposite direction, through the power line wires, namely, the phase and the neutral. Indeed, the asymmetric currents flow with the same intensity and direction on both the phase and the neutral. For the common mode (CM) currents, the conductors can be conceived as being a single wire, and the electrical circuit to be closed through a different path, e.g., the physical earth. When the propagation mode is differential, the radiated field intensity is negligible because the currents flow in opposite directions. On the contrary, weak CM currents turn into strong radiated fields. In this respect, emission limits were defined by regulation bodies. The International Electrotechnical Commission (IEC) defines different limits for the frequency ranges up to, and above 30 MHz. In the lower frequency range, the focus is on conducted emissions, and the regulations constrain the maximum amplitude of the asymmetric signal that can be injected into the power delivery network. Above 30 MHz, the limits concern the radiated emissions. The conducted and radiated emission limits are described in the CISPR

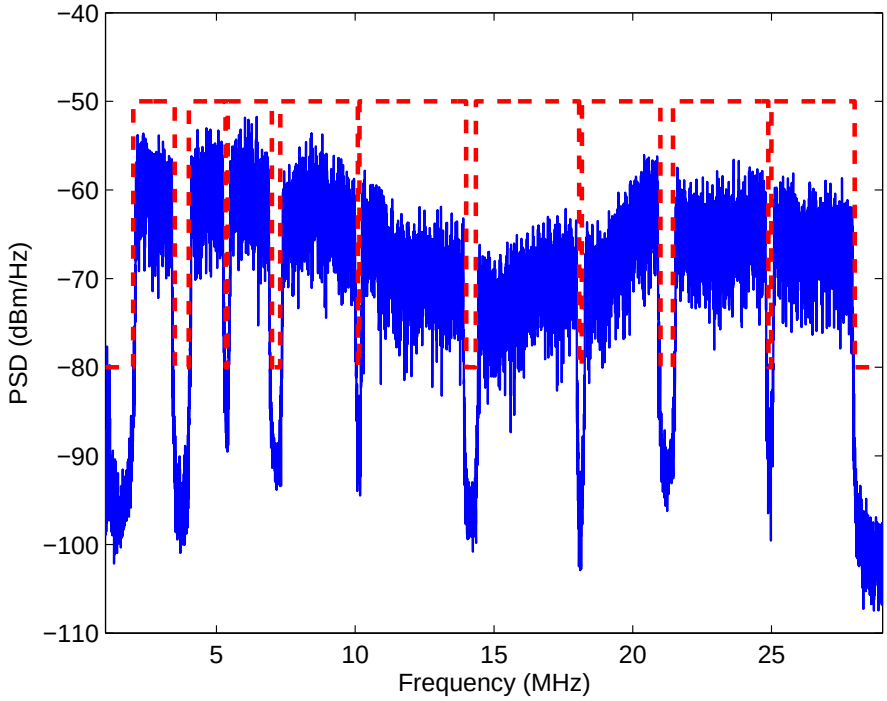

Figure 6.3: Measurement results on the transmitted PSD level. The transmitted PSD of a HomePlug compliant device. The Homeplug notching mask is also shown.

22 [71] norm. The measurement procedures are defined in the norm CISPR 16 [72].

BB-PLC

Current BB-PLC standards fulfill limitations on conducted emissions because they operate in the 2-30 MHz frequency range. CISPR 22 defines two classes of appliances, namely, class A and B, according to the application scenario. In-home appliances belong to class B. Furthermore, CISPR 22 distinguishes between the mains port and the telecommunication port. In PLC, the mains and telecommunication ports coincide. Currently, Limitations on the mains port, which coincides with the telecommunication port, define the PLC transmission levels [54]. According to CISPR 22, the average value of the CM component amplitude must be lower than $V_{lim} = 46$ dBμV and $V_{lim} = 50$ dBμV in the 0.5-5 MHz and the 5-30 MHz frequency range, respectively.

PLC employs differential mode signals. However, the asymmetries of the

PLC network lead to the partial conversion of the differential mode currents into CM components. The relation between the amplitude of the symmetric signal transmitted from a port of the PLC network and the amplitude of the asymmetric component received at any other port of the network is referred to as transverse conversion transfer loss (TCTL) [54]. The TCTL is expressed in dB and it is a positive quantity. Experimental measurement campaigns in the indoor scenario have shown that in 80% of the cases the amplitude of the common mode signal that is measured at any port of the network is at least 45 dB lower than the amplitude of the differential mode signal injected into the network, i.e., TCTL $\geq$ 45 dB. In [54], the maximum PSD of the PLC signal, that can be injected for transmission, is computed as follows

$$P_{lim} = V_{lim} + \text{TCTL} - 10\log_{10}(B_{if}) - \nu \quad \left[\frac{\text{dBm}}{\text{Hz}}\right], \tag{6.4}$$

where TCTL = 45 dB, B_{if} is the intermediate frequency bandwidth of the spectrum analyzer that is used to carry out the EMC measurements, and ν is the coefficient that allows for the conversion from dBμV to dBm, i.e., ν = 110 dBm/μV. CISPR 16-1 [73] sets B_{if} = 9 kHz. Now, if we assume a 100 Ω reference resistance, i.e., a typical value for the power line characteristic impedance, and we let V_{lim} = 50 dBμV, we obtain $P_{lim} = -54.5$ dBm/Hz. The approximated value -50 dBm/Hz is often used by broadband PLC modems.

Furthermore, the HomePlug consortium introduced the notching mask concept [74]. In Fig. 6.3, we show the HomePlug notching mask. Basically, the notching mask reduces the transmitted PSD below -80 dBm/Hz at the frequencies where radio services are supposed to transmit. Multi-carrier modulation schemes, as OFDM, satisfy the notching mask by switching off certain sub-channels. In Fig. 6.3, we also show the measured PSD of commercial modems during typical operating conditions. For a HomePlug-compliant device (BB-OFDM, Fig. 6.3) the measured PSD satisfies the notching mask, and it is below -80 dBm/Hz in correspondence of the notched bands.

NB-PLC

The frequency bands used by NB-PLC are not universal but vary as a function of the continent. In this section, we focus on Europe and North America.

In EU, the European Committee for Electrotechnical Standardization (CENELEC) has regulated NB-PLC in the frequency range 3-148.5 kHz in the standard EN 50065 [75]. This band has been partitioned in four sub-bands. CENELEC A (3-95 kHz) is reserved for electric distribution companies. Band B (95-125 kHz) can be used without restriction for any application. Band C (125-140 kHz) is used for home automation systems and the devices must

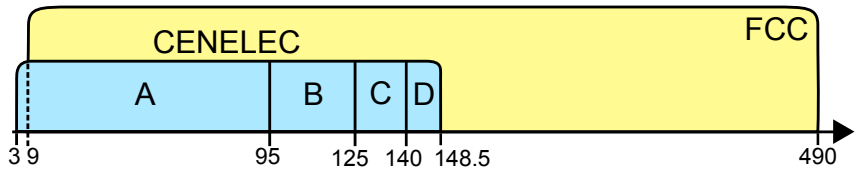

Figure 6.4: Band plan for NB-PLC in EU (CENELEC bands) and US (FCC band). Frequencies are expressed in kHz.

use a CSMA/CA protocol. Band D (140-148.5 kHz) is reserved to alarm and security systems. Concerning the transmission level, devices must fulfill the EMC regulation defined in EN 50065. The EMC measurements are performed according the CISPR 16-1 norm (quasi-peak detector with 200 Hz of resolution bandwidth). The limits are expressed in dBμV. For CENELEC A, the limit decreases with the logarithm of the frequency, from 134 dBμV at 3 kHz to 120 dBμV at 95 kHz. For B, C and D bands the limit is set to 116 dBμV.

Table 6.1: Conducted Emissions limits for NB-PLC.

Band [kHz]	dBm/Hz limit from (6.5)	
	Quasi-Peak	Average
$3-95$[1]	$1.0/-13.0$	
$95-148.5$[1]	-17.0	
$150-500$[1,2]	$-83.5/-93.5$	$-93.5/-103.5$

[1] Valid only in EU and defined in EN 50065.
[2] Valid in both EU and US and defined in CISPR 22.

In the US, the Federal Communications Commission (FCC) has regulated NB-PLC in the frequency range 9-490 kHz in [76]. The norms set both radiated and conducted limits. The radiated limit is set to 2400 μV/m at $f = 1$ kHz and decreases with the inverse of the frequency, i.e. $E_{lim} = 2400/f$, where f in the frequency expressed in kHz. The measurement is performed at a 300 m distance. Concerning conducted emissions, the limits are set for the frequencies above 150 kHz. In the 150-500 kHz frequency range, the limit decreases with the logarithm of the frequency, from 66 dBμV at 150 kHz to 56 dBμV at 500 kHz for the quasi-peak measure, and from 56 dBμV at 150 kHz to 46 dBμV at 500 kHz for the average measure. Measurement follows the CISPR 16-1 norm.

Fig. 6.4 summarizes the band plan in EU and the US.

To derive the limits in dBm/Hz, a conservative approach is followed. A common mode transmission is assumed. Consequently, the PSD limit can be

derived as follows

$$P_{lim} = V_{lim} - 10\log_{10}(B_{if}) - \nu \quad \left[\frac{\text{dBm}}{\text{Hz}}\right], \tag{6.5}$$

where V_{lim} is the limit expressed in dBμV, B_{if} is the intermediate frequency bandwidth of the spectrum analyzer that is used in EMC measurements and $\nu = 110$ is a coefficient for the conversion from dBμV to dBm. B_{if} is equal to 200 Hz for frequency below 150 kHz and is equal to 9 kHz for frequencies above 150 kHz. In Tab. 6.1, the EMC limits are reported expressed in dBm/Hz.

6.2.5 Numerical Results

BB-PLC

We evaluate the performance of the proposed CB-FMT scheme in terms of maximum achievable rate and we perform a comparison with the standard OFDM system. To provide a comparison, we evaluate the achievable rate with the Shannon capacity formula. This represent the upper bound on the rate at which information can be reliably transmitted over a communications noisy channel. The formula is known as the Shannon-Hartley theorem. Given an informative Gaussian signal with average power P_s, transmitted over a communication channel subject to additive white Gaussian noise of power P_n, the capacity, denoted as maximum achievable rate, is given by

$$C = B\log_2\left(1 + \frac{P_s}{P_n}\right), \tag{6.6}$$

where B is signal bandwidth. For a multi-carrier, the capacity is given by the sum of the capacities of the sub-channels.

For OFDM modulation, assuming a CP longer than the channel duration, the achievable rate is given by

$$C_{\text{OFDM}} = \frac{1}{(N+\mu)T}\sum_{k=0}^{N-1}\log_2\left(1 + \frac{P_a(k)}{P_\eta(k)}\right), \tag{6.7}$$

where $P_a(k)$ and $P_\eta(k)$ are the output signal power of the k-th sub-channel and the output power of noise, respectively. $P_a(k)$ takes into account both the channel attenuation and the signal transmitted power that allows us to fulfill the notching mask. For the CB-FMT system, we can view it as LK equivalent parallel signal transmissions. The achievable rate is therefore given by

$$C_{\text{CBFMT}} = \frac{1}{(M_2+\mu)T}\sum_{k=0}^{KL-1}\log_2\left(1 + \frac{P_a(k)}{P_\eta(k) + P_I(k)}\right), \tag{6.8}$$

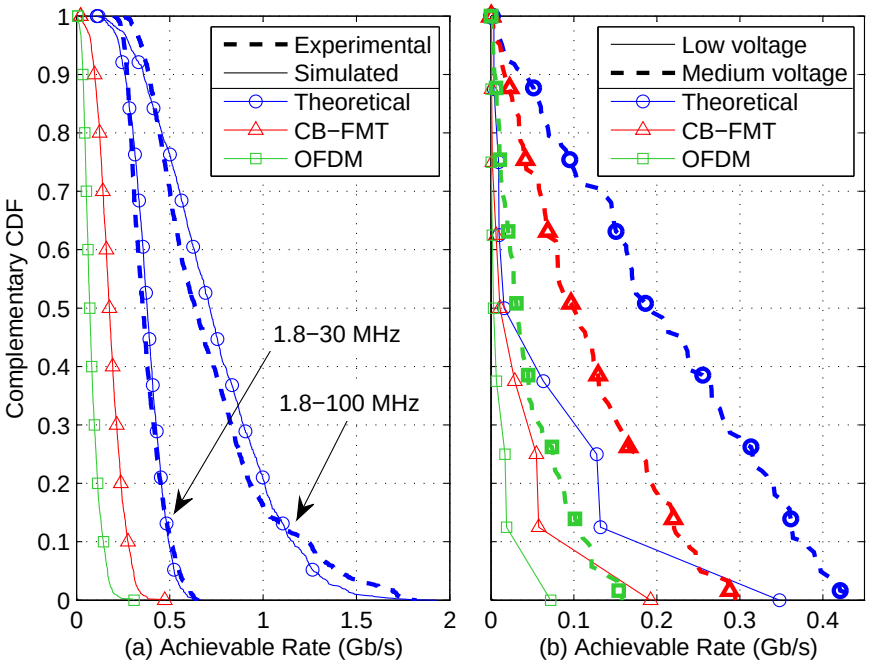

Figure 6.5: Achievable rate complementary CDF (C-CDF) for the indoor scenario in the 1.8–30 and 1.8–100 MHz frequency band (on left), and for the outdoor LV and MV scenarios in the 1.8–30 MHz (on right). The C-CDF for the CB-FMT and the OFDM schemes in the 1.8–30 MHz frequency band for the in-home (on left) and outdoor LV and MV are also depicted.

where $P_a(k)$, $P_n(k)$ and $P_I(k)$ are the output signal power of the k-th sub-channel, the output power of the noise and the output power of the interference that may be present, respectively. Interference can in fact be present among the L data symbols transmitted in one of the K sub-channels unless Zero-Forcing equalization is implemented.

We consider the indoor case and we infer the improvement provided by the frequency band extension from 1.8–30 to 1.8–100 MHz. Fig. 6.5 depicts the achievable rate CCDF for the channels described in Section 6.2.2, assuming -50 dBm/Hz PSD constraint in the 1.8–30 MHz and a flat -80 dBm/Hz PSD in the 30–100 MHz. Notching is typically required in BB-PLC to allow coexistence with radio amateur and broadcast signals. Therefore, the PSD notching mask depicted in Fig. 6.6 is herein used to derive results. The colored background noise models named in-home (best), O-LV and O-MV in Section 6.2.3 are herein adopted for each different environment, respectively.

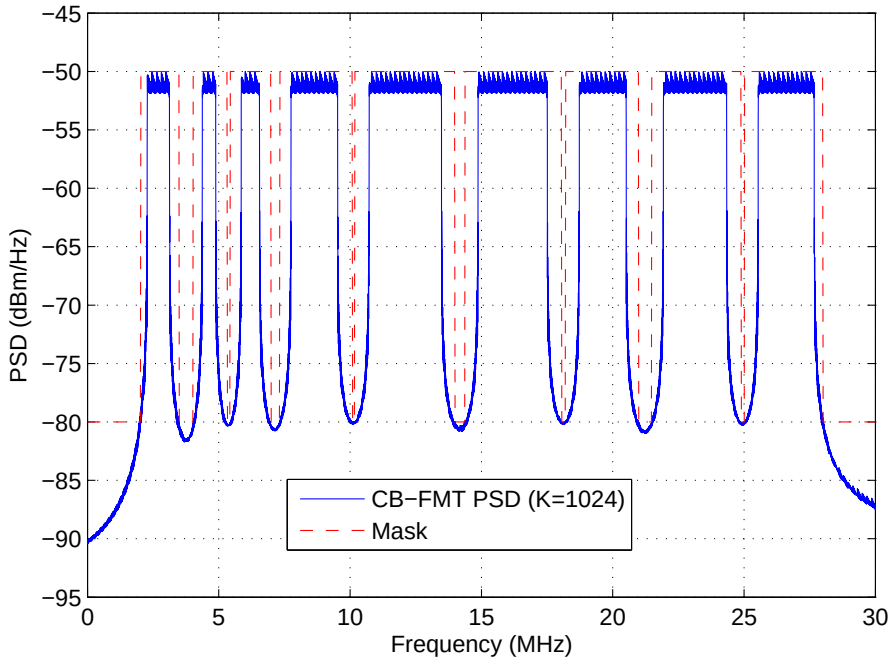

Figure 6.6: Analytic CB-FMT PSD for $K = 1024$. In dotted line, the Homeplug notching mask.

In Fig. 6.7 we report the achievable rate in Mbps as a function of number of sub-channels K used for OFDM for a specific channel realization (corresponding to the median channel ranked in terms of capacity selected from the data base of measured channels). The CP length is chosen so that the highest rate is offered under the further constraint of fulfilling the notching mask in Fig. 6.6. The noise PSD is the best according to the model in Fig. 6.2. The figure shows that the offered rate increases with the number of sub-channels since the overhead introduced by the CP is reduced and better notching capability is obtained. However, the performance gap from the channel capacity is high. Such a gap can be reduced by deploying FMT since it has the potential to offer superior performance. In this example, FMT uses long root-raised-cosine pulses with roll-off set to 0.2 and one-tap sub-channel fractionally spaced equalization. The interpolation factor is equal to $N = 4/3K$ and the filter length is equal to $20N$. Therefore, significantly better notching capability is achieved.

In Fig. 6.7 the achievable rate for CB-FMT is also shown. For CB-FMT, a rectangular frequency domain pulse is used to obtain a maximum rate transmission Giuseppe Lambrughi. The interpolation factor is equal to $N = K$ and

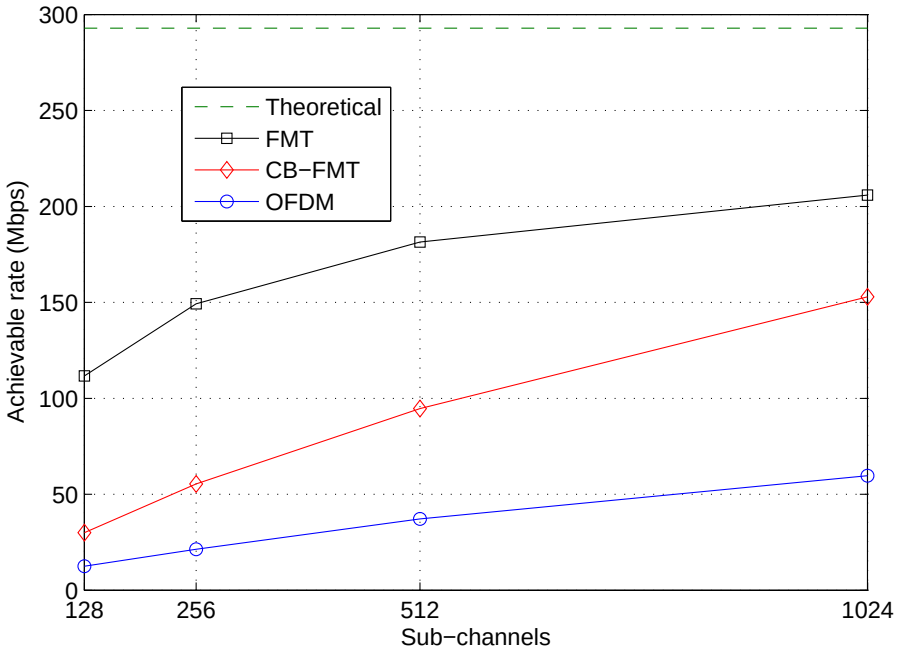

Figure 6.7: Comparison between FMT, CB-FMT and OFDM as a function of the sub-channel number K in terms of maximum achievable rate.

the filter length is equal to $4K$. For both CB-FMT and OFDM a cyclic prefix is added to the transmitted signal to reduce the interference between different blocks. The cyclic prefix duration is optimized to maximize the achievable rate. The figure shows, that CB-FMT provides better performance than OFDM. For $K = 1024$, CB-FMT is not far away from FMT but it has significant less complexity, i.e. CB-FMT complexity is about 36% of the FMT complexity. The ability of providing good notching selectivity is shown in Fig. 6.6 where the PSD of the transmitted CB-FMT signal is compared to the target notching mask. Finally, in Fig. 6.5 we compare the CCDF of the achievable rate obtained with OFDM and with CB-FMT assuming transmission in the 1.8–30 MHz band. The figure shows that CB-FMT outperforms OFDM offering about 52% and 20% of the theoretical channel capacity, respectively.

NB-PLC

We perform a performance comparison when CB-FMT is deployed in the G3-PLC and P1901.2 standards instead of PS-OFDM in terms of maximum achievable rate. The PL channel and the noise are modeled as described in Sections

6.2.2 and 6.2.3, respectively. For PS-OFDM, we adopted the parameters described in the G3-PLC and IEEE P1901.2 standards and reported in the following paragraph.

G3-PLC and IEEE P1901.2 parameters In this paragraph we provide an overview on the G3-PLC and IEEE P1901.2 parameters.

G3-PLC G3-PLC was initially released for operating in the CENELEC A band. Later, Maxim - member of the G3 Alliance - has proposed to extend G3-PLC to the other CENELEC bands [77] and to the FCC band [78]. In base band, the sampling frequency is set to $1/T = 200$ kHz for CENELEC bands and to $1/T = 600$ kHz for the FCC band. The sub-carrier number is set to $M = 128$ and the cyclic prefix length is set to 30 samples. In Table 6.2(a), we report the active sub-carries for each band. G3-PLC can operate in multiple CENELEC bands to increase the rate. In detail, it can operate in these bands: A, B, C, D, BC, BCD and BD.

To fulfill the EMC regulation, a PSD mask is specified. The transmitted signal spectrum must not exceed the limit of 120 dBμV. To ensure the coexistence with the single-carrier solution IEC 61334, a notch has been introduced between 63.3 kHz and 73.8 kHz. In the spectral notch, the limit is set to 70 dBμV. Finally, the PSD dynamic range in the notch and outside the notch has to be larger than 25 dB.

P1901.2 The new IEEE P1901.2 standard joins the previous NB-PLC standards to obtain a universal communication specification. At the physical layer, PS-OFDM is used. In CENELEC bands, IEEE P1901.2 can operate only in bands A and B. The full FCC band is partitioned in two parts, below 150 kHz (FCC-low band) and above 150 kHz (FCC-above-CENELEC band). The band above 150 kHz has be partitioned in 2 or 4 sub-bands. In this work, we consider the FCC-above-CENELEC partition reported in Tab. 6.2(b). In the following, we denote the FCC-low band as LOW.

The PSD mask specifies a limit of 120 dBμV. If a notch is present, the limit is set to 100 dBμV. The minimum PSD dynamic range in the notch and outside the notch has to be larger than 20 dB.

Performance Comparison For CB-FMT, we set the same sampling frequency and maximum sub-channel number as for PS-OFDM. The CB-FMT prototype pulse length is equal to $M = KQ = LN$, where Q is an integer number. In the following results, we set $K = N$ and $Q = L = 8$. The CB-FMT prototype pulse has a rectangular shape in frequency domain, i.e. $G(i) = 1$

Table 6.2: Active Carriers for G3-PLC and IEEE P1901.2 standards.

(a) Active carriers in CENELEC and FCC bands.

Band	Start freq.	Stop freq.	Cardinality
CENELEC A[1,2]	35.9	90.6	36
CENELEC B[1,2]	98.4	121.8	16
CENELEC C[1]	128.1	137.5	7
CENELEC D[1]	142.1	146.8	4
G3-FCC[1]	145.3	478.1	72
FCC-above-CENELEC[2]	154.6	487.5	72
FCC-low (LOW)[2]	37.5	117.2	18

[1] Used in the G3-PLC standard
[2] Used in the IEEE P1901.2 standard

(b) Partition of the FCC-above-CENELEC band.

	Start freq.	Stop freq.	Cardinality
HIGH_0	154.7	487.5	72
HIGH_1	154.7	318.8	36
HIGH_2	323.4	487.5	36

for $i \in \{0, \ldots, Q-1\}$ and 0 otherwise; $G(i)$ denotes the M-point DFT of the prototype pulse.

With such a choice, it should be noted that CB-FMT becomes the dual of OFDM where the rectangular pulse shape is chosen in the time-domain. Concerning the transmission power, we set the PSD of the transmitted signals so that we fulfill the EMC regulations and the PSD mask as shown in Fig. 6.9. In detail, we set a PSD limit to -45 dBm/Hz for frequencies below 150 kHz and -105 dBm/Hz for frequencies above 150 kHz. The limits are set equal for both systems. We have computed the achievable rate for all the eight OPERA channels for different CENELEC and FCC bands. The achievable rate is computed according to the Shannon capacity formula. In detail, for each band, we have computed the CCDF. Two CCDF examples are shown in Fig. 6.8. Then, we compute the mean achievable rate among the eight OPERA channels. The achievable rate is evaluated for two different CB-FMT configurations. Firstly, we set the CB-FMT active sub-channels to be equal to those used in OFDM. We denote this configuration as *CB-FMT reduced*. Then, we increase the number of active sub-channels so that the available bandwidth is better occupied. We denote this configuration as *CB-FMT full*. This is made possible because CB-FMT has a significant lower out-of-band PSD which allows to better fulfill the norms and to increase the possible number of active sub-channels. An

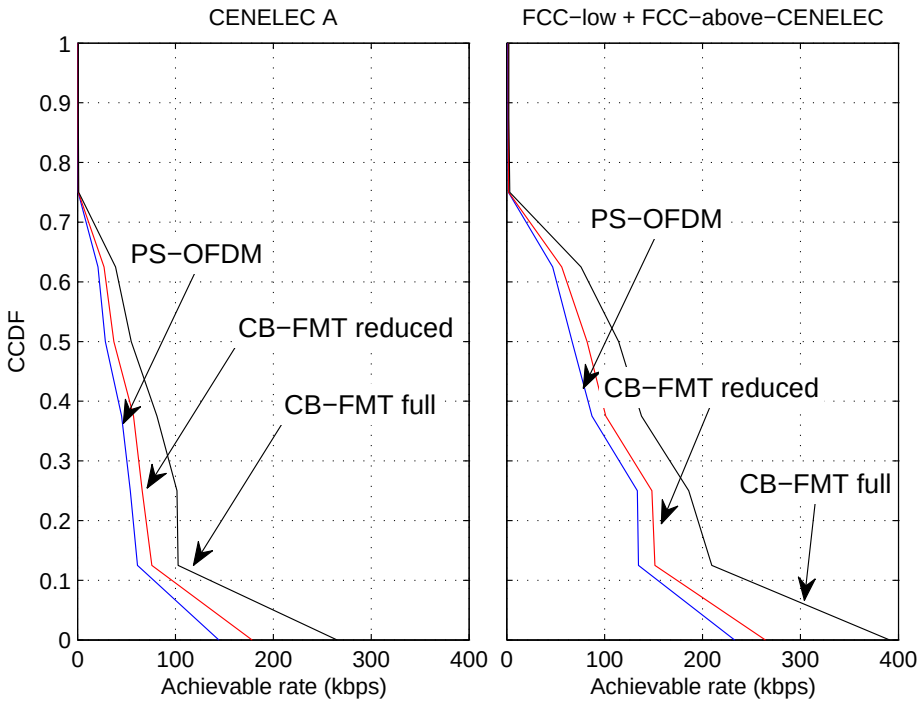

Figure 6.8: CCDF of the achievable rate for the OPERA channels.

example of these two configurations is reported in Fig. 6.9. In the previous figure, CB-FMT and OFDM have equal PSD peak. In Fig. 6.10, we increase the PSD peak of CB-FMT s.t. the two systems have equal PSD limit in the notches. Fig. 6.11 shows the achievable rate with the increased PSD limit.

The achievable rate values are reported in Tab. 6.3. CB-FMT outperforms OFDM because it is capable of exploiting the sub-channel energy with matched filtering in the frequency domain. For the FCC band, we note that when the transmission involves only the high part of the band (above 150 kHz), the achievable rate is significantly low. This is due to the low PSD level (-105 dBm/Hz) that has to be used to satisfy the EMC regulation.

To evaluate the spectrum confinement properties of PS-OFDM and CB-FMT, we compute the power ratio between the useful signal in a sub-band and the interference generated by the signals in the adjacent sub-bands. In

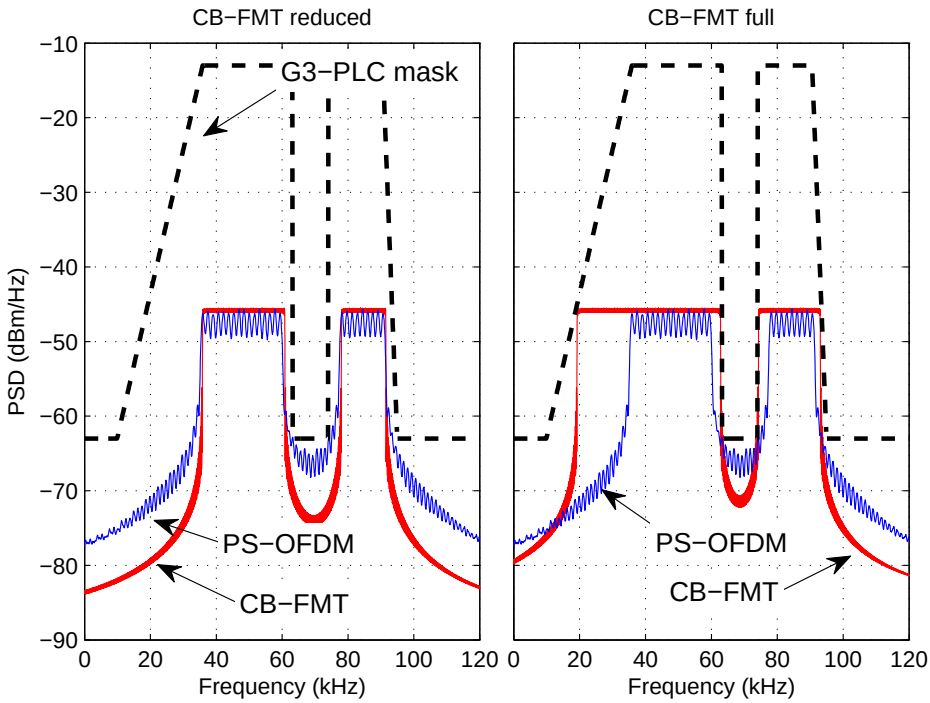

Figure 6.9: PSD example for PS-OFDM, CB-FMT reduced and full with equal PSD peak.

detail, we focus on the CENELEC band. We compute such ratio as

$$R_{ab} = \frac{P_a}{P_b}, \quad a \in \{A, B, C, D\}, b \in \{Z - a\}, \quad Z = \{A, B, C, D, \text{FSK}_{notch}\}, \tag{6.9}$$

where P_a is the power of the transmitted signal in the CENELEC a band and P_b is the interference power generated by the signal transmitted in the b band. FSK_{notch} denotes the range of frequencies that need to be notched to have coexistence with single-carrier S-FSK. In Tab. 6.4, we report these power ratios. It can be observed that CB-FMT generates less interference in adjacent bands than PS-OFDM. For CB-FMT, the power ratios are about 9 dB higher than the OFDM ratios showing again that we can have better coexistence with systems operating in distinct bands.

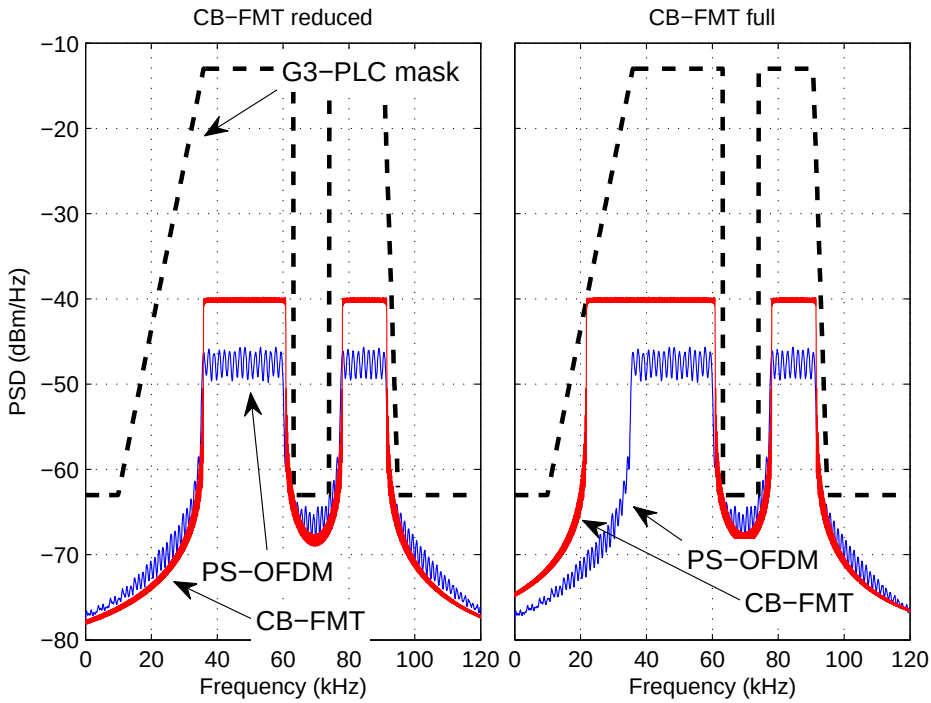

Figure 6.10: PSD example for PS-OFDM, CB-FMT reduced and full with PSD limit in the notches.

6.3 Wireless Communication

6.3.1 Historical notes

Wireless communications are a very large topic. Similarly to PLC, they are not a recent idea. Early electrical communications were wired and they started with the electrical telegraph, in the first half of XIX century. In the second half of the XIX century, in 1867, Maxwell predicts the existence of electromagnetic waves [79]. This discovery was the origin of the wireless. In 1897, Marconi sent the first ever intercontinental wireless communication over open sea, opening the doors to the long distance wireless communications.

The first cellular systems were introduced in the early 1980s [48]. The first generation (1G) cellulars were based on analog FM modulation. They were unencrypted and easy to tap via a radio scanner and susceptible to the cloning problem. The second generation (2G) was introduced in early 1990s [48] and exploits the digital modulations. Commercially, 2G cellular system

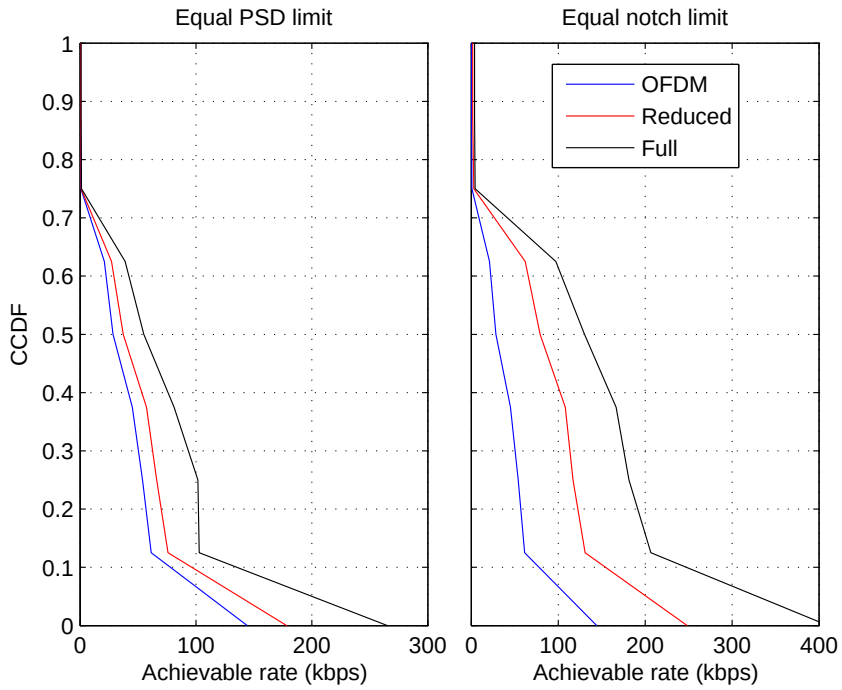

Figure 6.11: CCDF of the achievable rate with different PSD limit.

was launched in Europe with the GSM standard. In contrast to the 1G, the 2G cellular communications are encrypted. Furthermore, the spectral characteristic is improved and data services for mobile was introduced.

The capillary diffusion of the cellular has grown the demand for data from the mobile phone, i.e. internet access. Thus, the third generation (3G) of cellular system was introduced in early 2000s [80]. The data rate was pushed up from few hundred of kbps to a decade of Mbps. This high data rate extends the application scenarios from simple telephony to mobile internet access, video calls and mobile TV.

The demand of high data rate mobile communications is still growing. The fourth generation (4G) of mobile telecommunications have been recently released with the LTE standard [8]. The application scenario includes broadband internet access, IP telephony, HD mobile TV.

Simultaneously to cellular systems birth, the WLAN has been introduced. WLAN was initially introduced as an alternative to cabled LAN for communications in places where the wiring was not possible. First WLAN devices were expensive and the technology did not penetrate the market. In late 1990s,

Table 6.3: Mean achievable rate for several bands in EU and US.

		Mean achievable rate [kbps]		
Band		PS-OFDM	CB-FMT reduced	CB-FMT full
CENELEC	A	44.38	55.45	80.88
	B	53.96	67.52	76.48
	C	25.48	31.77	42.39
	D	13.81	17.20	22.83
	BC	95.57	119.45	128.95
	BCD	122.80	153.35	157.34
	BD	67.77	79.03	99.30
FCC	G3-FCC	2.28	3.25	3.63
	$HIGH_0$	2.53	3.63	3.63
	$HIGH_1$	0.23	0.31	0.31
	$HIGH_2$	2.28	3.22	3.25
	$LOW+HIGH_0$	88.37	101.27	140.34
	$LOW+HIGH_1$	86.07	97.96	137.02
	$LOW+HIGH_2$	88.12	100.87	139.97

Table 6.4: Power ratios between useful signal and interference in CENELEC bands for PS-OFDM and CB-FMT.

	Power Ratio (PS-OFDM/CB-FMT reduced) [dB]				
Band	A	B	C	D	FSK notch
A	-	25.5/34.2	35.0/42.8	38.3/46.1	24.0/31.7
B	21.7/30.5	-	23.1/32.1	31.8/40.4	33.1/41.3
C	27.2/35.5	19.2/28.8	-	20.6/29.4	36.3/44.5
D	28.6/36.1	26.3/34.8	18.0/26.6	-	37.8/45.4

low-cost chipsets give the opportunity for WLAN to emerge [81]. The first large scale scenario was the home internet access sharing. Introduction of the standard IEEE 802.11, namely commercial as Wi-Fi, has capillary diffuse the WLAN. The Wi-Fi market has grown to become the second largest wireless communications market, behind the cellular telephony [81].

6.3.2 Channel Characterization

Wireless channel characteristics depends on the application scenario. Four scenarios could be distinguished:

1. **Mobile satellite**. This system provides global coverage.

2. **Land mobile radio systems** These systems use the cellular network.

The coverage is not global and depend on the cells network extension.

3. **Wireless metropolitan area networks**. These systems provide radio connectivity over a small area. The covering is limited to few city blocks or several blocks of building, e.g. in a campus.

4. **Wireless local area networks**. These systems provide radio connectivity for stationary in-building users.

In this work, the land mobile radio systems are considered. In this scenario, two components can be mentioned. First, the fixed base stations (BSs) define the cells and the coverage extension. In a macrocellular scenario, communications between different BSs are a line-of-sight radio propagation. Indeed, the antennas are elevated w.r.t. the terrain and the local scatters have a low impact. The second system component is the mobile station (MS). Typically, there are several natural and man-made object between BS and MS. The propagation is non-line-of-sight and the radio waves propagate via reflections, diffraction and scattering. The propagation follow different paths between BS and MS. Each path introduce an attenuation and a delay, different path by path. This propagation is known as multipath propagation. This propagation can introduce constructive and destructive addition and the behavioral is strongly linked to MS location. If the MS is not fixed but it is moving, the scattering environment changes, introducing a phenomenon known as envelope fading.

The channel coefficients $\alpha_\ell(n)$ in channel impulse response in (2.3) are considered modeled according to the Clarke's isotropic scattering model [48]. Therefore, they are assumed to be independent stationary zero-mean complex Gaussian processes with correlation defined as

$$E\left[\alpha_\ell^*(m)\alpha_{\ell'}(m+n)\right] = \Omega_\ell J_0(2\pi f_D n)\delta(\ell-\ell'), \tag{6.10}$$

where f_D and $J_0(\cdot)$ are the maximum Doppler frequency and the zero-order Bessel function of the first kind, respectively. We assume an exponential power decay profile, i.e., $\Omega_\ell = \Omega_0\ e^{-\ell/\gamma}$, where Ω_0 is a normalization constant to obtain unit average power, and γ is the normalized, w.r.t. the sampling period, delay spread. The Doppler frequency is a parameters function of the velocity v and the incidence angle between the EM wave and the MS antenna. In this work, the maximum Doppler frequency in considered, defined as

$$f_D = \frac{v}{\lambda_c}, \tag{6.11}$$

where v is the MS velocity and λ_c is the wavelength of the electromagnetic signal, typically the carrier frequency.

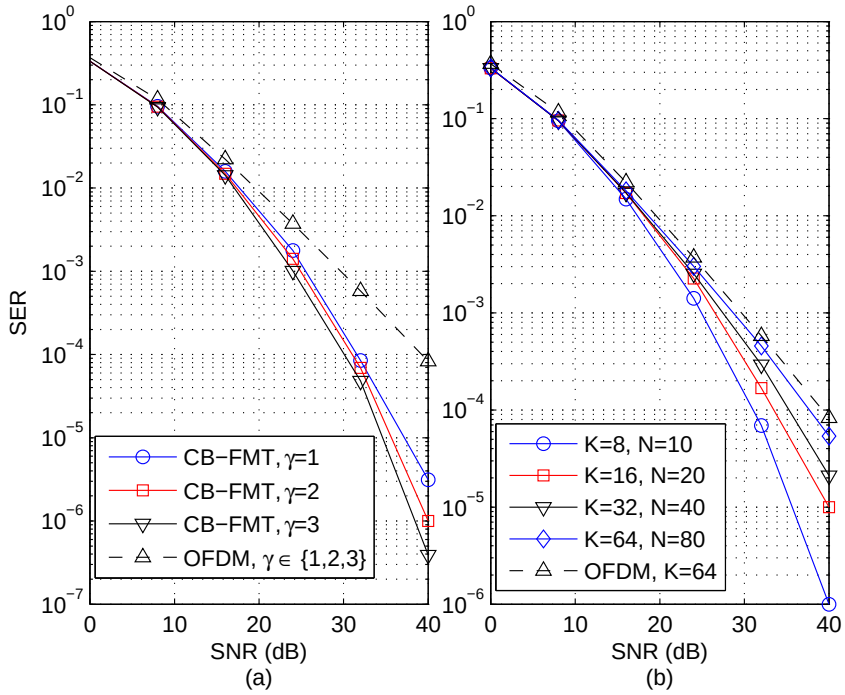

Figure 6.12: In (a), SER vs. SNR varying the normalized delay spread γ for CB-FMT and OFDM. In (b), SER vs. SNR for various combinations of CB-FMT parameters when $\gamma = 2$. The systems have identical transmission bandwidth and data rate. The 1-tap equalizer for time-invariant channels is used (Sec. 5.4).

6.3.3 Numerical Results

In order to evaluate the performance of CB-FMT, we consider the transmission over a wireless fading channel. The channel impulse response is modeled as in (6.10) and it is truncated at -10 dB.

First, we show the performance in terms of average SER versus SNR varying the delay spread γ, considering CB-FMT and OFDM both using a CP and a one tap MMSE equalizer at the receiver. 4-PSK modulation is assumed. Then, we show the maximum achievable data rate as a function of Doppler spread for different SNR values.

In Fig. 6.12.a, the CB-FMT system has parameters $K = 8$, $N = 10$, $M = 320$, and CP with length 8 samples. For the OFDM system, we consider the number of sub-channels equal to $K = 64$, as in the IEEE 802.11 WLAN standard. In OFDM the CP length is set equal to 18 samples so that the two

systems have identical transmission rate assuming an identical transmission bandwidth. We consider channels with normalized delay spread equal to $\gamma = \{1, 2, 3\}$ and no Doppler spread (static channels). The results reveal that CB-FMT can significantly lower the SER, especially for high values of delay spread γ. A 10 dB SNR gain is found at $SER = 10^{-4}$. This is due to the fact that CB-FMT in conjunction with the MMSE equalizer can exploit the frequency diversity introduced by the channel, and thus, the more dispersive the channel, the higher the gain is for CB-FMT. In OFDM the performance is identical for all values of γ considered, since the sub-channels see flat Rayleigh fading [34].

In Fig. 6.12.b, we show the SER for several combinations of parameters in CB-FMT. In all cases, CB-FMT has $M = 320$, $K \in \{8, 16, 32, 64\}$, $N \in \{10, 20, 40, 80\}$ and a CP equal to 8 samples so that it has the same data rate of OFDM. The normalized delay spread is set to $\gamma = 2$. The SER grows with the number of sub-channels K and it approaches that of OFDM, i.e., the performance of 4-PSK in flat Rayleigh fading. This is because when K increases, $Q = M/K$ decreases and, consequential, the ability of coherently capturing the sub-channel energy (thus exploiting diversity) with the MMSE equalizer is reduced.

In Fig. 6.13, we show the average maximum achievable rate (Shannon capacity [37]) assuming time-variant frequency selective fading and additive white Gaussian noise. The system parameters for OFDM and CB-FMT are equal to those assumed for the SER analysis in Fig. 6.12.a. Furthermore, we assume the transmission bandwidth $W = 1/T = 20$ MHz and the normalized delay spread $\gamma = 2$. For the OFDM system, we use a 1-tap MMSE sub-channel equalizer. For CB-FMT, we apply two different equalizers. Firstly, we use a 1-tap MMSE equalizer, similar to the OFDM equalizer. Then, we use the sub-channel block equalizer described in Section 5.5. For low SNRs (equal to 15 dB in the considered case), the 1 tap equalizer in CB-FMT is sufficient and provides good performance which is better than that offered by OFDM also in the presence of high Doppler spreads. For high SNRs (25 dB in the considered case), CB-FMT with single tap equalization provides higher achievable rate than OFDM for a Doppler below 400 Hz. For higher Doppler the performance is dominated by the interference. Therefore, the MMSE sub-channel block equalizer provides significantly higher performance than the single tap equalizer. In particular, at the maximum Doppler considered that is equal to 4 kHz, the gain in achievable rate of CB-FMT over OFDM is 6%, 20% for an SNR equal to 15 dB and 25 dB, respectively. This shows that CB-FMT has the potential of improving the performance of OFDM also in the presence of channel time variations introduced by mobility of the nodes. The gains in Fig. 6.13 are due to the fact that CB-FMT is more robust to the channel time variations due

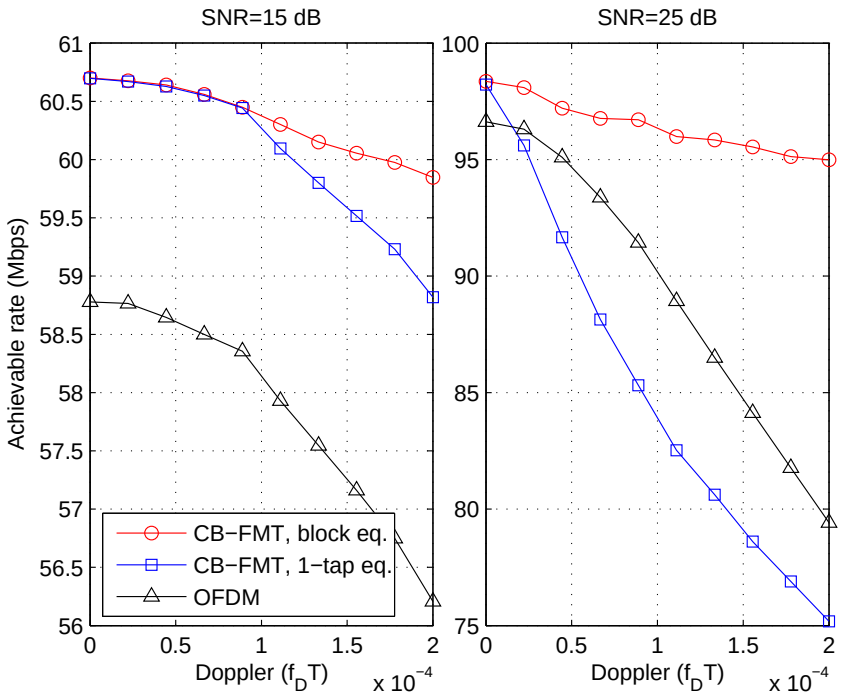

Figure 6.13: Maximum achievable rate for OFDM and CB-FMT in frequency selective time-variant fading with normalized delay spread $\gamma = 2$. Transmission bandwidth 20 MHz. The 1-tap equalizer for time-variant channels is used (Sec. 5.5.1)

to the use of frequency confined pulses that allow to lower the ICI compared to OFDM. Furthermore, as shown also in the BER curves, CB-FMT with the FD equalizer can exploit the sub-channel frequency diversity.

Chapter 7

Conclusions

In this thesis, a FBM referred to as Cyclic Block Filtered Multitone (CB-FMT) modulation has been presented. This scheme can be derived from the FMT architecture philosophy. However, linear convolutions are substituted with circular convolutions and data are processed in blocks, which justifies the acronym CB-FMT. The efficient implementation of CB-FMT in the frequency domain has been discussed and the performance analysis has been carried out.

In Chapter 2, a general FBM architecture has been introduced. This general scheme is valid for both OFDM and FMT. A mathematical model of the general scheme is also provided. Then, the main concepts of OFDM and FMT have been briefly recalled to simplify the understanding of the CB-FMT scheme.

In Chapter 3, the CB-FMT scheme has been described in detail. This scheme can be derived from the FMT architecture philosophy. However, linear convolutions are substituted with circular convolutions and data are processed in blocks, which justifies the acronym CB-FMT. The efficient implementation of CB-FMT in the frequency domain has been discussed and the performance analysis has been carried out. The computational complexity analysis has shown that CB-FMT can significantly lower the complexity compared to conventional FMT with even longer pulses. Then, the orthogonal CB-FMT design can be done in the frequency domain and a simple pulse design procedure can be followed by sampling in the FD a band limited Nyquist pulse. Finally, the orthogonal CB-FMT transmitted signal shows high frequency compactness and potentially lower PAPR than OFDM if a lower number of data sub-channels is used (still offering the same or higher spectral efficiency).

In Chapter 4 the orthogonality problem, introduced in the previous chapter, has been extensively analyzed. A mathematical analysis has been performed to determine the orthogonality criterion in time domain and in frequency domain.

Then, the conditions to have orthogonal pulses have been derived with a non-linear trigonometric function combination. The analysis has shown that there exists an infinite set of orthogonal solutions. From this set, two optimal pulses have been identified. These pulses maximize two cost functions, i.e. the in-band-to-out-band energy ratio and the maximum achievable rate in a time-variant scenario. Numerical results have shown that the optimal pulses can improve the performance w.r.t. the simple root-raised-cosine pulse.

In Chapter 5, the equalization problem has been analyzed. Equalizers are necessary to restore the orthogonality when the transmission medium is frequency selective and/or time-variant. A matrix channel model has been introduced. This model has shown that PR is possible when the cyclic prefix is greater than the channel impulse response length and there is no noise. When the CP is short w.r.t. the channel impulse response length, an additive interference term is present. We have shown that in time-invariant scenario a single 1-tap equalizer is sufficient to restore the orthogonality. In a time-variant scenario, more complicated equalizers are proposed. We have proposed four equalizers with growing complexity.

Finally, in Chapter 6, numerical results have been provided. The CB-FMT scheme has been applied to Power Line Communication and Wireless scenarios. For BB-PLC, numerical results have shown that CB-FMT can provide higher achievable rate than OFDM in typical PLC channels fulfilling severe power spectrum mask constraints. For NB-PLC, we have briefly described the band plan and EMC norms for NB-PLC in EU and US. Then, we have focused on two NB-PLC standards, namely G3-PLC and the recent IEEE P1901.2 standard. A numerical analysis has been performed in the O-LV scenario. Numerical results have shown that CB-FMT has higher achievable rate w.r.t. OFDM which is due to the ability of better exploiting the channel energy and providing better spectrum confinement which allows to fulfill the PSD norms with a higher number of active sub-channels than PS-OFDM. The better spectrum notching capability allows also to generate lower interference to adjacent bands, e.g., CENELEC bands, which in turn allows to have better coexistence between PLC systems operating in different bands.

For the wireless scenario, sub-channel FD MMSE equalization provides good performance in doubly-selective fading channels. In particular, lower symbol error rate and higher spectral efficiency than OFDM in multipath time-variant fading channels has been found depending on the choice of parameters.

In conclusion, this thesis has shown that CB-FMT is a new filter bank modulation scheme with great potential and practical relevance in both wireless and PLC applications.

7.1 Future perspectives

- **Coding**. Performances have been evaluated in terms of achievable rate (Shannon capacity). This is the theoretical upper limit to the transmission rate. In practical, the rate is much lower than the theoretical limit in an uncoded transmission. Future work can cover a performances analysis in terms of symbol error rate with coding techniques.

- **PAPR**. CB-FMT can reduce the PAPR w.r.t. OFDM. The main reason is related to the reduction in the number of sub-carriers. In CB-FMT, prototype pulse design adds several degrees of freedom. Future work can cover a PAPR analysis as a function of the prototype pulse. Furthermore, the PAPR reduction techniques developed in OFDM can be applied to CB-FMT too.

- **Channel estimation**. In this thesis, the channel impulse is assumed to be known. In practical, the transmission medium is unknown and it requires to be estimated. In the literature, several estimation algorithms have been proposed. Future work can cover the channel estimation problem in CB-FMT with a performances analysis.

- **Comparison with others scheme**. Recently, in the literature, some FBM schemes that involve cyclic convolution have been proposed. Future work can cover a comparison between CB-FMT and these schemes to highlight the main differences in the architecture and in the performances.

Bibliography

[1] M. Doelz, E. Heald, and D. Martin, "Binary Data Transmission Techniques for Linear Systems," *Proceedings of the IRE*, pp. 656–661, 1957.

[2] J. Bingham, "Multicarrier Modulation for Data Transmission, an Idea whose Time Has Come," *IEEE Commun. Mag.*, vol. 31, pp. 5 – 14, May 1990.

[3] G. Cherubini, E. Eleftheriou, and S. Olcer, "Filtered Multitone Modulation for Very High-Speed Digital Subscribe Lines," *IEEE J. Sel. Areas Commun.*, pp. 1016–1028, June 2002.

[4] A. M. Tonello, "Asynchronous Multicarrier Multiple Access: Optimal and Sub-optimal Detection and Decoding," *Bell Labs Technical Journal*, vol. 7, no. 3, pp. 191–217, 2003.

[5] A. M. Tonello, "A Concatenated Multitone Multiple-Antenna Air-Interface for the Asynchronous Multiple-Access Channel," *IEEE Journal on Selected Areas in Communications*, vol. 24, pp. 457–469, March 2006.

[6] IEEE, "802.11 Standard: Wireless LAN Medium Access Control and Physical Layer Specification," 2007.

[7] IEEE, "802.16: IEEE Standard for Air Interface for Broadband Wireless Access Systems," 2012.

[8] D. Astely, E. Dahlman, A. Furuskar, Y. Jading, M. Lindstrom, and S. Parkvall, "LTE: The Evolution of Mobile Broadband," *IEEE Communications Magazine*, vol. 47, pp. 44–51, April 2009.

[9] ETSI, "Radio Broadcasting Systems; Digital Audio Broadcasting (DAB) to mobile, portable and fxed receivers," 2006.

[10] ETSI, "Digital Video Broadcasting (DVB); A Guideline for the Use of DVB Specifcations and Standards," 2008.

[11] "Asymmetric digital subscriber line (ADSL) transceivers." Recommendation G.992.1, 1999.

[12] "Home Plug Alliance." [Online]. Available: `http://www.homeplug.org`.

[13] "IEEE Standard for Low-Frequency (less than 500 kHz) Narrowband Power Line Communications for Smart Grid Applications." IEEE 1901.2-2013, Dec. 2013.

[14] F. Sjoberg, R. Nilsson, M. Isaksson, P. Odling, and P. Borjesson, "Asynchronous Zipper," in *IEEE International Conference on Communications, 1999. (ICC '99)*, vol. 1, pp. 231–235 vol.1, 1999.

[15] R. Van Nee and A. de Wild, "Reducing the Peak-to-average Power Ratio of OFDM," in *Proc. of IEEE Vehicular Technology Conference (VTC 98)*, vol. 3, pp. 2072–2076, 1998.

[16] S. Sandberg and M. Tzannes, "Overlapped discrete multitone modulation for high speed copper wire communications," *IEEE Journal on Selected Areas in Communications*, vol. 13, pp. 1571–1585, Dec 1995.

[17] P. Siohan, C. Siclet, and N. Lacaille, "Analysis and design of OFDM/OQAM systems based on filterbank theory," *Signal Processing, IEEE Transactions on*, vol. 50, pp. 1170–1183, May 2002.

[18] S. Weinstein, "The History of Orthogonal Frequency-Division Multiplexing [History of Communications]," *IEEE Communications Magazine*, vol. 47, pp. 26–35, November 2009.

[19] R. R. Mosier and R. G. Clabaugh, "Kineplex, a Bandwidth-Efficient Binary Transmission System," *American Institute of Electrical Engineers, Part I: Communication and Electronics, Transactions of the*, vol. 76, pp. 723–728, Jan 1958.

[20] R. W. Chang, "Synthesis of Band-Limited Orthogonal Signals for Multichannel Data Transmission," *Bell System Technical Journal*, vol. 45, no. 10, pp. 1775–1796, 1966.

[21] S. Weinstein and P. Ebert, "Data Transmission by Frequency-Division Multiplexing Using the Discrete Fourier Transform," *Communication Technology, IEEE Transactions on*, vol. 19, pp. 628–634, October 1971.

[22] A. Peled and A. Ruiz, "Frequency Domain Data Transmission Using Reduced Computational Complexity Algorithms," in *Acoustics, Speech, and Signal Processing, IEEE International Conference on ICASSP '80.*, vol. 5, pp. 964–967, Apr 1980.

[23] A. Tonello and F. Pecile, "Efficient Architectures for Multiuser FMT Systems and Application to Power Line Communications," *IEEE Transactions on Communications*, vol. 57, pp. 1275–1279, May 2009.

[24] F. Pecile and A. Tonello, "On the Design of Filter Bank Systems in Power Line Channels Based on Achievable Rate," in *IEEE International Symposium on Power Line Communications and Its Applications, 2009 (ISPLC 2009).*, pp. 228–232, March 2009.

[25] W. Kozek and A. Molisch, "Nonorthogonal Pulseshapes for Multicarrier Communications in Doubly Dispersive Channels," *IEEE J. Sel. Areas Commun.*, vol. 16, pp. 1579–1589, October 1998.

[26] M. Harteneck, S. Weiss, and R. Stewart, "Design of Near Perfect Reconstruction Oversampled Filter Banks for Subband Adaptive Filters," *IEEE Transactions on Circuits and Systems II: Analog and Digital Signal Processing*, vol. 46, no. 8, pp. 1081–1085, 1999.

[27] B. Borna and T. Davidson, "Efficient Design of FMT Systems," *IEEE Trans. Commun.*, vol. 54, pp. 794–797, May 2006.

[28] C. Siclet, P. Siohan, and D. Pinchon, "Perfect Reconstruction Conditions and Design of Oversampled DFT-Modulated Transmultiplexer," *EURASIP Journ. on Appl. Sign. Proc.*, pp. 1–14, 2006.

[29] N. Moret and A. M. Tonello, "Design of Orthogonal Filtered Multitone Modulation Systems and Comparison among Efficient Realizations," *EURASIP Journal on Advanced Signal Processing*, 2010.

[30] M. Clark, "Adaptive Frequency-domain Equalization and Diversity Combining for Broadband Wireless Communications," *IEEE Journal on Selected Areas in Communications*, vol. 16, no. 8, pp. 1385–1395, 1998.

[31] A. Tonello, "Method and apparatus for filtered multitone modulation using circular convolution," 2008. Patent n. UD2008A000099, PCT WO2009135886A1.

[32] G. Fettweis, M. Krondorf, and S. Bittner, "GFDM - Generalized Frequency Division Multiplexing," in *IEEE 69th Vehicular Technology Conference, 2009. VTC Spring 2009.*, pp. 1–4, April 2009.

[33] A. Tonello, "Time Domain and Frequency Domain Implementations of FMT Modulation Architectures," in *IEEE International Conference on Acoustics, Speech and Signal Processing (ICASSP 2006)*, vol. 4, pp. IV–IV, May 2006.

[34] A. M. Tonello, "Performance Limits for Filtered Multitone Modulation in Fading Channels," *IEEE Trans. Wireless Commun.*, vol. 4, pp. 2121–2135, September 2005.

[35] P. Vaidyanathan, *Multirate Systems And Filter Banks*. Electrical engineering. Electronic and digital design, Dorling Kindersley, 1993.

[36] IEEE, *802.11 Standard: Wireless LAN Medium Access Control and Physical Layer Specification*. 2007.

[37] J. Proakis and M. Salehi, *Digital Communications*. McGraw-Hill higher education, McGraw-Hill Education, 2007.

[38] H. Ochiai and H. Imai, "On the Distribution of the Peak-to-average Power Ratio in OFDM signals," *IEEE Transactions on Communications*, vol. 49, no. 2, pp. 282–289, 2001.

[39] S. H. Han and J. H. Lee, "An Overview of Peak-to-Average Power Ratio Reduction Techniques for Multicarrier Transmission," *IEEE Wireless Communications*, vol. 12, pp. 56–65, April 2005.

[40] T. van Waterschoot, V. Le Nir, J. Duplicy, and M. Moonen, "Analytical Expressions for the Power Spectral Density of CP-OFDM and ZP-OFDM Signals," *IEEE Signal Processing Letters*, vol. 17, no. 4, pp. 371–374, 2010.

[41] G. Golub and C. Van Loan, *Matrix Computations*. Johns Hopkins Studies in the Mathematical Sciences, Johns Hopkins University Press, 1996.

[42] P. Davis, *Circulant Matrices*. Chelsea Publishing Series, Chelsea, 1994.

[43] D. M. Y. Sommerville, *An Introduction to the Geometry of N Dimensions*. Methuen Publishin Ltd, 1929.

[44] R. H. Byrd, J. C. Gilbert, and J. Nocedal, "A Trust Region Method Based on Interior Point Techniques for Nonlinear Programming," *Mathematical Programming*, vol. 89, no. 1, pp. 149–185, 2000.

[45] R. H. Byrd, M. E. Hribar, and J. Nocedal, "An Interior Point Algorithm for Large-Scale Nonlinear Programming," *SIAM J. on Optimization*, vol. 9, pp. 877–900, Apr. 1999.

[46] R. Waltz, J. Morales, J. Nocedal, and D. Orban, "An Interior Algorithm for Nonlinear Optimization that Combines Line Search and Trust Region Steps," *Mathematical Programming*, vol. 107, no. 3, pp. 391–408, 2006.

[47] A. M. Tonello, "A Novel Multi-carrier Scheme: Cyclic Block Filtered Multitone Modulation," in *Proc. of IEEE International Conference on Communications (ICC 2013)*, (Budapest, Hungary), pp. 3856–3860, June 2013.

[48] G. L. Stuber, *Principles of Mobile Communication*. Kluwer Academic Publishers, second ed., 1996.

[49] L. L. Scharf, *Statistical Signal Processing*. Addison-Wesley, 1991.

[50] H. Sari, G. Karam, and I. Jeanclaude, "Transmission Techniques for Digital Terrestrial TV Broadcasting," *IEEE Communications Magazine*, vol. 33, pp. 100–109, Feb 1995.

[51] P. Schniter, "Low-Complexity Equalization of OFDM in Doubly Selective Channels," *IEEE Transactions on Signal Processing*, vol. 52, pp. 1002–1011, April 2004.

[52] L. Rugini, P. Banelli, and G. Leus, "Low-Complexity Banded Equalizers for OFDM Systems in Doppler Spread Channels," *EURASIP Journal on Advances in Signal Processing*, vol. 2006, no. 1, p. 067404, 2006.

[53] A. M. Tonello and F. Pecile, "Analytical Results about the Robustness of FMT Modulation with Several Prototype Pulses in Time-Frequency Selective Fading Channels," *IEEE Transactions on Wireless Communication*, vol. 7, pp. 1634–1645, May 2008.

[54] H. C. Ferreira, L. Lampe, J. Newbury, and T. G. Swart, *Power Line Communications: Theory and Applications for Narrowband and Broadband Communications over Power Lines*. NY: Wiley & Sons, 2010.

[55] L. Yonge, K. Afkhamie, L. Guerrieri, S. Katar, H. Lioe, P. Pagani, R. Riva, D. M. Schneider, and A. Schwager, "An Overview of the HomePlug AV2 Technology," *Journal of Electrical and Computer Engineering*, vol. 2013, pp. 1–20, 2013.

[56] "IEEE Standard for Broadband over Power Line Networks: Medium Access Control and Physical Layer Specifications." IEEE 1901-2010, Sept. 2010.

[57] "Unified High-Speed Wireline-Based Home Networking Transceivers - System Architecture and Physical Layer Specification." Recommendation ITU-T G.9960, Dec. 2011. [Online]. Available: `http://www.itu.int/rec/T-REC-G.9960-201112-I`.

[58] IEC, *Distribution automation using distribution line carrier systems - Part 5-1: Lower layer profiles - The spread frequency shift keying (S-FSK) profile (IEC 61334-5-1, ed. 2.0)*, May 2001.

[59] "Narrowband Orthogonal Frequency Division Multiplexing Power Line Communication Transceivers for PRIME Networks." Recommendation ITU-T G.9904, 2012.

[60] "Narrowband Orthogonal Frequency Division Multiplexing Power Line Communication Transceivers for G3-PLC Networks." Recommendation ITU-T G.9903, 2012.

[61] "Narrowband Orthogonal Frequency Division Multiplexing Power Line Communication Transceivers for ITU-T G.hnem networks." Recommendation ITU-T G.9902: Narrowband, Oct. 2012. [Online]. Available: `http://www.itu.int/rec/T-REC-G.9902-201210-I`.

[62] S. Goel, S. F. Bush, and D. Bakken, eds., *IEEE Vision for Smart Grid Communications: 2030 and Beyond*. IEEE Standard Association, 2013.

[63] F. Corripio, J. Arrabal, L. del Rio, and J. Munoz, "Analysis of the cyclic short-term variation of indoor power line channels," *Selected Areas in Communications, IEEE Journal on*, vol. 24, no. 7, pp. 1327–1338, 2006.

[64] M. Antoniali and A. M. Tonello, "Measurement and characterization of load impedances in home power line grids," *IEEE Trans. on Instrumentation and Measurements (in press)*, 2013.

[65] A. M. Tonello and F. Versolatto, "Bottom-Up Statistical PLC Channel Modeling - Part I: Random Topology Model and Efficient Transfer Function Computation," *IEEE Trans. Power Del.*, vol. 26, pp. 891–898, April 2011.

[66] M. Babic *et al.*, "D4: "Theoretical Postulation of the PLC Channel Model OPERA"," tech. rep., IST Integrated Project No. 507667 funded by EC, March 2005. OPERA Deliverable D4.

[67] A. M. Tonello, F. Versolatto, and C. Tornelli, "Analysis of Impulsive UWB Modulation on a Real MV Test Network," in *Proc. of IEEE International Symposium on Power Line Communications and Its Applications (ISPLC)*, pp. 18–23, 3–6 April 2011.

[68] T. Esmailian, F. R. Kschischang, and P. Glenn Gulak, "In-Building Power Lines as High-Speed Communication Channels: Channel Characterization and a Test Channel Ensemble," *Intern. J. of Commun. Syst.*, vol. 16, pp. 381–400, June 2003.

[69] M. Babic *et al.*, "D5 Pathloss as a function of frequency, distance and network topology for various LV and MV European powerline networks.," tech. rep., IST Integrated Project No. 507667, April 2005. OPERA Deliverable D5.

[70] A. Tonello, F. Versolatto, and M. Girotto, "Multitechnology (I-UWB and OFDM) Coexistent Communications on the Power Delivery Network," *IEEE Transactions on Power Delivery*, vol. 28, no. 4, pp. 2039–2047, 2013.

[71] IEC, *Information Technology Equipment - Radio Disturbance Characteristics - Limits and Methods of Measurement (CISPR 22, ed. 6.0)*, Sept. 2008.

[72] IEC, *Specification for Radio Disturbance and Immunity Measuring Apparatus and Methods (CISPR 16-SER, ed. 1.0)*.

[73] IEC, *Part 1: Radio Disturbance and Immunity Measuring Apparatus (CISPR 16-1, ed. 2.1)*, Oct. 2002.

[74] N. Weling, "Expedient Permanent PSD Reduction Table as Mitigation Method to Protect Radio Services," in *15th IEEE International Symposium on Power Line Communications and Its Applications (ISPLC 2011)*, pp. 305–310, apr 2011.

[75] "Signalling on Low-Voltage Electrical Installations in the Frequency Range 3 kHz to 148,5 kHz - Part 1: General Requirements, Frequency Bands and Electromagnetic Disturbances." EN 50065-1:2011, 2011.

[76] "Code of Federal Regulations, Title 47, Part 15 (47 CFR 15)." Title 47 of the Code of Federal Regulations.

[77] Maxim, "Supplement to PLC G3 physical layer specification for operation in CENELEC B/C/BC/D/BCD/BD frequency bands."

[Online]. Available: http://www.maximintegrated.com/en/products/powerline/pdfs/G3-PLC-CENELEC-Supplement-B.pdf.

[78] Maxim, " Supplement to PLC G3 physical layer specifications for operation in the FCC frequency band." [Online]. Available: http://www.maximintegrated.com/en/products/powerline/pdfs/G3-PLC-FCC-Supplement-B.pdf.

[79] P. Harman, *The Natural Philosophy of James Clerk Maxwell*. Cambridge University Press, 2001.

[80] C. Smith and D. Collins, *3G Wireless Networks*. McGraw-Hill telecom professional, Mcgraw-hill, 2001.

[81] C. L. Jackson, K. J. Negus, and A. Petrick, "History of wireless local area networks (wlans) in the unlicensed bands," *info*, vol. 11, no. 5, pp. 36–56, 2009.